



ulm university universität
uulm



**Deutsches Zentrum
für Luft- und Raumfahrt**

MODELING OF SILICON-AIR BATTERIES

Master Thesis

By

Yasin Emre Durmus

Energy Science and Technology - Ulm University

Deutsches Zentrum für Luft- und Raumfahrt

Supervised By:

Dr. Birger Horstmann

Examiners:

Prof. Dr. Arnulf Latz

Prof. Dr. Werner Tillmetz

December 2013

DECLARATION

I hereby declare that this thesis was performed and written on my own and that references and sources used within this work have been explicitly indicated.

I am aware that making false declaration may have serious consequences.

Ulm, 02/12/2013

Yasin Emre Durmus

ABSTRACT

In order to improve the lifetime and performance of an **electric drive train system**, one of the most challenging tasks is to improve the performance of the **electrochemical energy storage** device in terms of the power and energy density. The energy density of current electrochemical concepts, such as Li-ion batteries, is still far from meeting all demands due to technological and thermodynamical limitations. Therefore, new electrochemical energy storage concepts with enhanced energy density, such as metal-air batteries, are currently being investigated.

Silicon-air batteries, a recent concept of metal-air batteries, have been researched over the past few years. From a thermodynamic point of view, the silicon-oxygen couple is very promising and attractive. The theoretical energy density of silicon-air batteries ($8,470 \text{ Wh kg}^{-1}$) are close to lithium-air batteries ($11,140 \text{ Wh kg}^{-1}$) which is the highest capacity among all the batteries.

The aim of this work is to **model** primary silicon-air batteries by **computationally** to evaluate the performance of the battery and improve the understanding of the system. In that respect, we developed a **mathematical model** of the battery on the basis of the mechanisms discussed in previous experimental studies. Our mathematical model is based on the electrochemical processes including reactions, transport mechanisms, oxygen dissolution, volume conditions, and nucleation and growth processes. Finally, we investigate remarkable effect of water addition into the electrolyte with our simulations. We discuss our results in terms of nucleation and growth in the battery, half-cell potentials of the electrodes, spatial distribution of crystallization in the electrode pores, discharge of the battery at various water contents, and discharge of the battery at various discharge currents.

TABLE OF CONTENTS

Chapter 1 : INTRODUCTION	1
Chapter 2 : METAL-AIR BATTERIES	4
2.1 Zinc-Air Battery.....	11
2.2 Lithium-Air Battery	15
Chapter 3 : SILICON-AIR BATTERIES	22
3.1 Literature Review	22
Chapter 4 : MODELING	38
4.1 Simulation Methodology.....	39
4.2 Numerical Details	41
4.3 Electrochemical Reactions	42
4.4 Transport Mechanisms.....	45
4.5 Oxygen Dissolution.....	47
4.6 Phase Coexistence in the Electrodes (Volume Conditions)	48
4.7 Nucleation and Growth	49
Chapter 5 : PARAMETERIZATION	53
5.1 Structure of the battery	53
5.2 Thermodynamics.....	54
5.3 Transport and Kinetics.....	55
Chapter 6 : RESULTS AND DISCUSSION	60
6.1 Nucleation and Growth.....	60
6.2 Half-cell Potentials	65
6.3 Spatial Distribution of Crystallization.....	71

6.4 Discharge at Various Water Contents	79
6.5 Discharge at Various Discharge Currents	86
Chapter 7 : CONCLUSION AND OUTLOOK.....	91
ACKNOWLEDGEMENT	93
LIST OF FIGURES	94
LIST OF TABLES	98
LIST OF SYMBOLS.....	99
LIST OF CONSTANTS	100
BIBLIOGRAPHY.....	101

Chapter 1 : INTRODUCTION

Electric mobility received enormous interest in the past decade. In this thesis, we refer to electric mobility as wheeled vehicles powered by electrical energy. In the 21st century, electric vehicles (EVs) will probably become an important part of the world drive vehicles. The history of electric vehicles began in the mid-19th century.¹ Before the development of internal combustion engines (ICEs), EVs were developed shortly after the invention of lead-acid batteries. Over 30,000 electric cars were on the roads in United States between 1900-1912.¹ People were using either horse-drawn vehicles or gasoline powered vehicles with a hand-crank system at that time. The pollution issues of using horse-drawn vehicles in the cities and the dangers of hand-cranking internal combustion engines were the two major drawbacks of these systems. However, an electric vehicle did not have these drawbacks, and thus, it became popular when it was successfully invented. Nevertheless, internal combustion engines dominated the industry in the next years. They combined the advantage of longer range and lower cost over electric vehicles and the hand-crank issue was solved with the electric starter motor. For these reasons, gasoline-powered vehicles still dominate the automotive industry today.

Why did it take so long to use electric cars again as people do nowadays? The reasons why electric cars have not been used as means of transport were: development advance of ICEs, long driving range of ICEs, cheap oil, and good gas infrastructure. The idea of using electrical vehicles has been renewed in the recent decade. Limited amount of fossil fuels on earth and environmental effects of using internal combustion engine vehicles are the two main reasons which are acting as a driving force to shift to electric drive systems. Also, the rising demand on oil increases fuel prices. Therefore, people try to find an alternative way to operate their vehicles. The best option so far, seems to use batteries or fuel cells on vehicles. Hybrid vehicles, which use two or more different power sources (ICEs-Battery, Battery-Fuel cell) to power the vehicle, are other options. As a result, not only the dependence of fossil fuels would vanish, but air pollution would be significantly reduced.

Motor vehicles are a significant source of urban air pollution and are increasingly important contributors of carbon dioxide emissions and other greenhouse gases. Hundreds of million people in urban areas worldwide are exposed to traffic-generated air pollution. Therefore, traffic-generated air pollution received great attention in the recent years. Moreover, there are low emission zones operated by some cities or towns where the most polluting vehicles are regulated to increase air quality. If a vehicle with an internal combustion engine has a carbon emission rate (regulations may differ for each country) which exceeds the limits, it is forbidden to enter the low emission zone. In contrast, an EV, a hybrid vehicle or a fuel cell vehicle does not confront with this problem due to having zero or low carbon emission rates.

In the meantime, there are many ongoing projects using batteries on vehicles which make batteries more favorable. One example is Smart Grid projects. Electric vehicles do not only reduce carbon emissions, but they can be integrated perfectly into a so called smart grid network. In this network, electric vehicles are not just the consumers. They can be used as suppliers during the peak load times; in other words, they can be used as energy storage for the grid.

In summary, electric mobility, as an alternative to internal combustion engines, provides a significant reduction in emissions of pollutants and greenhouse gas emissions, a significant reduction in noise and operating costs, as well as the overall benefits to the environment, especially in urban areas. Electricity onboard a car can be provided either by a battery or a fuel cell. The focus of this thesis will be on batteries. Besides EVs, batteries are used in almost every portable electronic device. Therefore, an achievement in battery technology does not only affect the automotive industry, but it affects other electronic devices as well.

As a result of increased demand of batteries in the automotive industry, new battery technologies have become the center of interest for many studies. Even though other technologies (i.e. Li-ion with 160 Wh kg^{-1}) have witnessed many achievements in the past decades, it is still inadequate to achieve a considerable amount of energy density (approximately $1,700 \text{ Wh kg}^{-1}$, basing on practical energy density of gasoline) and meet all the demands. For this reason, new electrochemical concepts with increased energy density have

received a lot of attention in the past years. Metal-air batteries are being considered as a promising candidate in this manner. Even though metal-air batteries have some obstacles (i.e. rechargeability, electrolyte stability, discharge product issues) like other types of prototype batteries, the energy density they possess is very high.

The purpose of the study presented in this thesis is to understand the primary silicon-air battery concept and model it mathematically with the computer. Mathematical modeling includes developing sets of equations for the electrochemical processes including reactions, transport mechanisms, oxygen dissolution, volume conditions, and nucleation and growth processes. The model is based on experimental results for primary silicon-air batteries. It can be used to predict the discharge performance of silicon-air battery under several conditions, such as addition of water into the electrolyte and various constant current densities. The model is implemented in DENIS² and validated by comparing it with suitable experiments.

The scope of this thesis is as follows: Chapter 2 provides general ideas about metal-air batteries. Particularly, zinc-air and lithium-air batteries are discussed in detail. Chapter 3 describes the available experimental results on primary silicon-air batteries. It is important to discuss these experiments since our model includes the mechanisms and parameters from these studies. Computational battery modeling forms the core of this thesis and is described in Chapter 4. The adopted modeling approach is explained in detail and the model equations for a silicon-air battery model are derived in this chapter. Chapter 5 provides the parameters that are used in the battery model. The simulation of the developed model is implemented, the results are discussed and the comparisons between the literature and the simulation results are done in Chapter 6. Conclusions are drawn in Chapter 7 and recommendations are made for further research in experiments and for improvements of the model.

Chapter 2 : METAL-AIR BATTERIES

With regards to the replacement of fossil fuel driven systems by electrochemical energy storage devices (i.e. batteries, fuel cells), a considerable amount of energy and power density needs to be achieved by these energy storage devices. There have been many successful achievements by now. At first, primary batteries were used for portable electronic devices. Some of the advances for different types of primary batteries are shown in Figure 2-1. Even though the energy densities are considerably high, capacities of the batteries do not allow using these batteries for long operation times. Therefore, people started to think about producing a battery which is rechargeable, so that the battery can be recharged rather than replaced, unlike the primary batteries.

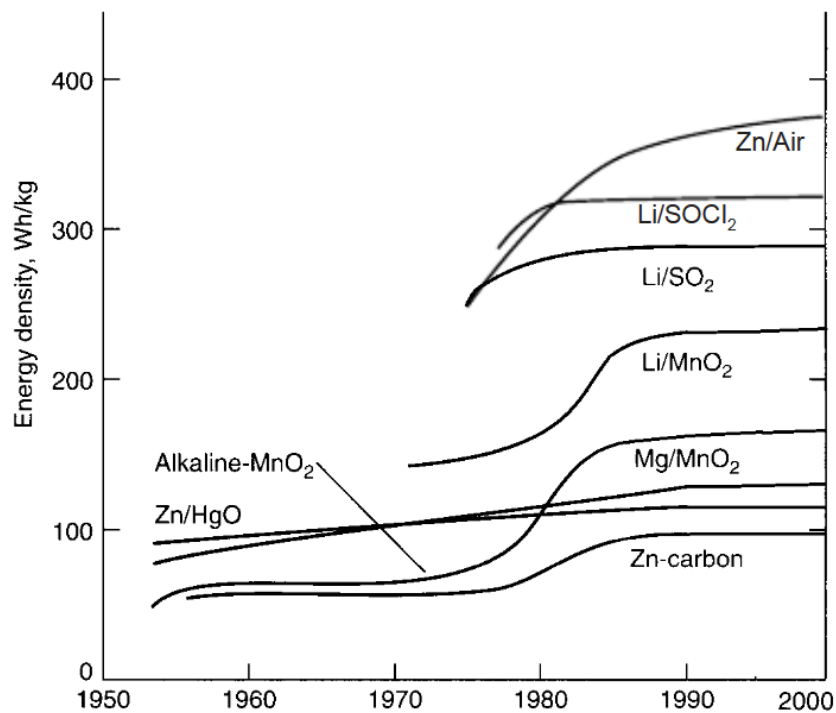


Figure 2-1 Advances in development of primary batteries in 20th century. Continuous discharge at 20°C; 40-60 h rate; AA or similar size battery¹

Development of some important battery chemistries are shown in Figure 2-2. The first rechargeable or secondary battery was a lead-acid battery and it was invented by Gaston Planté, a French physicist, in 1859.¹ The disadvantage of this battery in comparison to other batteries was that it was heavy and bulky for the amount of the energy it could store. In the late nineteenth century, nickel-cadmium (Ni-Cd) rechargeable batteries were commercialized in Sweden. This was the first alkaline battery which had nickel and cadmium electrodes in a potassium hydroxide solution. Ni-Cd batteries have larger energy densities ($60 - 100 \text{ Wh L}^{-1}$) than lead-acid batteries ($50 - 80 \text{ Wh L}^{-1}$). The nickel-metal hydride battery (Ni-MH) appeared in the market after some decades of commercialized Ni-Cd batteries around 1989. It has a positive electrode of nickel oxyhydroxide (NiOOH) like Ni-Cd, but the anode material is a metal hydride instead of cadmium. Ni-MH batteries have larger energy densities ($170 - 430 \text{ Wh L}^{-1}$) and are more environmentally friendly as they do not have a toxic cadmium electrode. In the early nineties, a very promising battery was published by Sony, Li-ion batteries. Various types of electrode materials were used in Li-ion batteries, such as graphite for anode and LiCoO_2 for cathode when it was successfully commercialized. There are several other types of electrode materials which were tried in Li-ion batteries. Graphite materials are the dominant active anode material used in lithium-ion batteries. The performance of graphite is as being a safe and good reversible material that provides high energy density for many portable electronic devices. Moreover, LiCoO_2 received tremendous attention when it was successfully commercialized. Even though there have been some successful improvements in the electrochemical performance of LiCoO_2 by years, alternatives (e.g. Lithium iron phosphate LiFePO_4 , manganese spinels, lithium nickel manganese cobalt oxides) are also widely used due to LiCoO_2 's high cost, toxicity and poor safety.

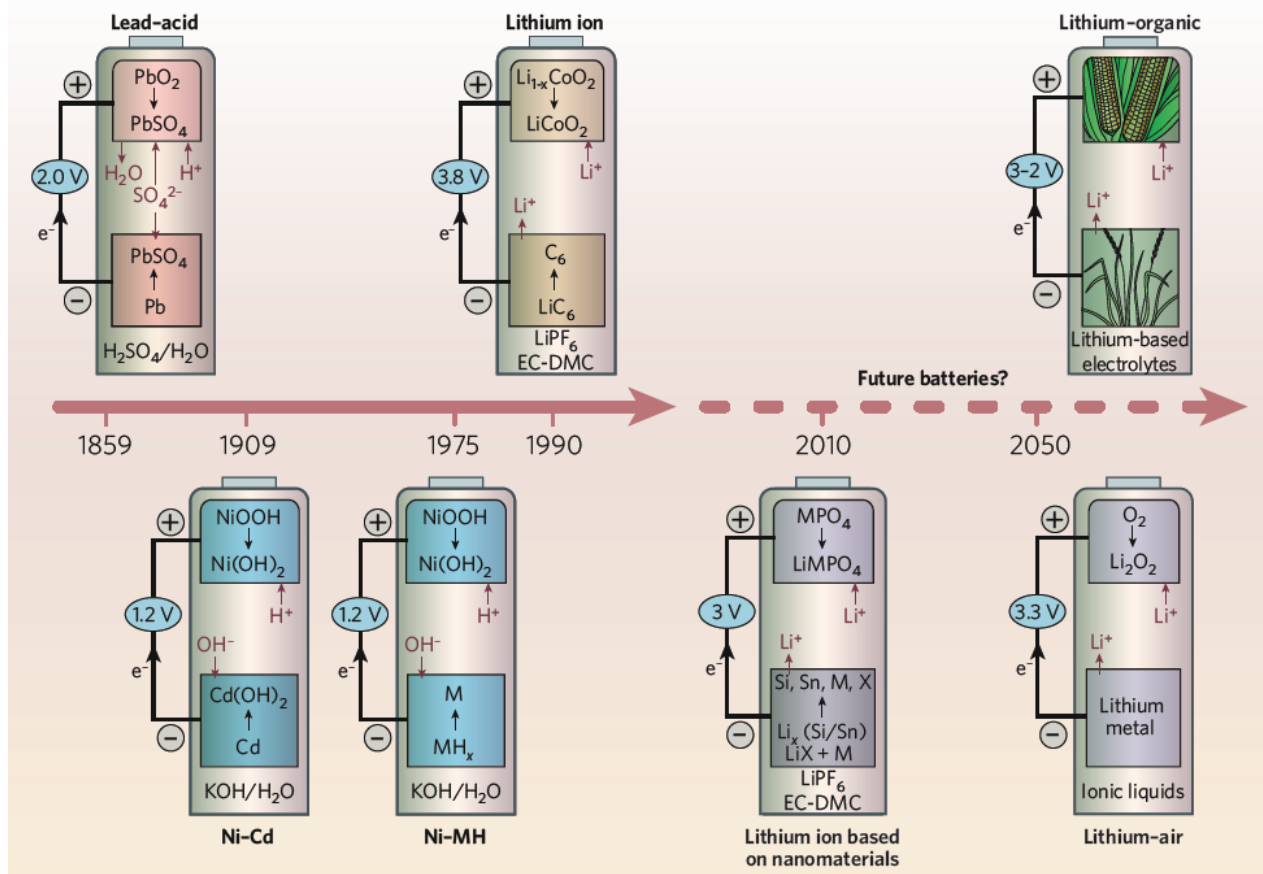


Figure 2-2 Development of some battery chemistries³

Li-ion batteries are promising alternative energy storage systems for electric vehicles as well as portable electronic devices. However, it is necessary to extend the driving range of electric cars while reducing their cost. The driving range is directly related to energy density of a battery that is the capability of providing power over time. A typical driving range for an EV, such as BMW i3 or Volkswagen e-Up, is around 130 – 160 km per charge of battery pack (Li-ion) with an energy density of 75 – 100 Wh kg⁻¹.^{4,5} For a comparison, conventional ICE vehicles provide a range of 480 – 650 km powered by gasoline with a theoretical energy density of 13,000 Wh kg⁻¹.¹ The driving range depends on the type of battery and is highly affected by the electrochemistry of the battery. Basically, batteries which are capable of storing higher electrochemical energies, provide a longer driving range. That being said, increasing the energy density brings another problem, which is cost. Complex systems or expensive materials are needed for higher energy

densities. This is a disadvantage in terms of battery cost. Therefore, cost, storage density, lifetime and safety must be improved. For that reason, new types of batteries are taken into account, such as metal-air batteries. The electrochemical coupling of a metal anode to an air electrode may result in very high specific energy and power density. The advantage of such systems is having an inexhaustible cathode reactant, such as oxygen. A summary of major advantages and disadvantages of metal-air batteries is given in Table 2-1. Moreover, a comparison of theoretical energy densities and practical energy densities between the metal-air batteries (e.g. Zn-air, Li-air) and other types of batteries is shown in Figure 2-3. Theoretical energy density is based on thermodynamics while practical energy density is based on experimental results. The experiments are performed by drawing some amount of current from the battery. This process may result in pore clogging by precipitation, passivation of active surface or irreversible reaction products. Due to these effects and insufficient kinetics of oxygen reduction reaction, the practical energy density can only reach 1 order of magnitude lower values than the theoretical energy density. To improve practical energy density, one needs to either develop new batteries with higher theoretical energy density or optimize the structure of current batteries. Another fact that can be seen from Figure 2-3 is the energy density difference between the gasoline and the current commercialized batteries, such as Li-ion. It is impossible that the current batteries will come close to target value $1,700 \text{ Wh kg}^{-1}$ which is the practical energy density of conventional ICE vehicles. Therefore, metal-air batteries have attracted much attention as an alternative to current batteries, because the energy they can store is extremely high compared to that of other rechargeable batteries.

Table 2-1 Major advantages and disadvantages of metal-air batteries¹

Advantages	Disadvantages
High energy density	Limited power output
Flat discharge voltage	Reversibility of discharge products
Long shelf life	Pore clogging by discharge products
No or small environmental problems	Instability of contacting to air
Low cost	

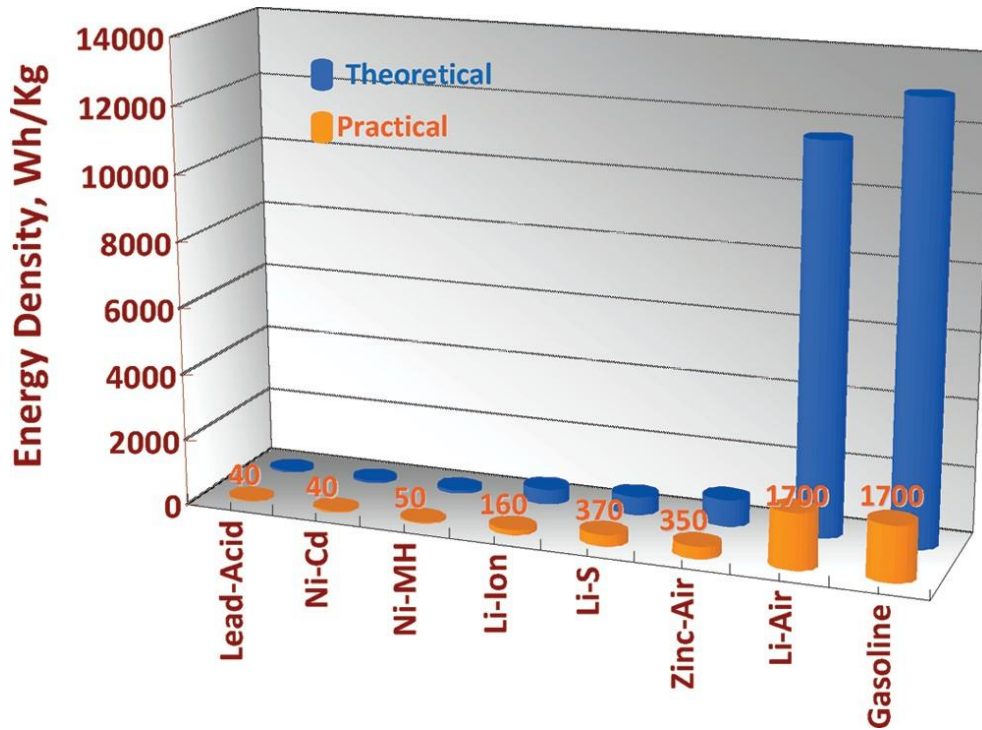


Figure 2-3 The gravimetric energy densities for various types of rechargeable batteries and the gasoline. Theoretical energy densities are based on thermodynamics.⁶

Several types of metal-air batteries based on various anode electrodes have been researched already. Reaction mechanisms, electrolytes and cell designs (i.e. cylindrical, button, prismatic and pouch cell) may differ for each type of metal-air batteries. A brief comparison of metal-air batteries in terms of open circuit voltage and theoretical specific energy density is given in Table 2-2. Metal-air batteries are classified into two main groups depending on the electrolyte. One is a system using a liquid electrolyte and the other one is using a solid electrolyte. Liquid electrolytes are commonly used and include aqueous and non-aqueous electrolytes. Aqueous electrolytes have the advantage of not being degraded by moisture, while non-aqueous electrolytes can be sensitive to moisture. The chemistry of metal electrode restricts the choice of the electrolytes that should be used in the battery. Additionally, the metal electrode may react with electrolytes resulting in decomposing the electrolyte or degrading the electrode. Metals such as Ca, Al, Fe, Cd and Zn are appropriate for aqueous electrolyte systems. When the first Li-air battery was realized in 1996 by Abraham et al., a non-aqueous electrolyte was used since Li metal is highly reactive with water.⁷

Table 2-2 A comparison of metal air batteries.^{6,8,9} Only the masses of the active reactant materials are included. The specific energy values are given for the cases of inclusion and exclusion of O₂.

Type	Open circuit voltage at 25 °C / V	Theoretical specific energy density / Wh kg ⁻¹	
		O ₂ mass included	O ₂ mass excluded
Li/O ₂	2.96	5,200	11,140
Al/O ₂	2.73	4,300	8,130
Na/O ₂	1.94	1,677	2,260
Mg/O ₂	2.93	2,789	6,462
Ca/O ₂	3.12	2,990	4,180
Zn/O ₂	1.65	1,090	1,350
Si/O ₂	0.8 – 1.1 (practical), 2.2 V (theoretical)	5,360	8,470

Each type of metal-air battery concept has some advantages and disadvantages. Depending on application, environment, external effects etc., the proper battery can be chosen. Up to now, Zn-air and Li-air batteries have attracted most attention. More information about these two batteries will be given in the next sections.

There are some technological and scientific problems that metal-air batteries suffer from as other battery technologies do. These problems are caused mainly by the performance of positive and negative electrodes and result in low practical energy density, low cycle life, low power density etc. Some examples regarding anode issues are: passivation of the metal surface and corrosion of the metal in contact to electrolytes, the accumulation of some reaction products etc.¹⁰ These effects may retard the electrolyte access into electrode and prevent further discharging. Cathode issues are; slow kinetics, poor reversibility of oxygen chemistry, side reactions etc. Also, electrolyte can be unstable and decompose at the cathode electrode (at ORR and especially OER conditions).¹¹⁻¹³ Moreover, in some cases, the air cathode suffers from the catalysts that are used for the oxygen reduction reaction (ORR). These catalysts may speed up decomposition of the electrolyte resulting in a passivation layer that covers the surface of the catalysts. This layer prevents the catalysts active material and it is no longer used for any reactions.^{9,14,15} Because some of the mechanisms underlying cathode reactions have not been understood well yet, cathode is considered as the main reason for the failure most of the times.

Although using an air cathode seems very promising and attractive, it appears to be the most expensive, complicated and bulky component of a battery system.¹⁶

As a result, to make metal-air batteries useable in real life and an alternative to other batteries, the important tasks are as follows: oxygen chemistry should be fully understood and the kinetics of the electrochemical oxygen reduction reaction (ORR) and/or oxygen evolution reaction (OER) should be accelerated, electrolyte should be stable on anode and cathode side, the underlying mechanisms of anodic problems (passivation, corrosion etc.) need to be investigated. In the last years, researchers have put much effort on the cathode reaction mechanisms and on the development of efficient catalytic materials for ORR/OER.^{6,10} Furthermore, a new material, alloy, structure or electrolyte could be found and can be the solution to all these problems mentioned above in the coming years.

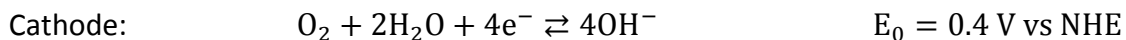
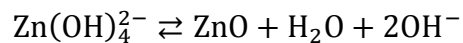
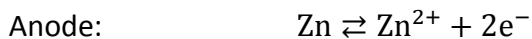
Recently, a new type of metal-air battery was explored at the Technion-Israel Institute of Technology. The silicon-air battery is new, environmentally friendly, and capable of supplying power for thousands of hours.¹⁶ By using silicon metal, the anode electrode is safe, non-toxic, stable and very lightweight with long shelf life. Silicon-air batteries have high energy densities comparable to other metal-air batteries (see Table 2-2). Moreover, silicon is the second most abundant element in the earth's crust. Also, the reaction product of silicon with oxygen silicon dioxide SiO_2 can be handled and disposed without any special requirements. Potential applications of the primary silicon-air battery include medical applications, i.e. powering diabetic pumps or hearing aids, sensors and microelectronics structured from silicon. Furthermore, according to the inventor of silicon-air battery, Prof. Ein-Eli, it may be possible to use silicon-air batteries in terms of portable devices, transportation, and military applications in the next few decades.¹⁷ The focus of this thesis lies on these silicon-air batteries, as discussed in detail in the next chapter.

2.1 Zinc-Air Battery

Zinc metal has been used as anode in batteries for many years. Primary zinc-air batteries are commercially available since 1970s.¹ The use of zinc-air batteries has been explored in telecommunications, military, industry and medical applications. Especially in medical applications, zinc-air batteries have been used for hearing aids for more than 30 years.

Zinc received great attention among other potential metal-air batteries, because it is one of the most electropositive metals. It provides the advantage of being relatively stable in aqueous and alkaline electrolytes. Rechargeable zinc batteries are the center of interest for many studies. There has been a lot of research for several decades. Because of having low equilibrium potential, reversibility, compatibility with aqueous electrolytes, low equivalent weight, high specific energy, abundance, low cost, low toxicity and easy handling, zinc is one of the most commonly used battery electrodes.¹⁸ Another advantage of alkaline zinc batteries is that non-noble metal catalysts can be used for the ORR.¹⁹

The half-cell reactions and the global reaction of alkaline zinc batteries are:¹⁹



The schematic of a typical Zn-air battery is shown in Figure 2-4. There are three main parts in the cell; a zinc metal as anode, a separator, and an air electrode as cathode. The air cathode is composed of two parts, a gas diffusion layer and a catalytic active layer. The working principle of such batteries is the same as the other types of metal-air batteries, such as Li-air etc.⁶

In metal-air batteries, oxygen is reduced on the air cathode and the metal anode is oxidized and dissolved by interacting with electrolyte. In Zn-air batteries, these processes are as follows: Oxygen taken from the atmosphere diffuses from the porous air electrode and is reduced to hydroxyl ions in the alkaline electrolyte by the help of catalysts. The electrons needed for this reaction are generated from the oxidation of the zinc metal anode. Hydroxyl ions, which are produced as a result of the cathodic reaction, migrate to zinc metal anode and produce zincate ion Zn(OH)_4^{2-} by reacting with zinc cations. When the zincate ion exceeds its saturation limit in the alkaline electrolyte, it starts decomposing to ZnO . ZnO is an insulating white powder that is deposited in the cell.

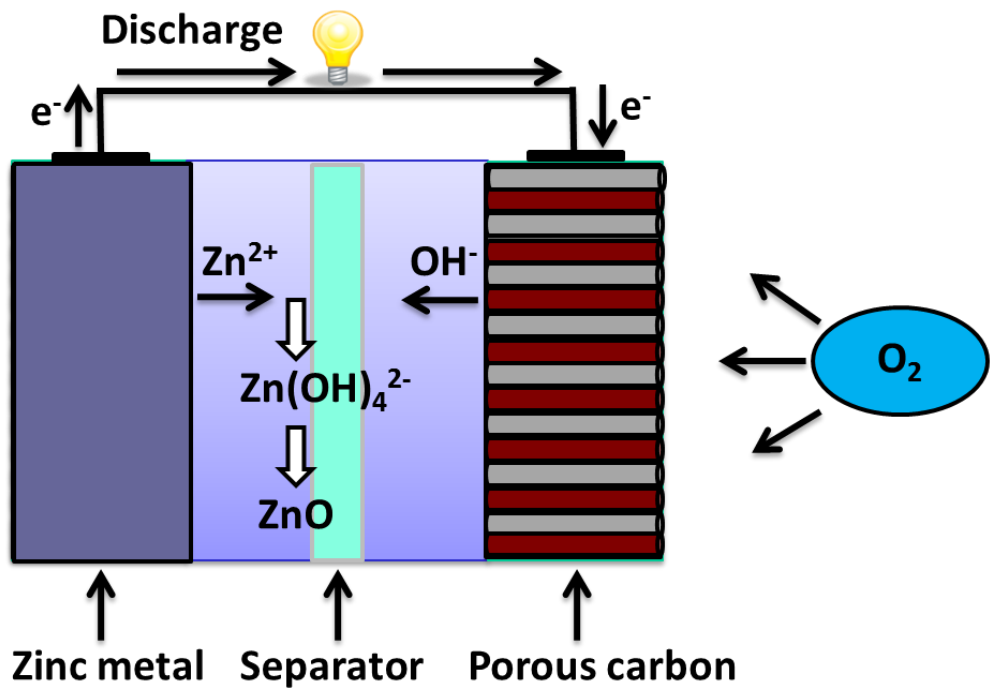


Figure 2-4 Schematic representation of a zinc-air battery

The equilibrium potential of a zinc-air battery should be 1.65 V, theoretically. In practice, due to internal loss of the cell, such as activation loss, ohmic loss and concentration loss, the operating voltage is less than 1.65 V. The electrochemical behavior of zinc-air batteries is described by Lee et al.¹⁹ through a polarization curve schematically shown in Figure 2-5. The discharge, charge,

operating potentials, as well as the overpotentials of the electrode reactions are depicted in the figure. One can see that the overpotential is higher at the air electrode than the anode, and thus, the cathodic reaction is the main origin of potential loss. To be able to generate hydroxyl ions by ORR, the battery needs a high overpotential at the cathode. Due to this overpotential, the working voltage is less than 1.65 V. In charging process, the direction of the currents is reversed as expected. In this case, the needed voltage for the oxygen evolution reaction (OER) is higher than 1.65 V.¹⁹

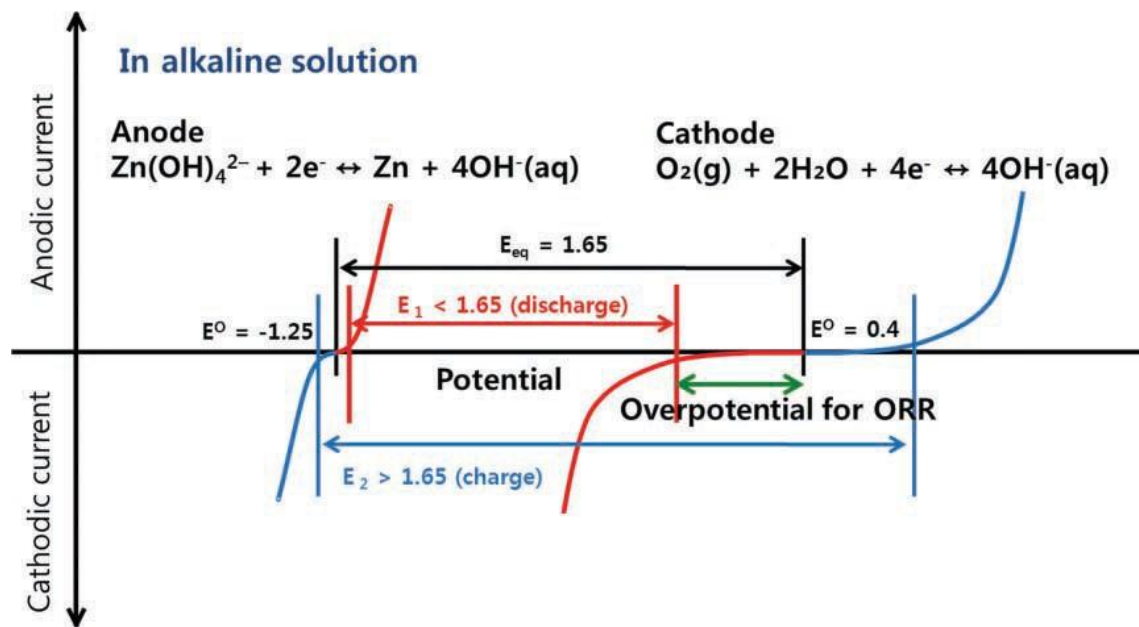


Figure 2-5 The polarization curves of the anodic and cathodic reactions¹⁹

From the discussion above, it is clear that the main reason for the potential drop is the air cathode and that is why many studies have focused on how to improve the air electrode. However, this is not enough to make zinc-air batteries rechargeable. The electrochemical behavior of zinc anode, the cathodic overpotential, the use of KOH solutions as electrolyte, and the deposition of ZnO solid powder are the main challenges for rechargeable zinc-air battery researchers. To lower the charging electric potential, zinc-air batteries need a bifunctional catalyst.¹⁹ Also, making the zinc metal anode reversible is vital. Because it is known that zinc metal undergoes morphological changes during discharge. This process is caused by the formation of dendrites in the Zn-air battery.¹⁸ Dendrites are unwanted morphologies in any type

of batteries and may cause huge problems. These dendrites can penetrate the separator and then cause a short circuit in the battery and may result hazardous effects. As a result of the ZnO morphology change, zinc metal can become partially inactive and the anodic zinc dissolution would stop. Moreover, the aqueous electrolyte can react with air in an open system and lead to the formation of potassium carbonate on the cathode side.²⁰ This process results in pore clogging in the air cathode. On the other hand, the discharge product ZnO can block the electrolyte pathway and prevent further hydroxide ions diffusion into the anode.²¹ Eventually, the active surface area of the electrodes can be lowered with these processes. Furthermore, the corrosion process of the zinc metal in an alkaline solution can generate hydrogen gas according to $\text{Zn} + 2\text{H}_2\text{O} \rightleftharpoons \text{Zn}(\text{OH})_2 + \text{H}_2 \uparrow$.^{19,22} This hydrogen evolution process is undesirable since it leads to self-discharge of zinc metal.

To overcome the challenges of rechargeable zinc-air batteries, many studies were done and found that several approaches are possible. Using an ionic liquid, which is a non-aqueous electrolyte, may retard the formation of dendrites.²⁰ Because the dendrite formation is a result of the interaction between zinc metal anode and electrolyte, using an ionic liquid may result in dendrite-free metal deposition. Moreover, the cathode materials need improvement as well. Up to now, some mechanisms have not yet been fully understood about the air electrode. Using a new catalysts and/or changing the design of the cathode may be the solution for the cathodic obstacles. Also, coating, alloying or adding additives to the electrolyte might be a solution to overcome hydrogen evolution reaction problem on anode electrode.¹⁹

There was a promising progress in the area of zinc-air batteries over the past decades. Although having some challenges, these batteries are still of interest for many studies. Low cost, high energy density, electrochemical performance, easy handling, environmentally friendliness are the reasons for zinc-air batteries to preserve their attractiveness. But, before these batteries can be commercially applied in several fields, such as mobile and portable systems, further investigations are required to overcome those challenges.

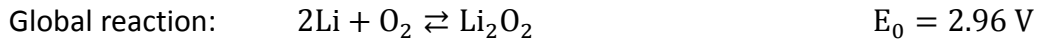
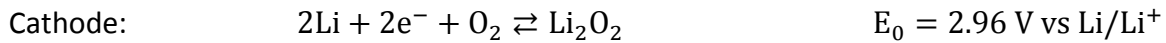
2.2 Lithium-Air Battery

Today, lithium-ion batteries are widely used in our daily life as power sources for laptop computers, mobile phones, music players, digital cameras, and many other electronic devices. Despite their success and widespread usage, there is an increasing need for batteries with higher densities than today's commercialized batteries, especially in the automotive industry. Herein, lithium-air batteries come to the forefront. A lithium-air battery could potentially provide three to five times higher energy densities than conventional Li-ion batteries (160 Wh kg^{-1}). Because the driving range of an electric vehicle will be extended by using lithium-air battery and become comparable to gasoline vehicles, they captured worldwide attention in the past few years. If the system is successfully developed, the dependence on gasoline will be decreased and thus it will be a part of a solution for global climate change due to CO_2 emissions. 34 % of the world's primary energy demand is covered by oil, which results in approximately 40 % CO_2 emission with a big influence on global climate change.²³

The specific capacity of lithium-air batteries are the highest among all kind of batteries (see Table 2-2). Together with other advantages, this makes lithium-air batteries one of the most attractive alternative energy storage systems. Although the first studies were done in 1996 by Abraham et al.⁷, most of the work was performed in the past few years. Studies mainly focused on cathode and electrolytes; different types and structures of materials, catalysts, and electrolytes were investigated in order to improve the performance and to overcome some obstacles.^{10,24}

Currently, there are different versions of lithium-air batteries based on the electrolyte: 1) non-aqueous Li-air battery utilizing organic liquid, polymer or ionic liquid electrolytes, 2) aqueous Li-air battery, 3) solid-state Li-air battery utilizing a Li^+ conductive inorganic solid electrolyte separator, 4) mixed Li-air battery utilizing both non-aqueous and aqueous electrolytes.⁶ Since lithium-air batteries are not the scope of this thesis, only the non-aqueous electrolyte type is discussed in detail because it attracts the widest interest.

The half-cell reactions and the global reaction of non-aqueous lithium-air batteries are given below:⁶



The schematic of a non-aqueous lithium-air battery is shown in Figure 2-6. It consists of a lithium metal as anode, an air electrode as cathode and a non-aqueous electrolyte. According to Abraham et al.⁷ reaction mechanisms, which are also given above, are as follows: An oxidation reaction of lithium metal occurs in the anode during discharge. Lithium ions, the product of the oxidation reaction, are transported to the cathode by electrolyte. At the same time, electrons flow through an external circuit to the cathode. In the cathode, oxygen taken from the ambient air is reduced by lithium ions and electrons to Li_2O_2 . By calculating the thermodynamics of reactions, the discharge potential is calculated as 2.96 V. Since the reaction products, lithium oxides, are insoluble in the electrolyte, they are stored in the pores of the carbon electrode, and the discharge of the cell theoretically ends when these pores are completely filled with the oxides. Some authors have reported that the production of Li_2O is also possible.^{25,26} Since twice lithium per oxygen is needed for Li_2O , it will increase the energy stored. However, the downside of Li_2O is that it is not easily reversible. If an external voltage, which is higher than 2.96 V, is applied to the cell, the discharge reaction can be reversed. Some studies have been done to observe whether Li_2O_2 deposits dissolve during the charging process or not. Results show that Li_2O_2 dissolves and there is an oxygen evolution at the cathode during charging.^{7,27} This is why researchers do believe that lithium-air batteries are rechargeable. Moreover, the lithium anode which is in contact with the electrolyte can form a stable solid electrolyte interface (SEI).⁶ SEI makes the electrolyte-lithium metal interface stable that is good for the battery performance.

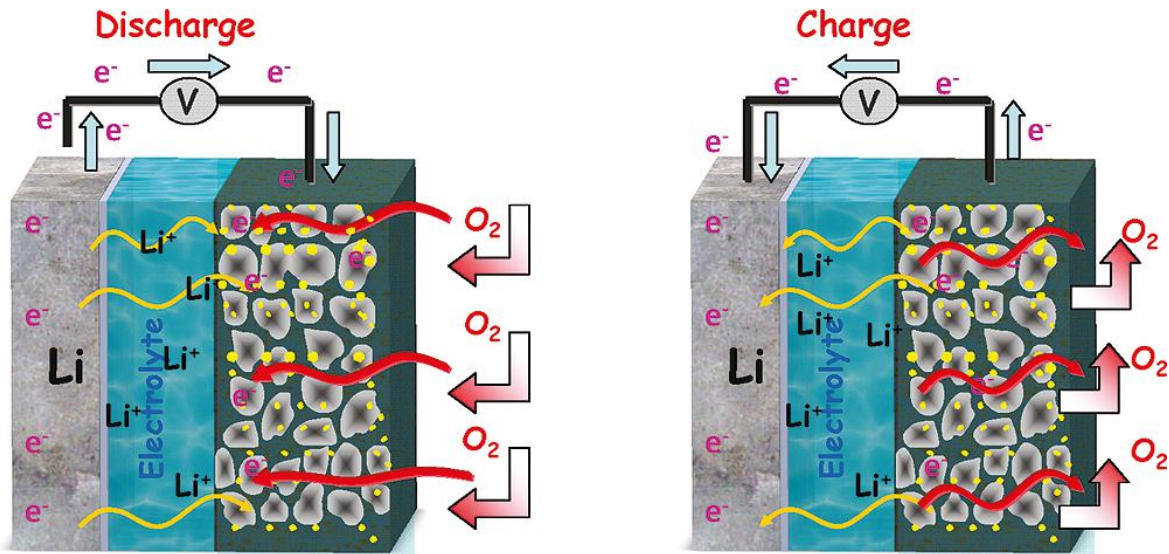


Figure 2-6 Schematic representation of a Li-air battery⁶

A discharge-charge cycle of a lithium-air battery is shown in Figure 2-7. The operating potential and the charging potential, as well as the overpotentials are shown in the figure. The difference between the open circuit voltage (OCV) and the operating voltage is defined as discharge overpotential (η_{dis}). The difference between the charging potential and the OCV is called charge overpotential (η_{chg}). One can see in Figure 2-7 that the discharge potential is around 2.6 – 2.7 V due to the activation and ohmic losses. Also, the cell potential increases up to 4.0 V when the cell is charged with a constant current.

The overpotentials mentioned above are challenges for the researchers. In order to improve the performance of the battery, people try to overcome these overpotentials by using electrocatalysts.²⁸ By using catalysts, not only the overpotentials will be reduced, but the electrical and thermodynamic efficiency together with the discharge capacity will be increased remarkably.

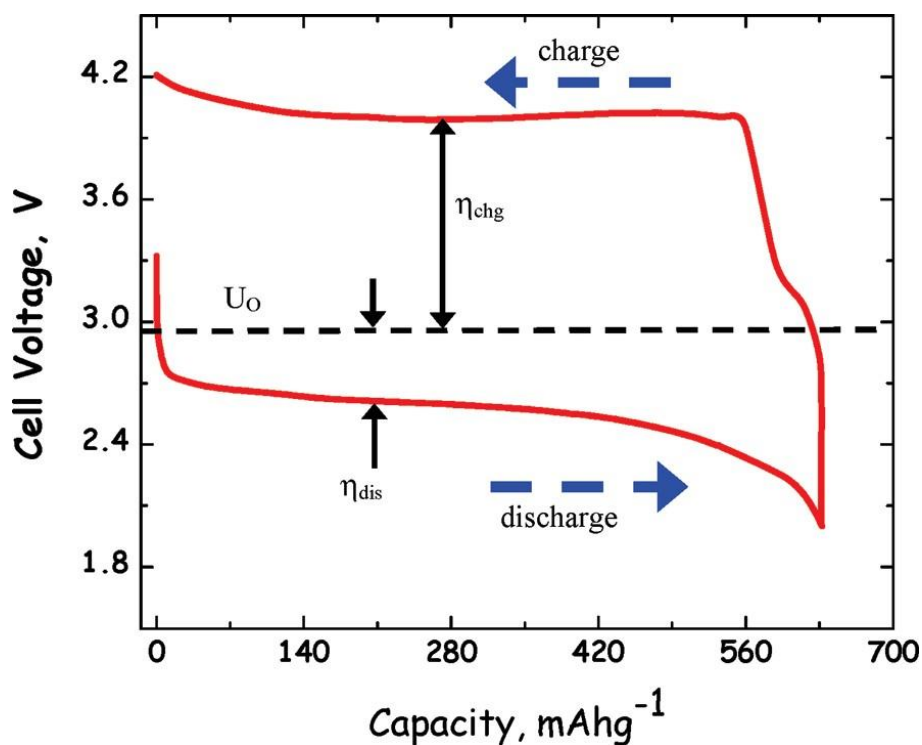


Figure 2-7 A single measured discharge-charge cycle for an aprotic Li-air cell (based on SP carbon) operated at $\sim 0.1 \text{ mA cm}^{-2}$ current density⁶

There are several challenges, some of them are mentioned before, to make lithium-air batteries rechargeable. The major challenges of rechargeable lithium-air batteries are summarized in Figure 2-8.²⁹

Lithium metal is the most promising anode material for lithium-air batteries among all the anode materials. Due to having the most electropositivity (-3.04 V vs SHE), lithium metal is expected to have a high energy density. Also, lithium metal is the lightest metal (equivalent weight = 6.94 g mol^{-1}) and it has an extremely high specific capacity ($3,860 \text{ Ah g}^{-1}$).³⁰ Even though having these advantages, lithium metal anodes suffer from some important problems. The first one is the dendrite growth during charge-discharge cycles.^{31,32} Dendrites can lead to internal short circuits of the battery, as a result in hazardous safety issues. Furthermore, the dendritic lithium can be ruptured and isolated from the anode during the discharge. This process causes a loss of anode materials and leads to a shorter cycle life. Therefore, to operate lithium-air batteries with lithium metal anodes, this challenge must be overcome. In order to

solve this problem, several studies were done: homogenous highly conductive artificial protective layers are developed⁶ (but still no layer is found that is safe and has sufficient conductivity), new electrolytes including ion conductive glass or glass-ceramic materials have been developed.³³ The second important obstacle is the low charge-discharge efficiency.³⁴ Dendrite growths is also a reason of the low charge-discharge efficiency, since it can lead to shorter cycle life.

Another important obstacle is the electrolyte decomposition on the cathode electrode. Some studies show that the discharge products are lithium alkyl carbonates Li_2CO_3 , and lithium alkoxides rather than Li_2O_2 due to electrolyte decomposition.^{6,11-13} Oxygen also participates in the formation of Li_2CO_3 by reacting with organic electrolytes.^{11,35} Formation of lithium carbonates is undesirable due to: Organic electrolyte is decomposed and consumed by producing Li_2CO_3 , and high voltages ($> 4 \text{ V}$) are needed to decompose Li_2CO_3 . This is the reason of high charge overpotential shown in Figure 2-7. On the other hand, formation of Li_2CO_3 strongly depends on the electrolyte. In order to prevent electrolyte decomposition, new electrolytes should be researched. However, it is not an easy task to find an electrolyte which does not decompose on cathode side and is stable on anode side at the same time.

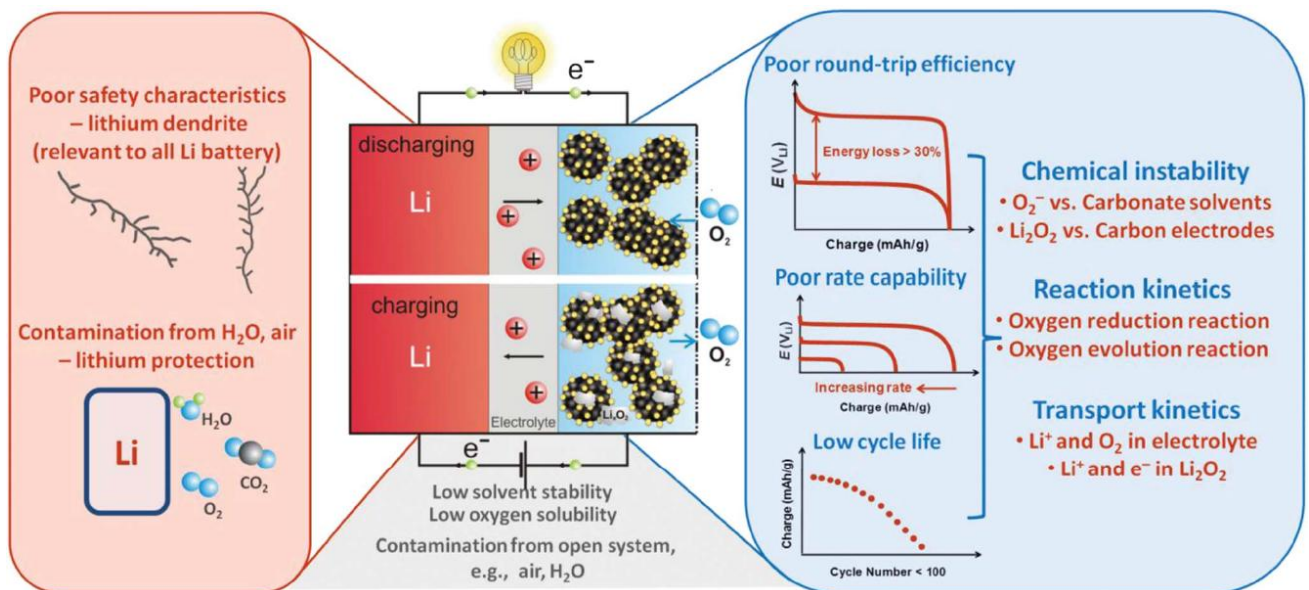


Figure 2-8 Major challenges for rechargeable Li-air batteries²⁹

Electrolyte has a massive role in making lithium-air batteries rechargeable. The electrolytes used in lithium-air batteries should have the following characteristics:^{6,36}

- 1) High stability in the open system³⁷
- 2) High chemical stability on anode and cathode
- 3) High oxygen solubility and diffusivity³⁸

Most of the experiments about investigation of electrolytes have been performed in a closed system (oxygen-starving environment with no other impurities). But, it is known that metal-air batteries are an open system (oxygen-rich environment with some other impurities) since the air electrode takes oxygen from the ambient air. Therefore, these experiments have to be re-performed in an open system, contacting directly with air. Because air does not include only oxygen molecules, it may cause some problems, such as extra reactions, contamination, impurities etc. Also, the electrolytes need to be non-sensitive to moisture. To be able to stand long term battery operations, electrolytes should be chemically stable to prevent decomposition and reacting with the electrodes of the battery (i.e. Li_2CO_3 formation). The reasons for the battery termination in many cases are mainly originated from the Li_2CO_3 formations or Li_2O_2 passivation layer.¹⁵ In the case of Li_2O_2 deposition, the capacity of battery is limited by the Li_2O_2 layer. Since Li_2O_2 is insoluble in non-aqueous electrolytes, deposition of Li_2O_2 builds up a layer on the cathode electrode. When this layer exceeds a critical thickness, the electron transfer to the Li_2O_2 – electrolyte surface cannot be sustained. For this reason, the electrochemistry in the cathode electrode cannot be supported anymore, and it leads to discharge termination at low capacities. Moreover, solubility and diffusivity of the oxygen are crucial for the battery operation as well. By adding some additives, the solubility of oxygen in the electrolytes can be increased. Unfortunately, no perfect electrolyte has been found to meet all these requirements so far.

In lithium-air batteries, $\text{Li} - \text{O}_2$ reactions (ORR and OER reactions) take place on the carbon substrate. Therefore, air cathode has an extreme importance on the battery performance. Main challenges regarding to air cathode are as follows: pore clogging by Li_2O_2 precipitation, Li_2O_2

passivation layer, instability with non-aqueous electrolytes, reaction kinetics and transport kinetics.^{15,39,40} It has been proposed by many authors that the energy storage capacity and power capability of Li-air batteries are mostly determined by the accumulation of discharge products, stability of electrolyte and the air electrode.^{15,39,40} Electrode material and design of the air cathode also influence the battery performance significantly.⁴¹ Furthermore, since a Li_2O_2 layer on the cathode surface is electronically insulating, impedance of the cathode increases after discharge due to accumulation of Li_2O_2 . The amount of stored Li_2O_2 increases as the depth of discharge increases. A fraction of this stored Li_2O_2 may locate farther away from the carbon cathode surface and loses electronic contact with the surface, and then it becomes unable to be oxidized. The amount of the isolated Li_2O_2 increases with depth of discharge process. Therefore, if the thickness of Li_2O_2 passivation layer can be controlled, it would be a way to increase Li-air battery rechargeability. In addition, O_2 diffusivity plays an important role regarding to the Li_2O_2 precipitation which leads to pore clogging on the air electrode. If the oxygen transport cannot be supplied from the air side through the carbon electrode (due to the clogged pores), the discharge ends in a short span of time and leads to a lower discharge capacity. Furthermore, the morphology of discharge product Li_2O_2 is another obstacle which affects the discharge capacity. Recent experiments show that the discharge product can deposit in various morphologies, such as complex toroid-like, thin film, disc-shape etc.⁴²⁻⁴⁷ These morphologies can play important role on the following: Pore clogging, surface passivation, electronic conductivity, kinetics of the oxygen reactions etc.

In summary, Li-air batteries possess the highest theoretical energy density among all batteries. However, making lithium-air batteries rechargeable is also extremely challenging due to the electrolyte decomposition, Li_2O_2 passivation layer, and lithium dendrites etc. Up to now, Li-air batteries are promising systems for as alternative drive train system replacing internal combustion engines. Therefore, further investigations and understandings of the mechanisms are mandatory and crucial.

Chapter 3 : SILICON-AIR BATTERIES

As mentioned above, a new type of metal-air battery, Si-air battery, has been developed recently.^{16,48,49} There are only a few studies published on Si-air batteries, but the results are promising. As a starting point, a primary Si-air battery is considered by researchers. It is difficult to make silicon-air batteries rechargeable as the discharge product SiO_2 is very stable and high voltages are needed in order to decompose it. Hence, there should be more research done to understand all the mechanisms taking place inside the battery and the challenges should be overcome to make silicon-air batteries rechargeable.

There are several advantages which make this system attractive: Firstly, silicon is a thermodynamically favorable fuel for a battery system since the Si-air combination possesses a specific energy of $8,470 \text{ Wh kg}^{-1}$ and an energy density of $21,090 \text{ Wh L}^{-1}$.⁹ Secondly, silicon is the second most abundant element in the earth's crust, which results in a low-cost battery system. Moreover, the Si-air battery system is environmentally friendly and inherently safe because of both silicon and its reaction product with oxygen are safe, nontoxic, and easy to handle.

In the following section, we review the available experimental results on primary silicon-air batteries. It is important to discuss these experiments since our model includes the mechanisms and parameters from these studies.

3.1 Literature Review

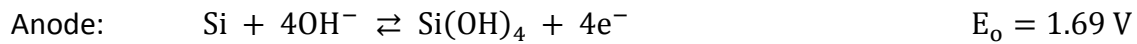
Silicon-air batteries with room temperature ionic liquid (RTIL), alkaline solutions, and composite polymer electrolyte are proposed in the literature.^{9,16,48,50-52} The results by employing a room temperature ionic liquid are more promising than the other types of electrolytes. Therefore, RTIL is considered as an electrolyte of the model in this thesis.

A group from University of California investigated a primary Si-air battery system by using an alkaline solution.⁵⁰ The battery system is able to provide an operating potential

between 0.9 to 1.2 V, with current densities of 0.01 to 0.1 mA cm⁻². Moreover, a self-capacity around 1,206 mAh g⁻¹ is achieved. The battery system consists of a surface modified silicon wafer as anode, an air electrode as cathode, and variable concentrations of potassium hydroxide solution as electrolyte.

A modification on the silicon surface by the metal-assisted electroless etching process was used in their studies. This process creates microporous layer silicon nanowires on top of the silicon surface; therefore the roughness of the silicon surface was increased significantly. Then, this prepared silicon substrate was used as the anode in the battery system. A typical discharge curve is shown in Figure 3-1a. The result by employing an unmodified silicon anode is shown in Figure 3-1b. Figure 3-1a presents the discharge in 30 hours, while Figure 3-1b shows the discharge in 400 seconds. These figures clearly indicate that the modification on the silicon surface is crucial and it significantly affects the discharge capacity of the battery.

The electrochemical reactions of the anode and cathode are:



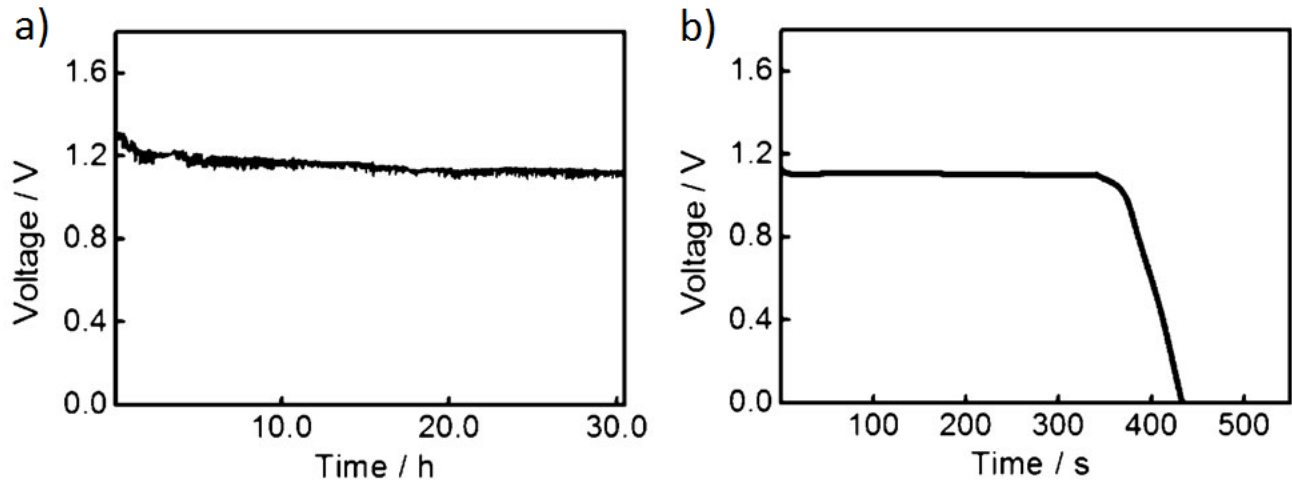


Figure 3-1 Discharges profiles of silicon-air battery with an alkaline solution: a) Galvanostatic discharge curve of a modified silicon-air battery with a discharge current density of 0.05 mA cm^{-2} . b) Galvanostatic discharge curve of an unmodified silicon-air battery with a discharge current density of 0.05 mA cm^{-2} .⁵⁰

The anode reaction product Si(OH)_4 can build up on the silicon surface and results in a formation of SiO_2 which passivates the surface. Therefore, the product Si(OH)_4 needs to be removed from the silicon surface in order to ensure continuous discharge. The capability of dissolving Si(OH)_4 is the main benefit of employing an alkaline solution. Consequently, the surface of silicon anode is kept clean without passivation layer. Even in the presence of alkaline solution, the surface can be covered by silicon oxide if the dissolution rate of Si(OH)_4 is not fast enough. The increased surface area after the etching process accelerates this dissolution rate. On the other hand, for the unmodified silicon surface, the surface is covered by silicon oxide and passivated very quickly. That is why it has a very short discharge time. Further investigations and improvements in the cell design, material surface structure, electrolyte concentration, and air cathode are needed to fully understand all the mechanisms and allow designing such a battery with an alkaline solution.

Another study has been done on the Si-air batteries utilizing a composite polymer electrolyte.⁵¹ Gel polymer electrolytes (GPEs) have attracted much attention as electrolytes due to some advantages such as: highly safe, shape flexible, mechanically stable, and having a modest loss in ionic conductivity (comparing to pure liquids). The formation of GPEs is done by introducing a

liquid electrolyte into a polymeric matrix. This combination results in a solid structure with a good conduction mechanism. The ionic conductivity of GPEs is in the range of 1 mS cm^{-1} at room temperature.

The combination of the room temperature ionic liquid ($\text{EMI} \cdot (\text{HF})_{2.3}\text{F}$) and polymer composites are explored by Tsuda et al.⁵³ The compound of 2-hydroxyethyl methacrylate (HEMA) is used as monomer. The conductivity of such GPEs depends highly on the molar content of RTIL in the mixture. For 60 mol % RTIL, the conductivity was found to be 23 mS cm^{-1} , which is considerably lower than pure RTIL (100 mS cm^{-1}). In this study, GPEs with 40 mol % to 70 mol % RTIL have been employed to be able to satisfy ionic conductivity, mechanical stability, and flexibility at the same time.

The discharge curves of such battery are given in Figure 3-2, at a discharge current of 0.1 mA cm^{-2} . The operating potentials for different concentrations of RTIL are around 0.4, 0.5 and 0.6 V, respectively. However, these discharge potentials are significantly lower than pure RTIL electrolyte which is around 1.1 V. The effect of the molar content of RTIL on the discharge time is presented in the figure. The low ionic conductivity of the GPEs results in higher IR potential drop across the cell and causes such high voltage drops in the battery. Also, it is observed that the contact between the silicon anode and the GPE is inhomogeneous over the silicon surface. Thereby, the surface area for oxidation is lower than expected and it affects the performance of the cell.

A battery system utilizing a GPE has various advantages. But nonetheless, low operating voltage and low ionic conductivity remain important problems. In order to overcome these challenges, further experiments need to be conducted.

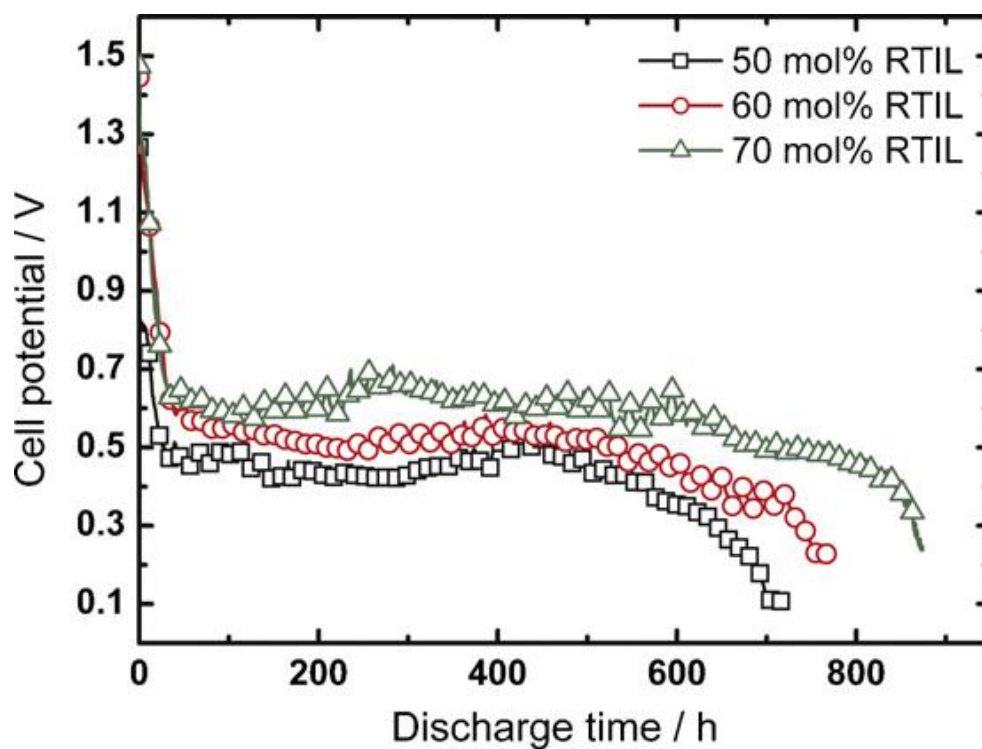


Figure 3-2 Discharge profiles of a silicon-air battery with a GPE as electrolyte⁵¹

In 2009, Ein-Eli et al. invented a Si-air battery system by utilizing a room temperature ionic liquid.¹⁶ Room temperature ionic liquids are relatively new electrolytes in electrochemical systems. Due to exhibiting wide electrochemical windows, high chemical and thermal stability, high ionic conductivity, low vapor pressure, low toxicity, and non-flammability they attract much attention. In 2002, synthesis of $\text{EMI} \cdot (\text{HF})_{2.3}\text{F}$ was reported by Hagiwara et al.⁵⁴ This electrolyte possesses the highest conductivity among all RTILs with 100 mS cm^{-1} . It consists of one cation (EMI) and two anions ($(\text{HF})_2\text{F}^-$ and $(\text{HF})_3\text{F}^-$). The typical ratio between these anions is 7:3. Moreover, the reaction of $\text{EMI} \cdot (\text{HF})_{2.3}\text{F}$ with n-type silicon forms a porous structure over the silicon surface. All these interesting properties make it desirable for silicon-air battery systems.

The schematic of the first experimental Si-air battery cell is shown in Figure 3-3. The cell comprised a heavily doped silicon single crystal wafer, an air electrode comprised with a polytetrafluoroethylene (PTFE) powder and carbon black structure catalyzed by manganese

dioxide pressed onto a nickel 200 mesh. $\text{EMI} \cdot (\text{HF})_{2.3}\text{F}$ is used as the electrolyte. From a thermodynamic point of view, the silicon-oxygen couple is very promising and attractive. The charge capacity of Si-air battery (3.816 Ah kg^{-1}) is very close to Li-air battery (3.86 Ah kg^{-1}). Also, the cell can exhibit high discharge capacities up to 53 mAh cm^{-2} at a current density of 0.3 mA cm^{-2} . The cell can be operated between $0.8 - 1.1 \text{ V}$ with current densities of 0.3 to 0.01 mA cm^{-2} , respectively.

During the discharge of the cell, silicon is oxidized at anode and oxygen is reduced at air cathode. The two anions of RTIL contribute to both reactions. Half-cell reactions, crystallization reaction, and global reaction are:

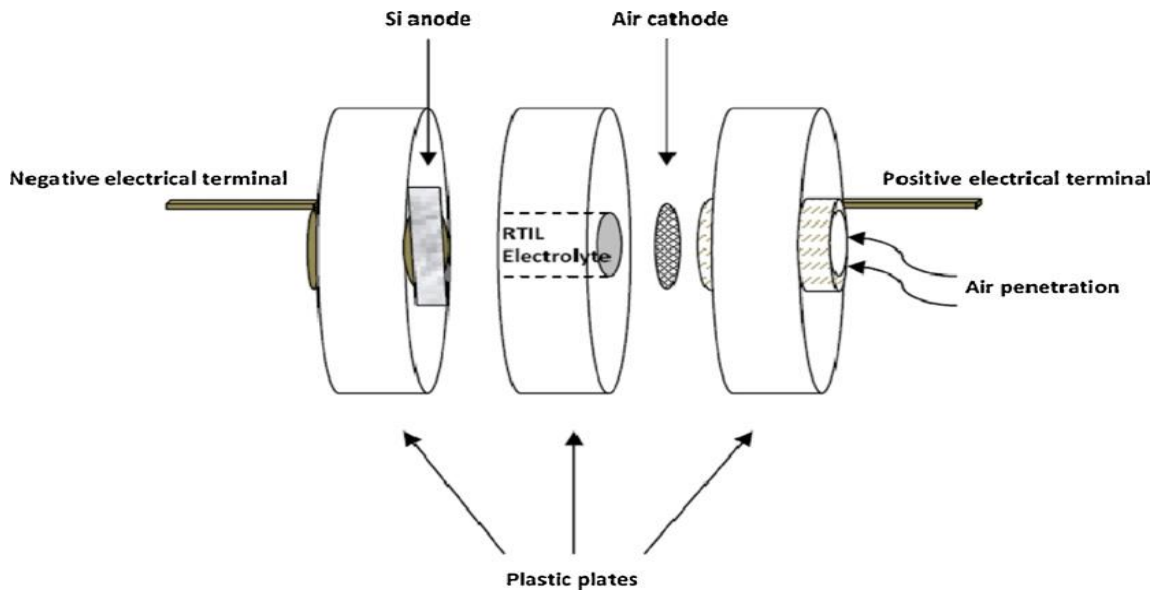
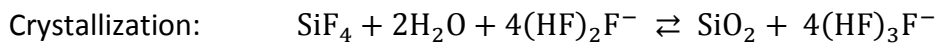
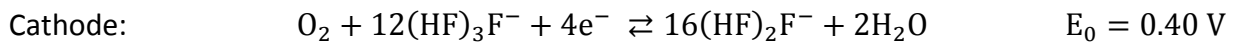
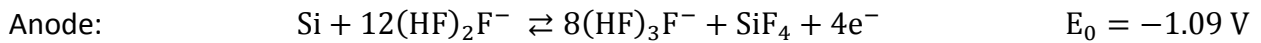


Figure 3-3 A schematic diagram of the silicon-air battery⁴⁸

In order to decide which Si type should be further studied; silicon corrosion rates and polarization voltammograms were investigated. The slow polarization voltammograms were recorded with EMI · (HF)_{2.3}F RTIL at 5 mV s⁻¹. Figure 3-4 shows the results of these voltammograms and Table 3-1 presents silicon corrosion rates for different wafer types. The corrosion rate affects the battery's shelf life; thus, a low corrosion rate leads to longer shelf life. On the one hand; n⁺⁺ silicon exhibits higher open circuit voltages (OCV) and relatively low corrosion rates, on the other hand, p⁺⁺ silicon have better cell voltage at high currents and lower corrosion rates compared to n⁺⁺ silicon. Even though n⁺⁺ silicon has higher corrosion rates, it was further studied due to having higher cell voltage at low currents in which the experiments run.

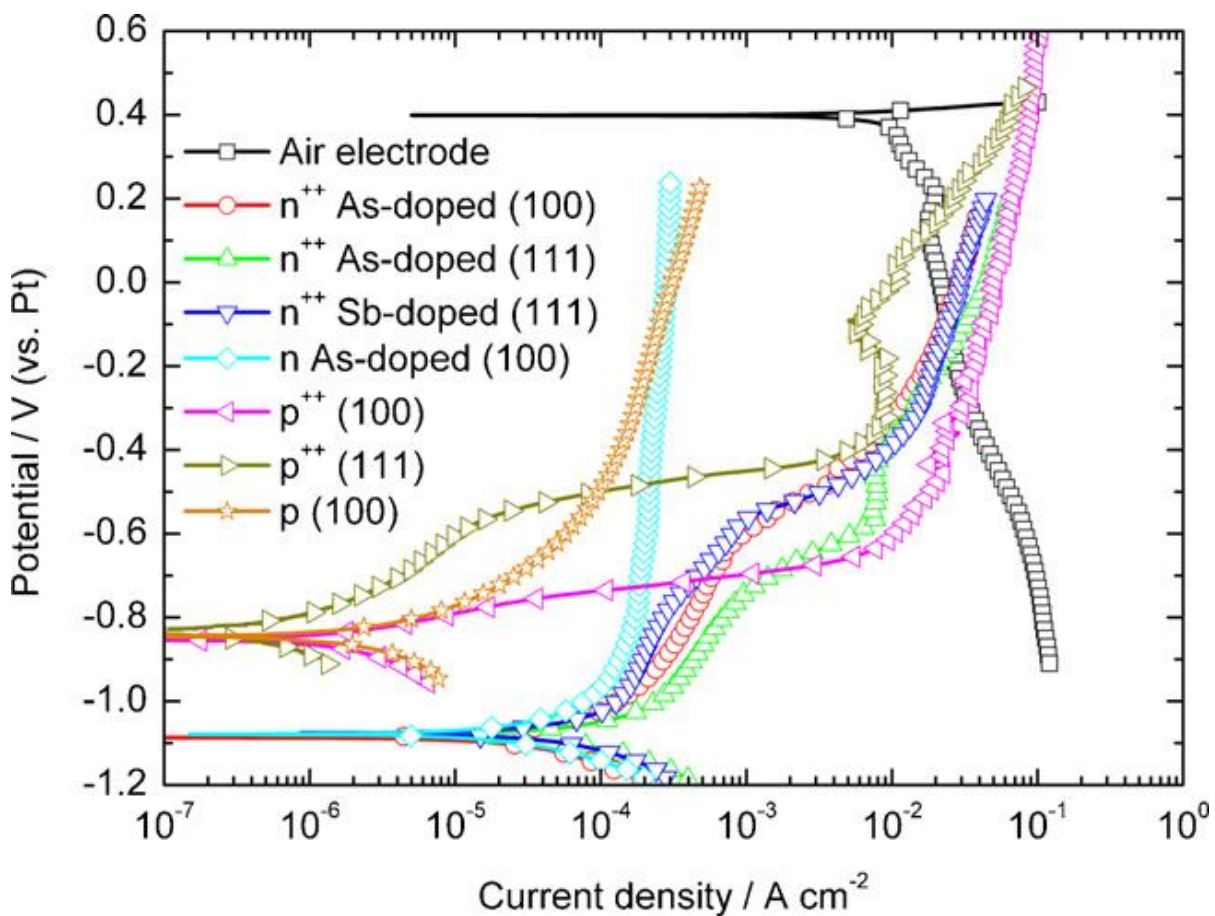


Figure 3-4 Polarization voltammograms recorded at 5 mV s⁻¹ for various electrodes⁴⁸

Table 3-1 Silicon electrodes corrosion rates in $\text{EMI} \cdot (\text{HF})_{2,3}\text{F}^{48}$

Silicon type	Corrosion current / $\mu\text{A cm}^{-2}$	Corrosion rate / nm min^{-1}
n 1 0 0 (As)	8.71	0.16
n ⁺⁺ 1 0 0 (As)	4.23	0.08
n ⁺⁺ 1 1 1 (As)	4.22	0.08
n ⁺⁺ 1 1 1 (Sb)	3.71	0.07
p 1 0 0	1.29	0.02
p ⁺⁺ 1 0 0	0.54	0.01
p ⁺⁺ 1 1 1	0.42	< 0.01

The discharge curves of the Si-air battery for several current densities are given in Figure 3-5. The cell is discharged with current densities of $10 \mu\text{A cm}^{-2}$, $50 \mu\text{A cm}^{-2}$, $100 \mu\text{A cm}^{-2}$ and $300 \mu\text{A cm}^{-2}$. Resulting cell operating voltages are 1.1 V, 1.0 V, 0.9 V and 0.8 V, respectively. Also, the discharge capacities of the cell for each current density are obtained as 3 mAh, 12.5 mAh, 15.25 mAh and 26.7 mAh, respectively. Clearly, the cell operating voltages are decreased by drawing higher current densities. Also, the highest discharge capacity 26.7 mAh is obtained with $300 \mu\text{A cm}^{-2}$ even though drawing smaller current densities result in longer discharge time. High current densities increase the polarization losses in the cell and result in lower operating voltages.

The reason of obtaining higher discharge capacity with higher current density is explained by a model for SiO_2 deposition on porous carbon air electrode in Figure 3-6. However, this explanation in the paper is contradictory to later findings. At low current densities, SiO_2 deposits have fine shape and they are deposited at micro-pores (see Figure 3-6a). When these micro-pores are filled with small crystal particles, it blocks the path for oxygen diffusion and reduction. As a result, the micro-pores become inactive. On the other hand, SiO_2 deposits have coarse and bulky shape at high current densities (see Figure 3-6b). These particles are deposited at meso- and macro-pore sites; therefore micro-pores are still available for further oxygen diffusion and reduction. This phenomenon explains why the battery is more efficient and has more discharge capacity once it is being discharged at high current densities. These discussions

would indicate that the performance of the battery is limited by the air electrode due to pore clogging in the active carbon sites.

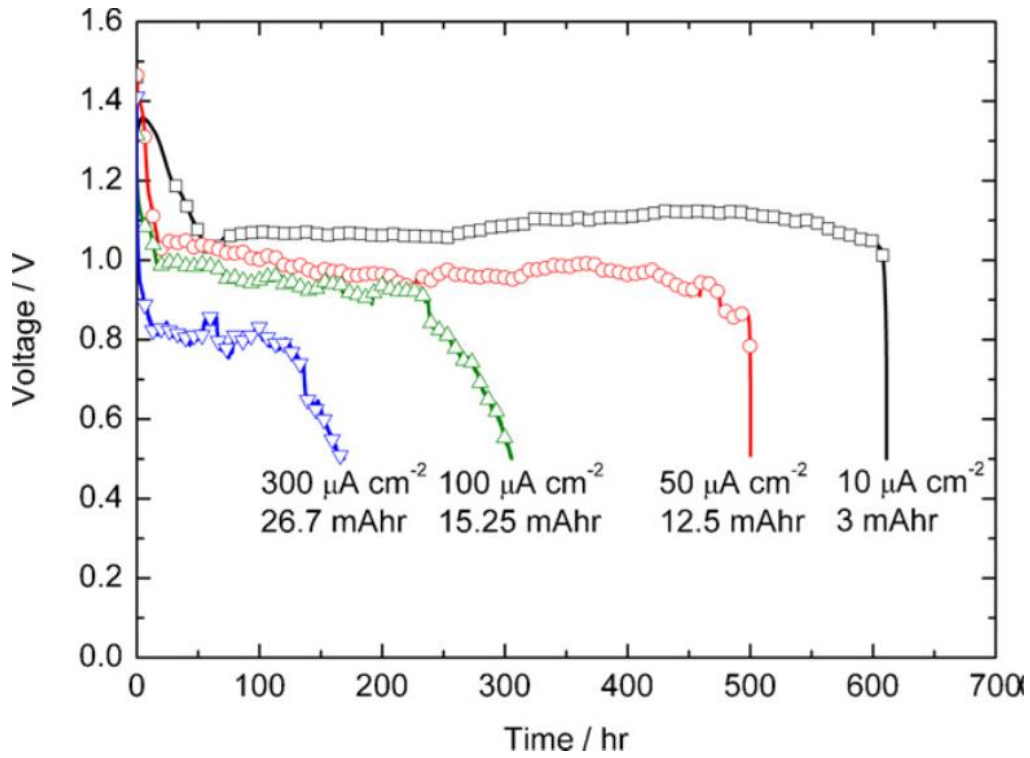


Figure 3-5 Discharge profiles of silicon-air cells at different constant current densities⁴⁸

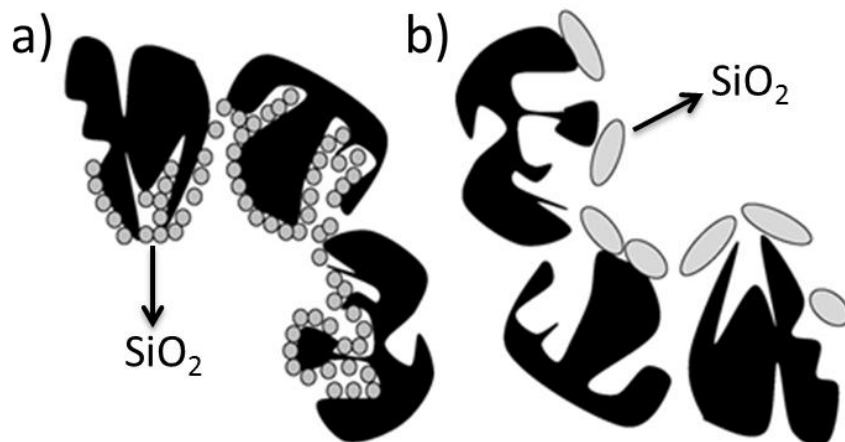
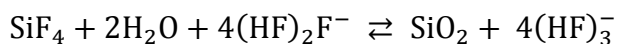


Figure 3-6 A model for SiO_2 deposition on porous carbon electrode. a) Low discharge currents and b) high discharge currents⁴⁸

In another study, the impact of water on the discharge performance of a silicon-air battery has been investigated by Ein-Eli et al.⁴⁹ Because, water plays an important role in the formation reaction of SiO₂ which is given below. Since room temperature ionic liquid has an ability of absorbing water, the addition of water into the electrolyte is possible. By adding water into the electrolyte, the formation of SiO₂ can be shifted to take place in separator or anode.



The discharge profiles of the silicon-air battery with various water contents are shown in Figure 3-7. The battery was discharged with 0.3 mA cm⁻², and the discharge process was terminated at 0.5 V. Discharge capacities of 50 – 70 mAh cm⁻² were obtained at the end of discharge. When the SiO₂ production zone is shifted away from the air cathode, available catalytic sites for oxygen reduction and diffusion are not lost by pore clogging. Therefore, oxygen can still be reduced and diffuse through the pores. Eventually, this leads to an increased capacity. The discharge capacity is increased by 40 % (from 50 mAh cm⁻² to 70 mAh cm⁻²) with addition of 10 – 15 % water into the electrolyte. On the other hand, the discharge potential is lowered by approximately 100 mV with the water addition. This decrease in discharge potential is due to the growth of SiO₂ layer on the silicon surface at anode electrode.

The discharge capacity and the electrolyte conductivity as a function of water content (vol %) in the electrolyte are shown in Figure 3-8. Left axis shows the electrolyte conductivity as a function of water content, while right axis shows the discharge capacity as a function of water content. Clearly, one can see in Figure 3-8 that the amount of water in the electrolyte significantly influences the conductivity and the discharge capacity. The discharge capacity of the battery increases initially by adding water into the electrolyte and reaches a maximum around 15 % water. If more water is added to the system, the discharge capacity decreases dramatically, even below to initial discharge capacity value. The battery could not be operated above 80 % water contents. Furthermore, the effect of water addition on the ionic conductivity shows a similar behavior as the discharge capacity does. The maximum conductivity is obtained with 10 % of water. Further addition of water decreases the conductivity below the maximum value.

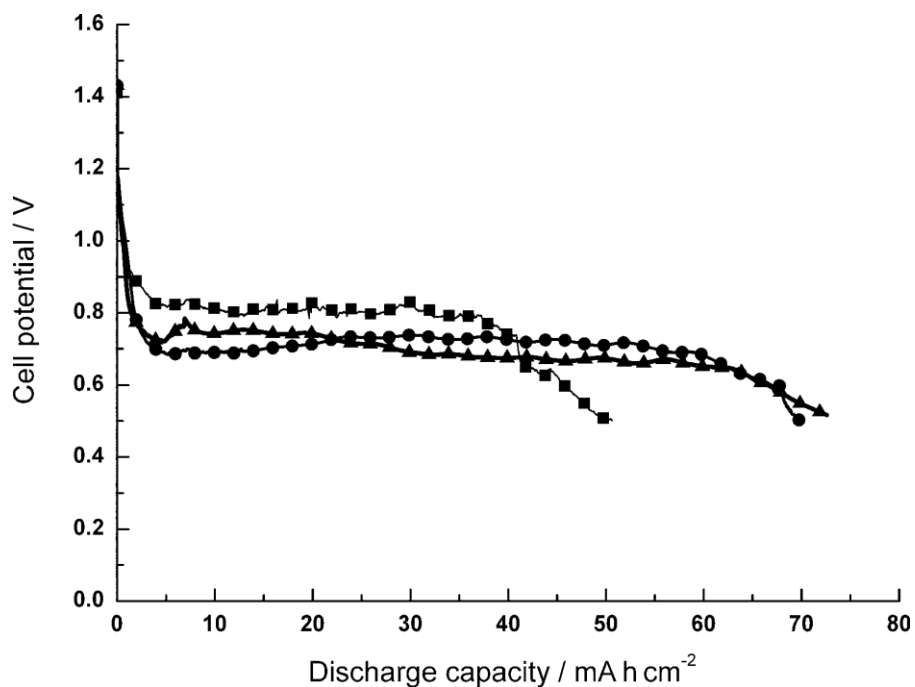


Figure 3-7 Variation of the discharge profiles with increasing water content in the electrolyte:⁴⁹ EMI · (HF)_{2.3}F (■), EMI · (HF)_{2.3}F + 10 vol % H₂O (●), and (HF)_{2.3}F + 15 vol % H₂O (▲) at discharge rate 0.3 mA h cm⁻²

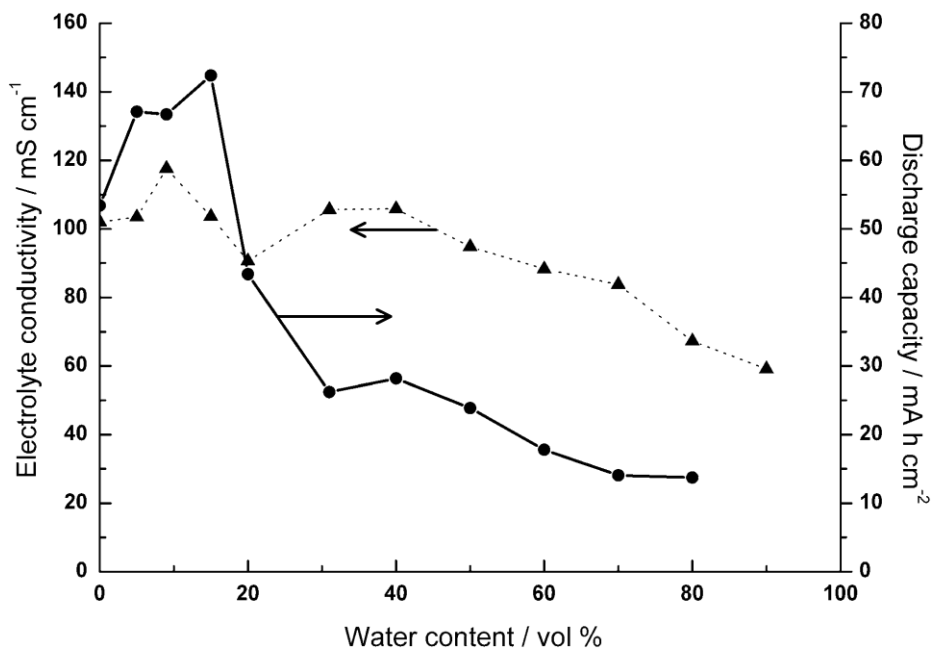


Figure 3-8 Electrolyte conductivity and discharge capacity as a function of water content⁴⁹

The main effect of water addition into the RTIL electrolyte is the reaction zone of formation SiO_2 is shifted into the electrolyte bulk and anode, thus pore clogging of the air electrode by SiO_2 deposits is prevented. This effect increases the discharge capacity of the battery. Once the water content in the electrolyte is too high, it results in a thick, highly resistive oxide layer over the silicon surface at anode. Thus, the electrolyte cannot sustain the electrochemical dissolution of the silicon once high water contents are introduced to the system. That is why the battery cannot be operated above 80 % water contents. Moreover, the addition of water into the electrolyte would reduce the ionic conductivity as lowering the amount of the ionic liquid in the electrolyte. However, the conductivity of RTIL depends on other parameters as well, such as viscosity etc. That is why there is an increase on the ionic conductivity when some amount of water (up to 15 %) is added to the electrolyte.

Overall, these results indicate that operating the Si-air batteries in a humid environment does not degrade the cell performance; in fact it increases the discharge capacities of the batteries. The effect of water addition on the discharge capacity is included in our model (see Chapter 4.7 and Chapter 6). By adding water into the electrolyte; the discharge capacity of the model is increased up to a point, and further addition of water decreased the discharge capacity.

In a most recent study in 2013, the cell impedance during the discharge process is investigated by Ein-Eli et al.⁵² Both electrodes impedances are observed by using electrochemical impedance spectroscopy (EIS) during discharge process. Also, the potential drops of silicon-air cell, cathode and anode are explored. Lastly, the effect of exchanging the anode and cathode during discharge and at the end of discharge is investigated as well.

The cell impedance of a battery can be affected by the generation and development of new interfaces in the battery during discharge. In order to determine which electrode is acting as a dominant source on the cell impedance, the impedance spectroscopies of anode and cathode electrodes are obtained and analyzed as shown in Figure 3-9 at OCP and at a discharge depth of 6.4 mAh. Figure 3-9 shows the Nyquist plots for silicon anode and air cathode. Since the cathode impedance is considerably smaller than the anode impedance, it is zoomed and shown in the right top of Figure 3-9. Therefore, the anode impedance which includes two well-defined

semicircles (separated into high- and low-frequency regions) can be seen clearly in Figure 3-9. The high frequency semicircle is due to a charge transfer resistance and a space charge layer capacitance. On the other hand, the low frequency semicircle is due to the resistance and capacitance of the sub-micron pores that are covered with a thin oxide layer during the anodic reaction.^{48,55}

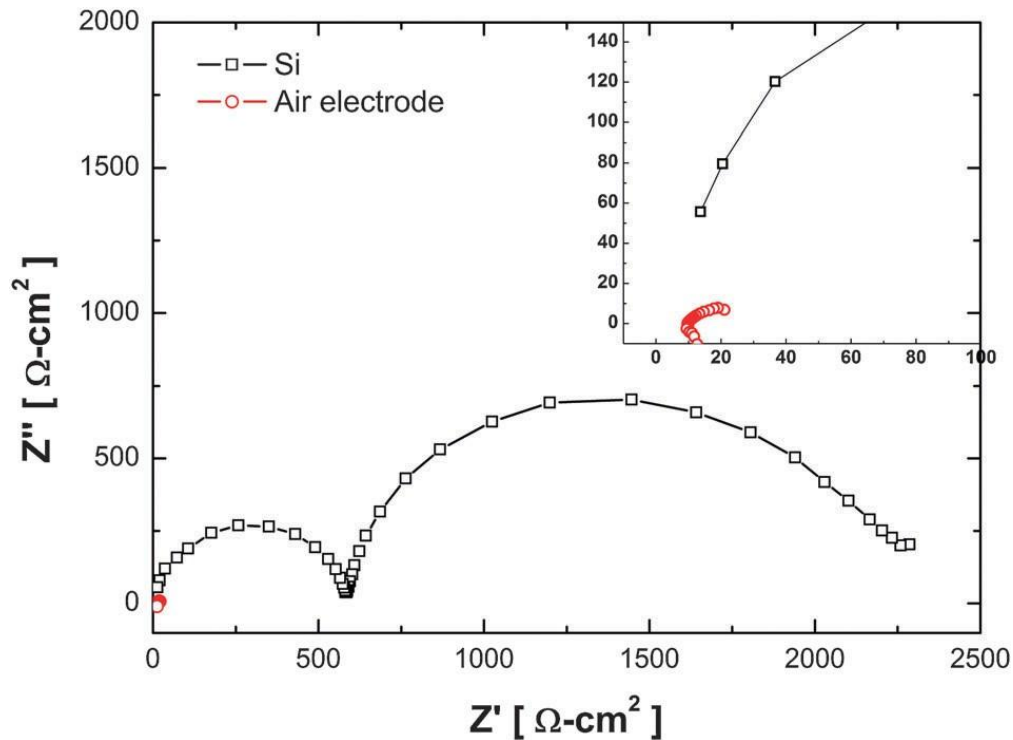


Figure 3-9 Nyquist plots for silicon anode and air cathode half-cells⁵²

The total impedance is given by:

$$Z_{\text{tot}} = \sqrt{|Z'|^2 + |Z''|^2}$$

As the total impedance of air cathode is substantially lower than the anode impedance, it can be neglected for the overall cell impedance. Therefore, the total impedance of the cell is originated from the silicon anode impedance.

The overpotentials of each electrode together with the cell overpotential are shown in Figure 3-10. The behaviors of the overpotentials by discharge capacity are presented in the figure; where the overpotential is defined as:

$$\Delta V(t) = |V(t) - V(t = 0)|$$

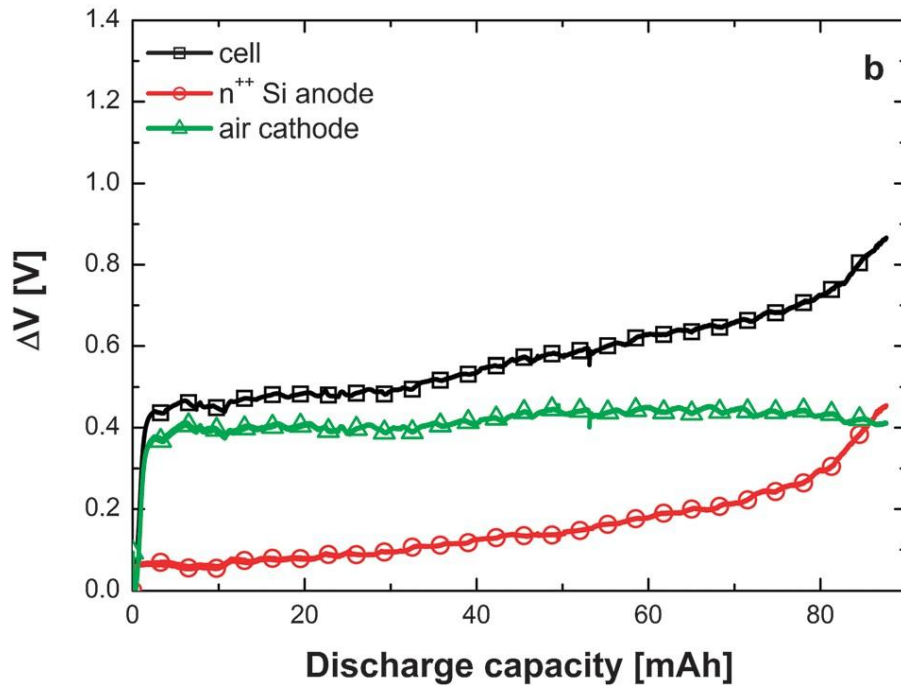


Figure 3-10 Overpotentials on Si-air cell, silicon anode and air cathode at a discharge current of 0.3 mA cm^{-2} .⁵²

Clearly, the initial drop of the air cathode is larger than the silicon anode. The initial drop of air cathode is attributed to dissolved oxygen in the electrolyte. As these oxygen molecules are easy to be accessed, they are consumed in the beginning of the operation. Once more and more oxygen is consumed, the potential of the electrode decreases, i.e. the overpotential of the air cathode increases. After the entire initial drop, the overpotential of the air cathode remains almost constant around 0.4 V. The behavior of the silicon anode overpotential is totally different to the air cathode. There is a small initial drop due to activation polarization, and then the overpotential increases upon continuous discharge. Furthermore, it is clear that the cell overpotential shows the same behavior as the silicon anode.

In the previous studies, it was proposed that the performance of Si-air battery is limited by the cathode electrode. However, the discussions up to now indicate that the battery performance is limited by the anode electrode. EIS results show that the silicon wafer-electrolyte impedance increases during the discharge process and results in battery termination over time. Moreover, the overpotential results confirm that the capacity is limited by the silicon anode rather than the air cathode.

The influence of the silicon anode on the battery discharge performance is also investigated by exchanging the anode electrode at the end of the discharge. The discharge profiles while exchanging the silicon anode are shown in Figure 3-11. The effect of each replacement of the silicon anode on the discharge capacity can be seen in the figure. The first replacement of the anode electrode is done in the middle of discharge, and apparently it does not affect the discharge potential at all. When the silicon anode is replaced at the end of discharge, it results a significant increase on the discharge capacity. Up to the fifth replacement, all the replacements correspond to an increase on the discharge capacity. Nevertheless, the increase in the discharge capacity with the fifth replacement is negligible compared to previous exchanges. The discharge capacity of the silicon-air battery is increased 70 % after the fifth replacement. Therefore, these results indicate that the performance of the Si-air battery is anode limited, but the air cathode and the electrolyte degrade during the discharge as well. This is the reason why the fifth replacement does not give a significant increase on the discharge capacity. The same experiments were conducted for the air cathode and shown in Figure 3-12. The contribution of exchanging the air cathode at the end of discharge on the discharge capacity was not that significant as in the anode case.

Overall, these results indicate and prove that the performance of the Si-air battery is anode limited.

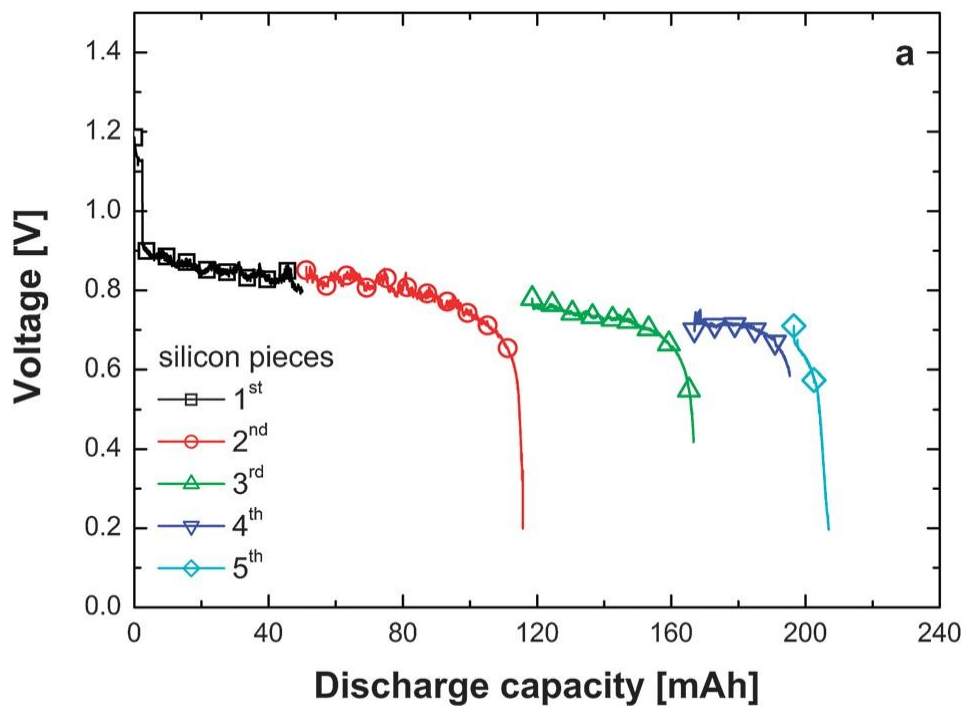


Figure 3-11 Discharge profiles of silicon-air battery at 0.3 mA cm^{-2} , while exchanging the silicon anode⁵²

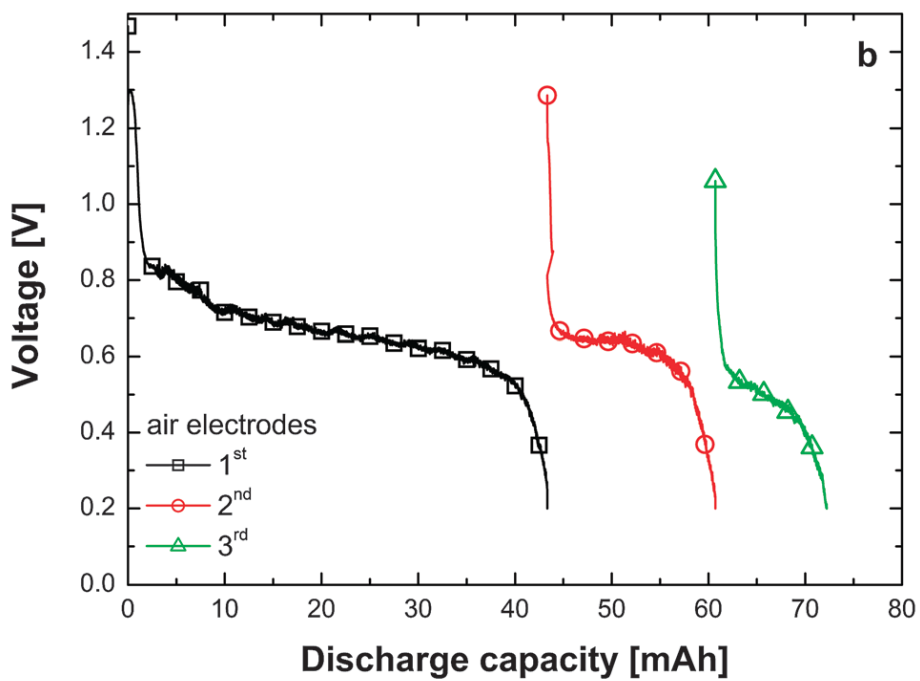


Figure 3-12 Discharge profiles of silicon-air battery at 0.3 mA cm^{-2} , while exchanging the air cathode⁵²

Chapter 4 : MODELING

In this chapter, modeling of a silicon-air battery is discussed. Modeling of a battery helps to understand the battery behavior and to optimize the cell and system design. A battery includes complex interactions between various physical and electrochemical processes that define the battery performance. The battery performance can easily be investigated in a computer environment by modeling all these physical and electrochemical processes individually and properly.

Battery modeling can be done in different levels, i.e. from atomistic levels to macroscopic levels. The atomistic level includes the surface structures, the kinetics of the ORR/OER, the electron conductivity etc.^{15,56-61} while the macroscopic level includes pore blocking, surface passivation etc. in the battery model.^{2,47,56,62-66} The gap between these levels can be bridged by employing mesoscopic continuum models.^{47,62} The developed battery model in this thesis is a continuum model based on atomistic studies and is adapted from the lithium-air battery model.^{2,63,64} In lithium-air battery models, atomistic studies discuss the surface structure of Li_2O_2 crystals,⁵⁶⁻⁶⁰ the kinetics of the ORR/OER in aprotic electrolytes,^{56,57,61} and the electronic conductivity of Li_2O_2 .^{15,57,59}

Here, a dynamic one-dimensional model of a Si-air battery is presented. We model the processes along one direction, which is the y-coordinate. In this thesis, we describe the full basic cell that is consisting of two electrodes and a separator. The electrodes and the separator are divided into computational domains as shown in Figure 4-1. Each domain consists of an arbitrary number of bulk phases which are characterized by their volume fraction and density. Furthermore, each bulk phase consists of an arbitrary number of chemical species. These species are characterized by their concentrations. Each domain contains an arbitrary number of phase boundaries or interfaces, on which chemical reactions can take place.

In this thesis, we take into account the following physicochemical processes; 1) Electrochemical reactions (section 4.3), 2) Transport mechanisms (section 4.4), 3) Oxygen dissolution (section

4.5), 4) Phase coexistence in the electrodes or volume conditions (section 4.6), 5) Nucleation and growth (section 4.7).

The model framework includes the main parts of the battery, main processes including with the precipitation of silicon dioxide. Due to the lack of the experimental data on the silicon-air batteries, we aim to make the simplest realistic approach.

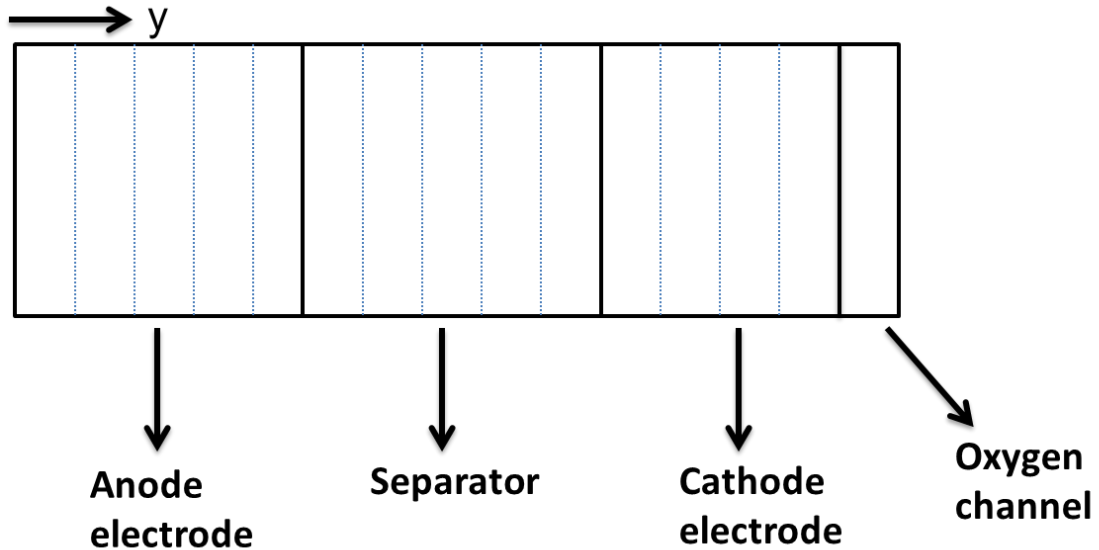


Figure 4-1 Representative modeling domains for the battery

4.1 Simulation Methodology

The battery model in this thesis is inspired from the experimental results. Therefore, the parameters are taken from the experimental studies. No experimental work was performed during this thesis.

The schematic of our silicon-air battery model is given in Figure 4-2. The battery model is comprised of a silicon anode, a separator, and an air cathode. A room temperature ionic liquid is employed as the electrolyte of the battery. Pure gaseous oxygen at atmospheric pressure is used as the cathode reactant.

The silicon electrode in this model has a porous structure in contrast to the experimental studies. In the experiments, a flat silicon anode was used. The discharge process leaves a porous structure behind on the silicon electrode. In this model, we assume that the silicon electrode has a porous structure initially and the pores are filled with RTIL electrolyte as in previous modeling of Li-air batteries.^{2,63,64} The dissolution process of the silicon electrode still takes place during discharge.

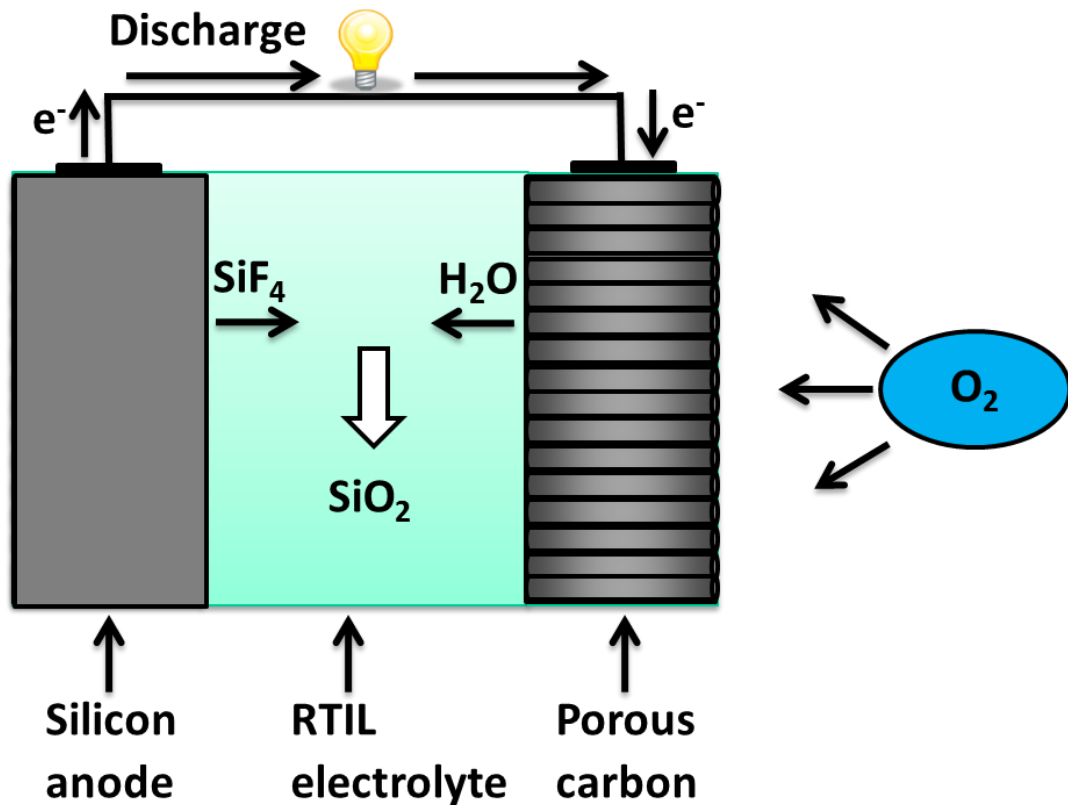


Figure 4-2 A schematic of the silicon-air battery

In this model, we use the same structure for the separator as in the experiments. The separator is a free space between the two electrodes and it is filled totally with the RTIL electrolyte. The separator is assumed to be a reaction-free zone which means the crystallization reaction can only take place on the cathode or on the anode electrode. The reason of this assumption will be explained in Chapter 5.1.

A carbon electrode is used as the cathode and it has a porous structure initially as in the experiments. The pores are already filled with the RTIL electrolyte. We assign the first compartment of the cathode as the oxygen channel, because this compartment is at the exterior surface. The oxygen enters the electrolyte from the oxygen channel and it dissolves immediately. Then, the dissolved oxygen diffuses through the pores of the electrode.

During the discharge process, dissolved oxygen molecules react with the electrolyte and produce water as a reaction product together with the fluoroacidic anion $(\text{HF})_2\text{F}^-$ at the active surfaces of air cathode. On the anode side, silicon metal oxidation forms silicon tetrafluoride SiF_4 together with four electrons and fluoroacidic anion $(\text{HF})_3\text{F}^-$. RTIL anions participate and play an important role in both reactions. Diffusion and migration of the species together with convection of the electrolyte take place in this system. Silicon dioxide particles start to nucleate and grow when the silicon tetrafluoride concentration increases sufficiently beyond its solubility limit. We model these processes such that the model is thermodynamically consistent and the stationary states are represented correctly.

4.2 Numerical Details

The modeling framework in this thesis is implemented into the multi-phase electrochemical simulation tool DENIS.^{2,64} The computational domain is divided into 25 compartments with widths between 28 μm and 57 μm in the cathode, 5 compartments with width of 200 μm in the anode, and 10 compartments with width of 100 μm in the separator. A finite volume scheme is used to discretize the computational domain. In order to evaluate the rate equations and other chemical terms, we use a software called CANTERA.⁶⁷ CANTERA is an open source software which is used for solving the complex chemical reaction systems. CANTERA is connected and embedded into DENIS, so that it will be available during DENIS runtime. The discretized equation system is numerically time-integrated with LIMEX.⁶⁸

4.3 Electrochemical Reactions

The kinetics of the electrode reactions is given by the reaction rate. Reaction rate is defined as the change in the concentration of reactants or products per unit time. Basically, the rate of the reaction is the speed of the reaction and it is defined as how fast or slow a reaction can take place.

Now, we describe the two half-cell reactions in silicon-air batteries. At the anode surface, silicon oxidation takes place:



The reaction rate of this electrochemical reaction is similar to general chemical reactions⁶⁹

$$r = k_f c_{\text{ox}} - k_b c_{\text{red}} . \quad (4.2)$$

In this expression, r is the reaction rate; k_f and k_b are the forward and backward reaction constants; c_{ox} and c_{red} are the concentrations of the reactants and the products, respectively.

In the chemical reactions, the current can be calculated from the electron transfer rate of the reaction as⁶⁹

$$\frac{i}{zFA} = r, \quad (4.3)$$

where i is the current, F is the Faraday constant, z is the charge number, and A is the electrode surface area. The net current can be written as

$$i = k_f z F A c_{\text{ox}} - k_b z F A c_{\text{red}} \quad (4.4)$$

$$i = i_f - i_b,$$

where $i_f = k_f z F A c_{\text{ox}}$ and $i_b = k_b z F A c_{\text{red}}$ are the forward and backward currents.

The rate of a chemical reaction can easily be modified by changing the electric potential step between electrode and electrolyte ($\Delta\phi = \phi_j - \phi_{\text{elyte}}$). The potential dependence of the reaction rates is:

$$k_f = k_f^0 \exp\left(-\frac{\alpha z F \Delta \phi}{RT}\right) \quad (4.5)$$

$$k_b = k_b^0 \exp\left(\frac{(1-\alpha) z F \Delta \phi}{RT}\right). \quad (4.6)$$

Here, k_f^0 and k_b^0 are the rate constants at $\Delta \phi = 0$. α is called transfer coefficient. The transfer coefficient describes the symmetry of the reaction. It can have any value between 0 and 1.

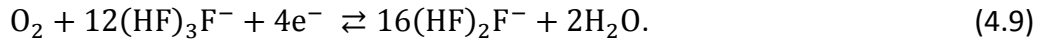
The potential dependence of the reaction rate can be obtained by substituting equations 4.5 and 4.6 into equation 4.2

$$r = k_f^0 c_{\text{ox}} \exp\left(-\frac{\alpha z F \Delta \phi}{RT}\right) - k_b^0 c_{\text{red}} \exp\left(\frac{(1-\alpha) z F \Delta \phi}{RT}\right). \quad (4.7)$$

For the silicon anode, equation 4.2 can be written as⁶³

$$r_{\text{an}} = k_{\text{an}}^f c_{(\text{HF})_2\text{F}^-}^{12} \exp\left(-\frac{\alpha z F \Delta \phi_{\text{an}}}{RT}\right) - k_{\text{an}}^b c_{\text{SiF}_4} c_{(\text{HF})_3\text{F}^-}^8 \exp\left(\frac{(1-\alpha) z F \Delta \phi_{\text{an}}}{RT}\right). \quad (4.8)$$

At the cathode surface, oxygen reduction takes place:



The reaction rate of the oxygen reduction can be written as⁶³

$$r_{\text{ca}} = k_{\text{ca}}^f c_{\text{O}_2} c_{(\text{HF})_3\text{F}^-}^{12} \exp\left(-\frac{\alpha F z \Delta \phi_{\text{ca}}}{RT}\right) - k_{\text{ca}}^b c_{\text{H}_2\text{O}}^2 c_{(\text{HF})_2\text{F}^-}^{16} \exp\left(\frac{(1-\alpha) F z \Delta \phi_{\text{ca}}}{RT}\right). \quad (4.10)$$

Under the equilibrium conditions, the net rate must be zero ($r = 0$). Thus, the reverse reaction rates can be calculated from the forward reaction rates⁶³

$$k_{\text{an}}^b = k_{\text{an}}^f c_{(\text{HF})_2\text{F}^-}^{12} c_{\text{SiF}_4}^{-1} c_{(\text{HF})_3\text{F}^-}^{-8} \exp\left(\frac{\Delta G_{\text{an}}}{RT}\right) \quad (4.11)$$

$$k_{\text{ca}}^b = k_{\text{ca}}^f c_{\text{O}_2} c_{(\text{HF})_3\text{F}^-}^{12} c_{\text{H}_2\text{O}}^{-2} c_{(\text{HF})_2\text{F}^-}^{-16} \exp\left(\frac{\Delta G_{\text{ca}}}{RT}\right), \quad (4.12)$$

where ΔG is the molar Gibbs reaction enthalpy. Also, there is no net current flow at the equilibrium

$$i_f = i_b = i_o, \quad (4.13)$$

where i_o is the exchange current. From the equation 4.4, 4.5 and 4.13, it can be obtained

$$c_{\text{ox}}k_f^{\circ} \exp\left(-\frac{\alpha zF\Delta\phi_{\text{eq}}}{RT}\right) = c_{\text{red}}k_b^{\circ} \exp\left(\frac{(1-\alpha)zF\Delta\phi_{\text{eq}}}{RT}\right), \quad (4.14)$$

where $\Delta\phi_{\text{eq}}$ is the equilibrium potential step. By rearranging equation 4.14,

$$\Delta\phi_{\text{eq}} = \frac{RT}{zF} \ln\left(\frac{k_f^{\circ}}{k_b^{\circ}}\right) + \frac{RT}{zF} \ln\left(\frac{c_{\text{ox}}}{c_{\text{red}}}\right). \quad (4.15)$$

From this expression, the formal standard potential ϕ° can be established

$$\phi^{\circ} = \frac{RT}{zF} \ln\left(\frac{k_f^{\circ}}{k_b^{\circ}}\right). \quad (4.16)$$

By substituting equation 4.16 into 4.15, the thermodynamic consistency of our set of equations with the Nernst equation can be shown⁶⁹

$$\Delta\phi_{\text{eq}} = \phi^{\circ} + \frac{RT}{zF} \ln\left(\frac{c_{\text{ox}}}{c_{\text{red}}}\right). \quad (4.17)$$

At equilibrium conditions, the exchange current can be obtained from the equations 4.4 and 4.5,

$$i_o = i_f = zFAk_f^{\circ} c_{\text{ox}}^{\circ} \exp\left(-\frac{\alpha zF\Delta\phi_{\text{eq}}}{RT}\right) = zFAk_f^{\circ} c_{\text{ox}}^{1-\alpha} c_{\text{red}}^{\alpha} \exp\left(-\frac{\alpha zF\Delta\phi_{\text{eq}}}{RT}\right). \quad (4.18)$$

The exchange current is defined as the rate of electron exchange between the oxidized and reduced species at the equilibrium potential. There is an exchange of electrons in both directions, but the rates in both directions are equal and opposite and thus the net exchange is zero.

In order to derive the kinetics in its most used form^{65,70}, the net current flow can be reformulated by using the equations 4.3 and 4.7

$$i = zFAk_f^{\circ} c_{\text{ox}} \exp\left(-\frac{\alpha zF\Delta\phi}{RT}\right) - Fk_b^{\circ} c_{\text{red}} \exp\left(\frac{(1-\alpha)zF\Delta\phi}{RT}\right). \quad (4.19)$$

Then, using the equations 4.16 and 4.17

$$i = zFA(k_f^{\circ})^{1-\alpha} (k_b^{\circ})^{\alpha} c_{\text{ox}}^{1-\alpha} c_{\text{red}}^{\alpha} \left(\exp\left(-\frac{\alpha zF\eta}{RT}\right) - \exp\left(\frac{(1-\alpha)zF\eta}{RT}\right) \right), \quad (4.20)$$

where $\eta = \Delta\phi - \Delta\phi_{\text{eq}}$ is defined as the overpotential. By rearranging the equation 4.20, general form of the Butler-Volmer equation can be obtained as^{65,69,70}

$$i = i_o \left[\exp\left(-\frac{\alpha z F \eta}{RT}\right) - \exp\left(\frac{(1-\alpha) z F \eta}{RT}\right) \right], \quad (4.21)$$

where $i_o = zFA(k_f^0)^{1-\alpha}(k_b^0)^\alpha c_{\text{ox}}^{1-\alpha} c_{\text{red}}^\alpha$.

For low overpotentials; $i \ll i_o$ and the Butler-Volmer equation can be reformulated as a linear response. In linear response, current is linear in overpotential

$$i = i_o \frac{zFA\eta}{RT}. \quad (4.22)$$

On the other hand, for large overpotentials; $i \gg i_o$ and the Butler-Volmer equation can be simplified to the Tafel equation

$$\eta = a + b \ln \frac{i}{i_o}, \quad (4.23)$$

where a and b are the Tafel constants. The Tafel plot has the slope b

$$\text{Tafel slope: } \frac{\alpha z F}{RT} \text{ for anode} \quad (4.24)$$

$$\text{Tafel slope: } \frac{(1-\alpha) z F}{RT} \text{ for cathode.} \quad (4.25)$$

Thus, we showed that the rate equation and the Butler-Volmer equation are equivalent. The calculation of the reaction rates will be explained in Chapter 5.

4.4 Transport Mechanisms

In this section, transport mechanisms that are used in this model are discussed. Mass transfer can be defined as the movement of species from one point to another point. It can occur whenever there is a difference in electrical or chemical potential at the two points or from a movement of a volume element of solution.

In this model, there are two types of transport mechanisms: diffusion and migration of the species, and convection of the electrolyte. Diffusion and migration arise due to concentration gradient and electrical potential gradient, while convection occurs to enforce volume constraint.

Transport mechanisms are governed by the Nernst-Planck equation where the concentrations of the species follow the continuity equations^{63,64}

$$\frac{\partial(\varepsilon_{\text{elyte}}c_i)}{\partial t} = -\text{div}\vec{j}_i^{\text{D}} - \text{div}\vec{j}_i^{\text{M}} - \text{div}(c_i\vec{v}_{\text{elyte}}) + A^{\text{spez}}\dot{r}_i. \quad (4.26)$$

In equation 4.26, \vec{j}_i^{D} and \vec{j}_i^{M} are the ionic currents due to diffusion and migration, respectively. The third term is the convective transport of the electrolyte. The last term is the total production rate of the chemical reactions. Here $\varepsilon_{\text{elyte}}$ is the volume fraction and \vec{v}_{elyte} is the velocity of the convective flow.

\vec{j}_i^{D} and \vec{j}_i^{M} are determined by^{63,64}

$$\vec{j}_i^{\text{D}} = -\varepsilon_{\text{elyte}}^{\beta} D_i \text{grad } c_i, \quad (4.27)$$

$$\vec{j}_i^{\text{M}} = -\varepsilon_{\text{elyte}}^{\beta} D_i^{\text{M}} \text{grad } \phi_{\text{elyte}}, \quad (4.28)$$

where β is the Bruggeman coefficient and takes into account the porosity and tortuosity of the medium. ϕ_{elyte} is the gradient of the electric potential in the electrolyte and can be determined by charge conservation (assuming electro-neutrality)

$$0 = \sum_i z_i F \frac{\partial(\varepsilon_{\text{elyte}}c_i)}{\partial t}, \quad (4.29)$$

$$0 = \sum_i z_i F (-\text{div}\vec{j}_i^{\text{D}} - \text{div}\vec{j}_i^{\text{M}} - \text{div}(c_i\vec{v}_{\text{elyte}}) + A^{\text{spez}}\dot{r}_i). \quad (4.30)$$

According to Einstein relation, the migration coefficient D_i^{M} is a function of the diffusion coefficient D_i in dilute solutions^{63,64}

$$D_i^{\text{M}} = \frac{z_i F}{RT} c_i D_i. \quad (4.31)$$

Also, D_i^{M} can be written from Ohm's law as

$$D_i^M = \frac{1}{z_i F} \kappa, \quad (4.32)$$

where κ is the conductivity and is taken from the literature.⁴⁹

From the equations 4.31 and 4.32, diffusion coefficient D_i can be calculated as

$$D_i = \frac{\kappa}{c} \frac{1}{(z_i F)^2} RT. \quad (4.33)$$

Convection contributes to electrolyte transport. This is important in the simulation since the stoichiometric numbers of the electrolyte species are quite big, and a tiny change in their concentrations affects the system significantly. The convective velocity of the electrolyte is determined by enforcing volume constraint in the electrode pores with v_{elyte} . This phenomenon will be discussed in section 4.6.

4.5 Oxygen Dissolution

During discharge process of the battery, pure gaseous oxygen enters the battery at the oxygen inlet. In order to react in the oxygen reduction reaction, it needs to be dissolved in the electrolyte. To be able to maintain the oxygen dissolution, it needs to be modeled most appropriately.

The equilibrium of oxygen dissolution is described by Henry's Law.⁶³ It states that the solubility of gaseous species is proportional to its partial pressure

$$c_{O_2}^S = H p_{O_2}, \quad (4.34)$$

where $c_{O_2}^S$ is the solubility, p_{O_2} is the partial pressure, and H is Henry's constant. However, Henry's law does not include the kinetics of the dissolution process. Hence, the dissolution process is being treated as a chemical reaction in this model⁶⁴ as



The kinetics of this reaction can be calculated with the rate equation⁶³

$$\dot{r}_s = k_s^f p_{O_2} - k_s^r c_{O_2}. \quad (4.36)$$

However, the oxygen dissolution reaction is so fast that it is always in equilibrium in our simulation.⁶²

4.6 Phase Coexistence in the Electrodes (Volume Conditions)

Due to the phase formation or dissolution reactions, such as crystallization of solid SiO_2 particles, the total volume of the electrode pores can change. Consequently, this process affects the volume of the phases in the pores. In the case of solid structure growth in the electrode pores, there can be two ways to handle the effect of volume changing:

1. Another phase or phases (liquid or gaseous phases) needs to be assigned as a compressible phase.⁶⁴
2. In the case of incompressible phases, convection of the electrolyte can be introduced.

In our model, convection of the electrolyte is introduced because RTIL is incompressible, which means the density of the electrolyte is constant in time and space.⁶⁹ This assumption is satisfied by the flow of the electrolyte through the electrode pores. Basically, the increased volume fraction of the solid particles inside the electrodes causes a decrease in the volume fraction of the electrolyte. This volume constraint enforces convective flow of the electrolyte. In our model, we define the convective flow with electrolyte velocity v_{elyte} .

We allow such a convective flow into or out of the battery at the oxygen inlet. We find that the volume change of the anode by the dissolution is nearly balanced with the crystal growth. Therefore, the amount of possible leakage will be very small. In the experiments, none of the studies witnessed a leakage in their systems. Even if there was a leakage in the experiments, the casing of the battery would hold it since the amount of leakage should be small.

The phase coexistence of all phases is modeled by applying the constraint^{63,64}

$$\sum_s \varepsilon_s = 1, \quad (4.37)$$

where ε_s is the volume fraction of a phase s . This expression is satisfied by the total volume at each position y . It states that the sum of the volume fractions ε_s of the all phases must be 1.

The equation of state for the electrolyte is⁶³

$$\sum_i \bar{V}_i c_i = 1, \quad (4.38)$$

where \bar{V}_i and c_i are the partial molar volume and the concentration of the species i , respectively. This expression is valid for any phase in the system and it follows from basic thermodynamics.

Moreover, the total volume of the solid particles can be affected by phase formations or dissolutions, like growth of solid structures.^{63,64} The growth of new phases is described with a continuity equation:^{63,64}

$$\frac{\partial \varepsilon_s}{\partial t} = r_s A_s^{\text{spez}} V_s^M, \quad (4.39)$$

where V_s^M is the molar volume, r_s is the reaction rate, and A_s^{spez} is the specific surface area of the phase s .

The dynamic change of electrolyte species and solid phases are modeled with the equations 4.37, 4.38, and 4.39. By employing these relations, the volume conditions are ensured successfully in the system.

4.7 Nucleation and Growth

As mentioned earlier in this thesis, there is a crystallization process in the silicon–air battery. The crystallization reaction is given as



Crystallization process starts with nucleation. In this process, solubility of silicon tetrafluoride SiF_4 plays an important role. When the SiF_4 concentration exceeds its solubility limit, small stable clusters start to nucleate followed by growth. Mainly, the crystallization process consists

of two stages. The first stage involves the formation of a supersaturated solution which is followed by the nucleation. At the supersaturation point, the solvent cannot dissolve any more molecules. Therefore, molecules which are dissolved in the solution begin to aggregate and eventually form nuclei. This process is defined as the nucleation and it acts as the center of crystallization. The second stage is called growth stage. Once the nucleus reaches the critical nucleus size, it becomes a stable nucleus. And then, the growth process begins immediately. Nucleation process can continue during the growth process if the supersaturation remains to be large.

In this thesis, classical nucleation and theory (CNG)^{63,71,72} is taken as a reference to model crystallization process. The CNG involves a thermodynamic parameter called free energy G (or Gibbs free energy). The free energy change ΔG required for the formation of a single crystal nucleus is the sum of the volume free energy (or the free energy change for the phase transformation in the infinite system), ΔG_V and the cluster's total surface energy (or the free energy change for the formation of a surface), ΔG_A .

$$\Delta G = \Delta G_V + \Delta G_A = -\Delta gV + \gamma A. \quad (4.41)$$

Here, V and A are the volume and the area of disc-shaped nucleus, and γ is the surface energy. Δg is the driving force for nucleation⁷³

$$\Delta g = -\frac{\Delta\mu}{V^M}, \quad (4.42)$$

where $\Delta\mu$ is the change in the chemical potential of crystallizing species and V^M is the molar volume.

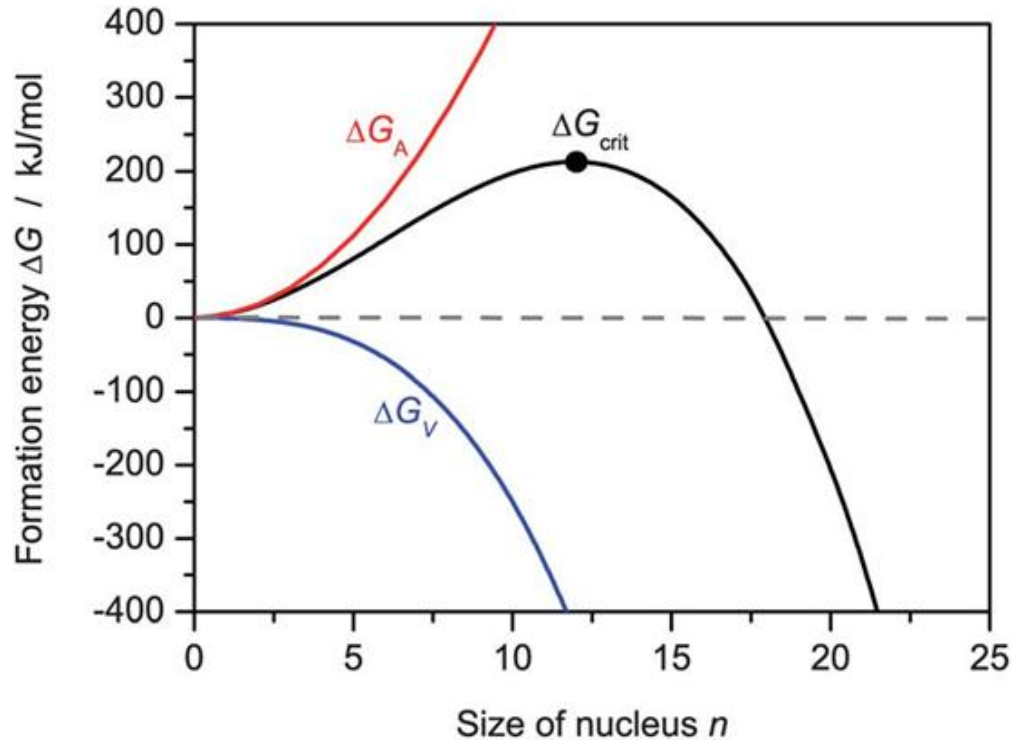


Figure 4-3 Formation energy of a crystal nucleus⁶³

The free energy change required for cluster formation is shown in Figure 4-3. Clearly, the value of ΔG_V is negative since the solid state is more stable than the liquid state. On the other hand, the value of the surface term is positive and increases the free energy. The total free energy change is equal to the sum of these two energies. At small size of nucleus n , the positive term dominates and increases the total free energy change. However, when the cluster size increases, the total free energy first passes a maximum at a critical nucleus size n_{crit} and then decreases continuously. In order to grow stably, crystal clusters must exceed this critical nucleus size. This critical nucleus size is determined by $\frac{d\Delta G}{dn} = 0$. Then the critical formation energy of heterogeneous disc-shaped nucleation⁷¹ is determined as

$$\Delta G_{crit} = -\frac{\pi h V^M \gamma^2}{\Delta \mu}. \quad (4.43)$$

The nucleation rate of critical nuclei is calculated with⁶³

$$\dot{N} = D_0 a_D^{-2} Z N_0 \exp\left(-\frac{\Delta G_{\text{crit}}}{kT}\right), \quad (4.44)$$

where $D_0 a_D^{-2}$ is the activation frequency for diffusion and corresponds to a diffusion-limited process. Z is the Zeldovich factor ($Z = (\Delta G_{\text{crit}}/3\pi kT)^{0.5}/n_{\text{crit}}$) and it describes that a critical nucleus can disintegrate again. N_0 is the number of sites where nucleation can take place. The last term expresses the activation of a critical complex from thermal fluctuations.

Up to here, the kinetics of nucleation process is discussed. As mentioned earlier, the nucleation process is followed by the growth process. In this model, a linear growth process is assumed. The reaction rate for a linear growth process is⁶³

$$r_{\text{cryst}} = \frac{D_0}{\delta} (c_{\text{SiF}_4} - c_{\text{SiF}_4}^{\text{S}}), \quad (4.45)$$

where $c_{\text{SiF}_4}^{\text{S}}$ is the solubility limit of silicon tetrafluoride and δ is the diffusion layer thickness. Furthermore, disc-shaped heterogeneous nucleation is assumed to take place only on the crystal particles. Because, in order to model heterogeneous nucleation all over the battery, contact angles (wetting angles) between materials and crystals are required. Since there are many different materials and surface morphologies in the battery, it is not an easy task to measure these angles.

The nucleation area is determined by⁶³

$$\frac{\partial A_{\text{cryst}}^{\text{spez}}}{\partial t} = \pi r_{\text{crit}}^2 \dot{N}(N_0), \quad (4.46)$$

$$N_0 = \frac{(A_{\text{cryst}}^{\text{spez},0} - A_{\text{cryst}}^{\text{spez}})}{a^2}, \quad (4.47)$$

where $A_{\text{cryst}}^{\text{spez},0}$ is the specific surface area of the pristine cathode/separator surfaces. The crystal particles start to grow on top of these discs according to equation 4.45. Here, a constant diffusion layer thickness $\delta = \delta_0$ is assumed which is determined by the pore structure.

Chapter 5 : PARAMETERIZATION

In this chapter, parameters for the simulation of silicon-air batteries are presented. The parameters are mostly taken from the experimental studies. Since some of the parameters (i.e. solubility of SiF_4 , solubility of O_2 , diffusivities etc.) cannot be found in the literature, we make assumptions for these parameters that are justified below. The battery model is assumed to be an isolated environment at a temperature of $T = 298.15 \text{ K}$. Furthermore, oxygen pressure of $p_{\text{O}_2} = 1.0132 \cdot 10^5 \text{ Pa}$ is assumed for this simulation. All parameters are presented in Table 5-1.

This chapter is divided into three parts:

1. Structure of the battery,
2. Thermodynamics,
3. Transport and kinetics.

First, we discuss about the structure of the battery in terms of dimensions and computational domains. Second, Gibbs free energies of the species, molar volumes, solubility's of SiF_4 and O_2 , and surface energy are given in section 5.2. Last, we discuss diffusivities and reaction kinetics in section 5.3.

5.1 Structure of the battery

In the experiments, cylindrical silicon-air cells with a diameter of 0.8 cm and a surface area of 0.5 cm^2 were constructed.^{9,48} In this thesis, the geometric structure of the silicon-air battery is explained briefly in Chapter 4. The computational domain is divided into four parts (shown in Figure 4-1):

1. Oxygen channel
2. Porous carbon cathode
3. Separator
4. Porous silicon anode

Gaseous oxygen enters the cell at the oxygen channel. The oxygen channel is the first compartment of the cathode (see section 4.1). Here, oxygen dissolution is the only reaction which can take place. The porous carbon has a length of 1 mm and it is divided into 25 domains. Both oxygen reduction reaction and crystallization reaction take place in each domain. The separator part is defined as a reaction-free zone; it is filled with RTIL electrolyte and there is no reaction taking place in the separator. Because, there are no surfaces for heterogeneous crystallization and homogeneous crystallization is very slow. The separator has a length of 1 mm and it is divided into 10 computational domains in order to observe the concentration, volume fraction etc. gradients during the cell operation. Moreover, the porous silicon anode, which has a length of 1 mm, is divided into 5 computational domains and both silicon oxidation reaction and crystallization reaction can take place in each domain. All these structural parameters are shown in Table 5-1.

In the simulation results, capacities are shown with respect to the mass of silicon. The initial mass of silicon with respect to the cell area is 1.86 kg m^{-2} .

5.2 Thermodynamics

In order to define thermodynamics of the system, we use Gibbs free energies. Because the battery model is assumed to be an isolated environment, entropy values are not taken into account. Firstly, we assume that the standard Gibbs free energies of silicon metal and oxygen are zero ($G_{\text{Si}}^0 = 0, G_{\text{O}_2}^0 = 0$), because all elements have zero standard Gibbs free energy in their standard states. Secondly, the OCV of half-cells are taken from the literature (see Figure 3-4). Thirdly, we assume that water has 0.1 % volume content initially, and thus, molar concentration of H_2O is $0.0553 \text{ mol L}^{-1}$. Also, the solubility of SiF_4 is chosen as $c_{\text{SiF}_4}^{\text{S}} = 1.0 \text{ mol L}^{-1}$. This is important for the crystallization point and we discuss it below. Lastly, after calculating the Gibbs free energies of pure H_2O and SiF_4 , the Gibbs free energies of $(\text{HF})_2\text{F}^-$ and $(\text{HF})_3\text{F}^-$ are calculated by using the Gibbs energy formula ($\Delta G = -zFE$) and the Nernst equation

$(\Delta G_i = \Delta G_i^\circ + RT \ln \frac{c_i}{1 \text{ mol L}^{-1}})$ for each half-cell. Enthalpy, standard Gibbs energy, and entropy values are obtained from the Atkin's Physical Chemistry⁷⁴ and from other literature.⁷⁵

The solubility of oxygen in RTIL is unknown, hence we take its solubility in pure water which is provided by Tromans⁷⁶. Furthermore, the solubility of gaseous SiF₄ in RTIL is not provided by the experiments. We assume the solubility of SiF₄ as $c_{\text{SiF}_4}^s = 1.0 \text{ mol L}^{-1}$. This value also takes the role of the crystallization limit. Lower values lead to numerical problems in the simulation (i.e. at lower values, crystallization already starts while the simulation equilibrates the system at $t < 0$ s). Then, the initial concentration for SiF₄ is assumed as $c_{\text{SiF}_4} = 0.0001 \text{ mol L}^{-1}$. In order to start the crystallization process, c_{SiF_4} needs to exceed the solubility limit. By setting the initial concentration as a lower value, it takes time to reach its solubility limit and we do not have crystallization at $t < 0$ s.

Moreover, mole fractions of each species in the electrolyte are calculated from the molecular mass and density of each species.^{74,77} We also represent the partial molar volumes of the electrolyte species. The partial molar volumes of the electrolyte ions (EMI, (HF)₂F⁻ and (HF)₃F⁻) are identical. Moreover, we assume that H₂O and SiF₄ have no contribution on the total volume because they have quite low concentrations. The battery has a volume of 100 cm³.

The surface energy of α -quartz is taken from the literature.⁷⁸⁻⁸¹ Various surfaces of α -quartz were investigated with periodic density functional theory (DFT) calculations. Surface energies of α -quartz are found to range from 0.1 to 0.45 J m⁻².⁸¹ Among these surface energies, we consider those of the relaxed surfaces found in the range from 0.1 to 0.25 J m⁻²,⁷⁹ because the relaxed surfaces are most stable. We assume the surface energy as 0.2 J m⁻² in our simulation.

5.3 Transport and Kinetics

Transport of the species and kinetics of the reactions both affect the cell performance significantly. In order to calculate the diffusion coefficients for electrolyte species, dilute

solution theory⁶⁴, Einstein-Stokes relationship, and Ohm's law are employed in the model. Conductivity of the RTIL is obtained from the previous study.⁴⁹ By using the relation of Einstein-Stokes and Ohm's law, diffusion coefficients for the electrolyte species are calculated as $D_i = 2 \cdot 10^{-10} \text{ m}^2 \text{ s}^{-1}$. However, this diffusion coefficient results in a concentration gradient which eventually affects the overpotential of the electrodes. Therefore, the diffusivities of the electrolyte species are assumed to be 1 order of magnitude higher. In this model EMI, $(\text{HF})_2\text{F}^-$ and $(\text{HF})_3\text{F}^-$ have the same diffusivity.

Furthermore, we take the oxygen diffusivity in pure water⁸² since the oxygen diffusivity in RTIL is unknown

$$D_{\text{O}_2} = 1.693 \times 10^{-6} \text{ m}^2 \text{ s}^{-1} \exp\left(\frac{16739 \text{ J mol}^{-1}}{RT}\right). \quad (5.1)$$

As mentioned in Chapter 4.3, the rate of the reaction can be calculated from the current in polarization experiment⁴⁸ (see equation 4.3). In our model, by extracting the data from the polarization voltammograms (Figure 3-4), the reaction rates are calculated through several steps. Figure 5-1 shows the extracted data and the fitting of the calculation results. From Figure 5-1, exchange current densities are calculated for both anode and cathode taking into accounts the specific surface areas and electrode lengths. We get $j_{0,\text{anode}} = 0.0014 \text{ A m}^{-2}$ and $j_{0,\text{cathode}} = 0.1439 \text{ A m}^{-2}$. We also calculate the symmetry coefficients as $\alpha_{\text{anode}} = 0.024275373$ and $(1 - \beta) = \alpha_{\text{cathode}} = 0.0064077925$ from the Tafel slopes of each electrode. Then, by using equation 4.18 the kinetics of the reactions are calculated. The forward reactions rates

$$k_{\text{anode}}^f = 3.34 \cdot 10^{-18} \frac{\text{mol}}{\text{m}^2 \text{ s}} \cdot \left(\frac{\text{L}}{\text{mol}}\right)^{12} = 3.34 \cdot 10^{-54} \frac{\text{m}^{34}}{\text{s mol}^{11}}$$

$$k_{\text{cathode}}^f = 1.69 \cdot 10^{-10} \frac{\text{mol}}{\text{m}^2 \text{ s}} \cdot \left(\frac{\text{L}}{\text{mol}}\right)^{13} = 1.69 \cdot 10^{-49} \frac{\text{m}^{37}}{\text{s mol}^{12}}$$

are determined by

$$k_{\text{anode}}^f c_{(\text{HF})_2\text{F}^-}^{12} = \frac{j_0 e^{\frac{-\alpha z F \Delta \Phi_{\text{ocv}}}{RT}}}{Fn} \quad (5.2)$$

$$k_{\text{cathode}}^f c_{(\text{HF})_3\text{F}^-}^{12} c_{\text{O}_2} = \frac{j_0 e^{\frac{(1-\beta)zF\Delta\Phi_{\text{ocv}}}{RT}} e^{\frac{-zF\Delta\Phi_{\text{ocv}}}{RT}}}{Fz}. \quad (5.3)$$

These reaction rates also depend on the specific surface areas; $A_{ca}^{spez} = 10^6 \text{ m}^{-1}$, $A_{O_2}^{spez} = 6.7 \cdot 10^7 \text{ m}^{-1}$, $A_{an}^{spez} = 10^6 \text{ m}^{-1}$, and $A_{cryst}^{spez,0} = 10^6 \text{ m}^{-1}$.

As it can be seen from Figure 5-1, the calculations are totally consistent with the experimental results. At low overpotentials, which means electrode potentials are close to their OCV conditions ($\phi_{anode} = -1.01 \text{ V}$, $\phi_{cathode} = 0.4 \text{ V}$), both electrodes are in the linear regime. However, at high overpotentials, which means the electrode potentials are different from the OCV conditions, they are in the Tafel regime.

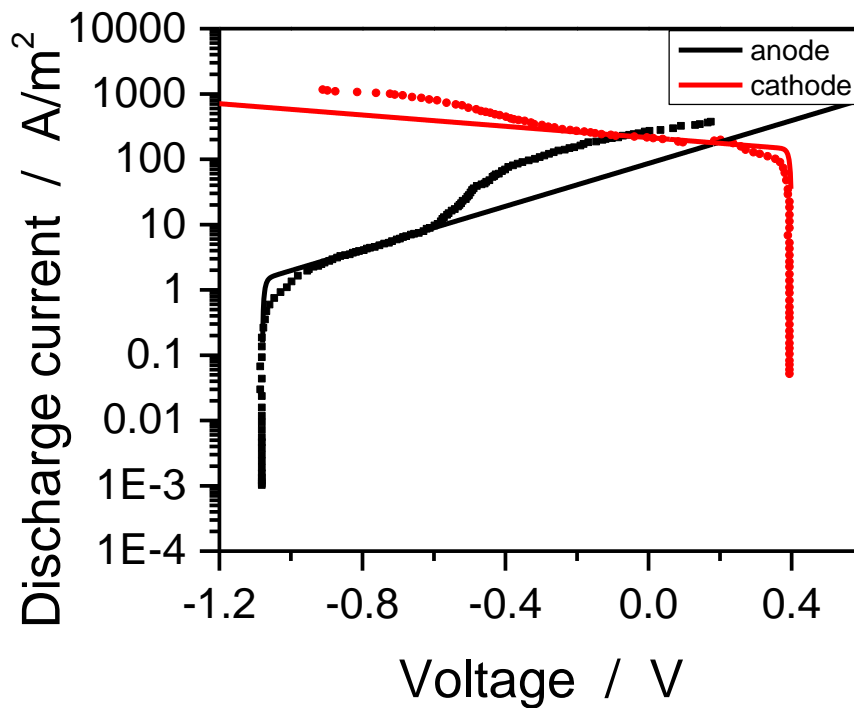


Figure 5-1 Polarization voltammograms and the Butler Volmer equation fitting. Dots are the experimental results, lines are the calculation results.

Table 5-1 Definition of parameters for the silicon-air battery

			Species	Gas state, G=-TS			
Cathode Channel	Control Volumes	1 x 10 μm	O ₂	0			
Cathode	Thickness ^{52,83}	990 μm					
	Control volumes	15 x 28 μm + 10 x 57 μm					
	Bulk phases	Volume fraction	Species	Molar Gibbs energy ^{74,75}	Density / Initial concentration ^{74,76,77}	Diffusion coefficient ⁸²	Partial molar volumes
	Carbon	0.25	C	0	2.26·10 ³ kg·m ⁻³	-	0
	Electrolyte	0.75	EMIM ⁺	0	6.41·10 ³ mol·m ⁻³	2.0·10 ⁻⁹ m ² ·s ⁻¹	7.78·10 ⁻⁵ m ³ ·mol
			(HF) ₂ F ⁻	-1035.52760 kJ·mol ⁻¹	4.48·10 ³ mol·m ⁻³	2.0·10 ⁻⁹ m ² ·s ⁻¹	7.78·10 ⁻⁵ m ³ ·mol
			(HF) ₃ F ⁻	-1405.21479 kJ·mol ⁻¹	1.92·10 ³ mol·m ⁻³	2.0·10 ⁻⁹ m ² ·s ⁻¹	7.78·10 ⁻⁵ m ³ ·mol
			O ₂	16.514 kJ·mol ⁻¹	1.2 mol·m ⁻³	2.0·10 ⁻⁹ m ² ·s ⁻¹	0
			SiF ₄	-1573.594 kJ·mol ⁻¹	1.0·10 ³ mol·m ⁻³	2.0·10 ⁻⁹ m ² ·s ⁻¹	0
			H ₂ O	-237.130 kJ·mol ⁻¹	0.05·10 ³ mol·m ⁻³	2.0·10 ⁻⁹ m ² ·s ⁻¹	0
	Silicon dioxide (SiO ₂)	0	SiO ₂	-636.217203 kJ·mol ⁻¹	2.64·10 ³ kg·m ⁻³	-	0
	Interfaces	Specific Area	Reactions	Forward rate ⁴⁸			
	Carbon-Electrolyte	1·10 ⁶ m ² ·m ⁻³	O ₂ + 12(HF) ₃ F ⁻ + 4e ⁻ ⇌ 16(HF) ₂ F ⁻ + 2H ₂ O	1.69·10 ⁻⁴⁹ m ³⁷ ·s ⁻¹ ·mol ⁻¹²			
	Carbon-SiO ₂ -Electrolyte	1·10 ⁶ m ² ·m ⁻³	SiF ₄ + 2H ₂ O + 4(HF) ₂ F ⁻ ⇌ SiO ₂ + 4(HF) ₃ F ⁻	Nucleation and growth theory			
	Carbon-Gas	-	O ₂ ^g ⇌ O ₂ ^{aq}	Assumed in equilibrium			
Separator	Thickness ^{52,83}	1 mm					
	Control volumes	10 x 100 μm					
	Bulk phases	Volume fraction	Species				
	Electrolyte	1	See cathode				

Anode	Thickness ^{52,83}	1 mm					
	Control volumes	5 x 200 μm					
	Bulk phases	Volume fraction	Species	Molar Gibbs energy	Density / Initial concentration	Diffusion coefficient	Partial Molar volumes
	Silicon	0.8	Si	0	$2.32 \cdot 10^3 \text{ kg} \cdot \text{m}^{-3}$	-	0
	Electrolyte	0.2	See cathode	See cathode	See cathode	See cathode	See cathode
	Silicon dioxide (SiO_2)	0	SiO_2	See cathode	See cathode	-	0
	Interfaces	Specific Area	Reactions	Forward rate ⁴⁸			
	Silicon-Electrolyte	$1 \cdot 10^6 \text{ m}^2 \cdot \text{m}^{-3}$	$\text{Si} + 12(\text{HF})_2\text{F}^- \rightleftharpoons \text{SiF}_4 + 8(\text{HF})_3\text{F}^- + 4\text{e}^-$	$3.34 \cdot 10^{-54} \text{ m}^{34} \cdot \text{s}^{-1} \cdot \text{mol}^{-11}$			
	Silicon- SiO_2 -Electrolyte	$1 \cdot 10^6 \text{ m}^2 \cdot \text{m}^{-3}$	$\text{SiF}_4 + 2\text{H}_2\text{O} + 4(\text{HF})_2\text{F}^- \rightleftharpoons \text{SiO}_2 + 4(\text{HF})_3\text{F}^-$	Nucleation and growth theory			
General	Surface Energy	$0.2 \text{ J} \cdot \text{m}^{-2}$					
	Crystal standard radius	$1 \cdot 10^{-5} \text{ m}$					

Chapter 6 : RESULTS AND DISCUSSION

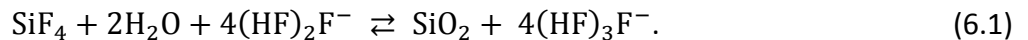
In this chapter, simulation results for the Si-air battery are presented and discussed. We also compare between experiments and our simulation results. The remarkable effect of water addition into electrolyte on the discharge process of Si-air battery is emphasized in the simulations.

6.1 Nucleation and Growth

An important phenomenon for the Si-air battery model is the crystallization process. This process affects the concentrations, volume fractions, overpotentials, diffusivities, and thus the capacity of the battery by forming solid particles SiO_2 in the pores of the electrodes. In the next section, the effect of crystallization on overpotential will be discussed as well.

Crystallization process was also discussed in Chapter 3.1 and Chapter 4.6 in detail. In this section, nucleation criterion will be defined and then the simulation results will be shown, respectively.

A nucleation criterion, which is defined as the thermodynamic onset point for the nucleation and growth, is determined by the thermodynamics of the crystallization reaction



First, the Nernst equation

$$\Delta G_i = \Delta G_i^\circ + RT \ln \frac{c_i}{1 \text{ mol L}^{-1}} \quad (6.2)$$

for each species is written. Second, the Gibbs free energy of the reaction is calculated by

$$\Delta G = \Delta G_{\text{products}} - \Delta G_{\text{reactants}} \quad (6.3)$$

At equilibrium, Gibbs free energy of the reaction is zero $\Delta G = 0$ and consequently, following relation is obtained as

$$\frac{c_{\text{SiF}_4} c_{\text{H}_2\text{O}}^2 c_{\text{HF}_2\text{F}^-}^4}{c_{\text{HF}_3\text{F}^-}^4} = 9.08 \cdot 10^{-2} \text{ mol}^3 \text{ L}^{-3}. \quad (6.4)$$

This value is defined as the nucleation criterion. When the relation exceeds this criterion, nucleation and growth is thermodynamically favored.

The time dependence of the nucleation criterion is shown in Figure 6-1 and Figure 6-2 for various water contents. The difference between the relation result and the nucleation criterion is the driving force for the crystallization process and shown on the figures.

At low water contents up to 1 % H₂O, in Figure 6-1, the concentration relation sharply increases to a peak point, then it decreases until reaching an equilibrium. The sharp rise corresponds to nucleation process. When the critical supersaturation value is exceeded, the crystallization could begin in a homogeneous system. Supersaturation keeps increasing until nucleation takes place. The decrease of the concentrations occur when crystal growth dominates on nucleation process. When it reaches a plateau, supersaturation is decreased and there is no more nucleation. Until the discharge ends, there is only crystallization process in the battery. The highest driving force and the highest capacity is obtained at 1.0 % H₂O content in the electrolyte.

At high water contents in Figure 6-2, the supersaturation value is increased and the sharp rise is higher than at low water contents. Also, the plateau becomes less and less flat by increasing the water content since the nucleation continues during the crystallization growth at high water contents. Moreover, the driving force for the crystallization is higher than that at low water contents. This larger driving force results in faster crystallization reaction in the battery.

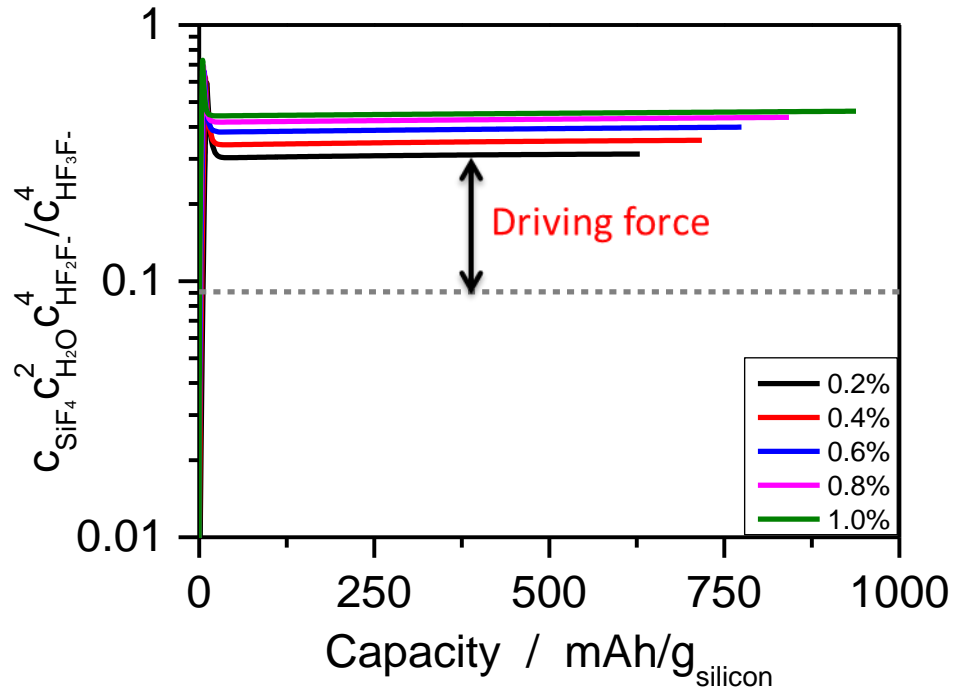


Figure 6-1 Crystallization criterion (dash) and driving force (line) at various low water contents. The effect of water addition on the driving force, crystallization, and nucleation are implemented.

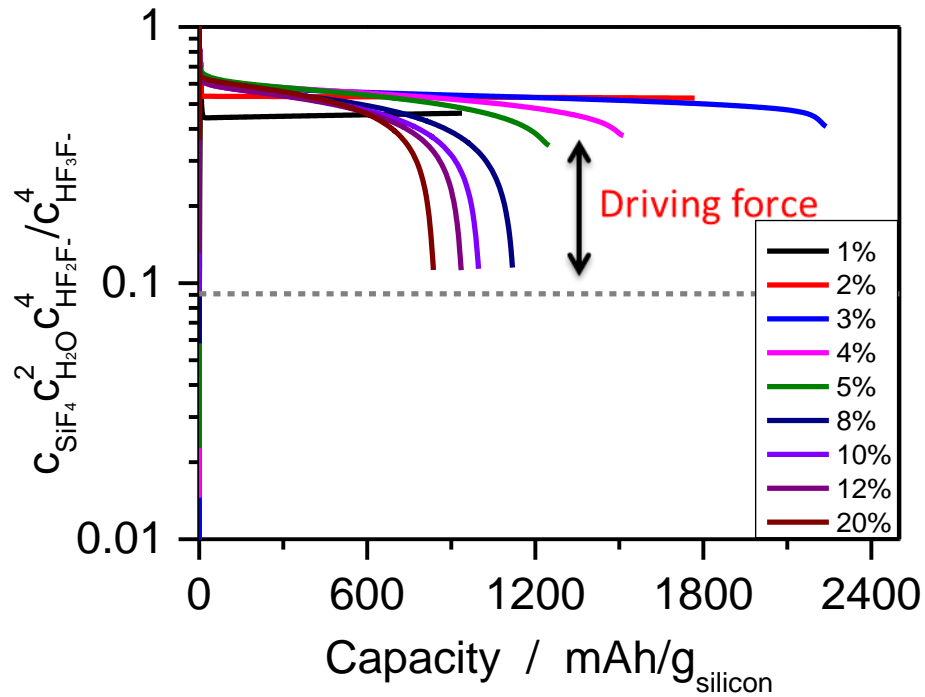


Figure 6-2 Crystallization criterion (dash) and driving force (line) at various high water contents. The effect of water addition on the driving force, crystallization, and nucleation are implemented.

In equilibrium, the concentration of silicon tetrafluoride c_{SiF_4} is inversely proportional to the square of the concentration of water $c_{\text{H}_2\text{O}}^2$. This is a good approximation of the nucleation criterion (equation 6.4), since $c_{(\text{HF})_2\text{F}^-}$ and $c_{(\text{HF})_3\text{F}^-}$ remain nearly constant. Thus, when there is more water added to the electrolyte, the concentration of silicon tetrafluoride c_{SiF_4} is decreased in order to satisfy the equilibrium conditions.

Figure 6-3 and Figure 6-4 present our simulation results for the concentration of silicon tetrafluoride c_{SiF_4} at anode and cathode with various water contents. There is a sharp rise initially in each case, then the concentrations reach a plateau. The peak points decrease by increasing the water content due to high consumption of SiF_4 at high water contents. The equilibrium relation between c_{SiF_4} and $c_{\text{H}_2\text{O}}^2$ is not clear in the simulation results which are shown in Figure 6-3 and Figure 6-4. Possible reasons are: influence of the $c_{(\text{HF})_2\text{F}^-}$ and $c_{(\text{HF})_3\text{F}^-}$ on equation 6.4 is high at low water contents and the driving force is low and increases with adding H_2O . In contrast, at high water contents, such as for 2 % and 20 %, the relation between c_{SiF_4} and $c_{\text{H}_2\text{O}}^2$ can be seen clearly from the figures. When the water concentration is increased by one order of magnitude, the silicon tetrafluoride concentration decreases by almost two orders of magnitudes.

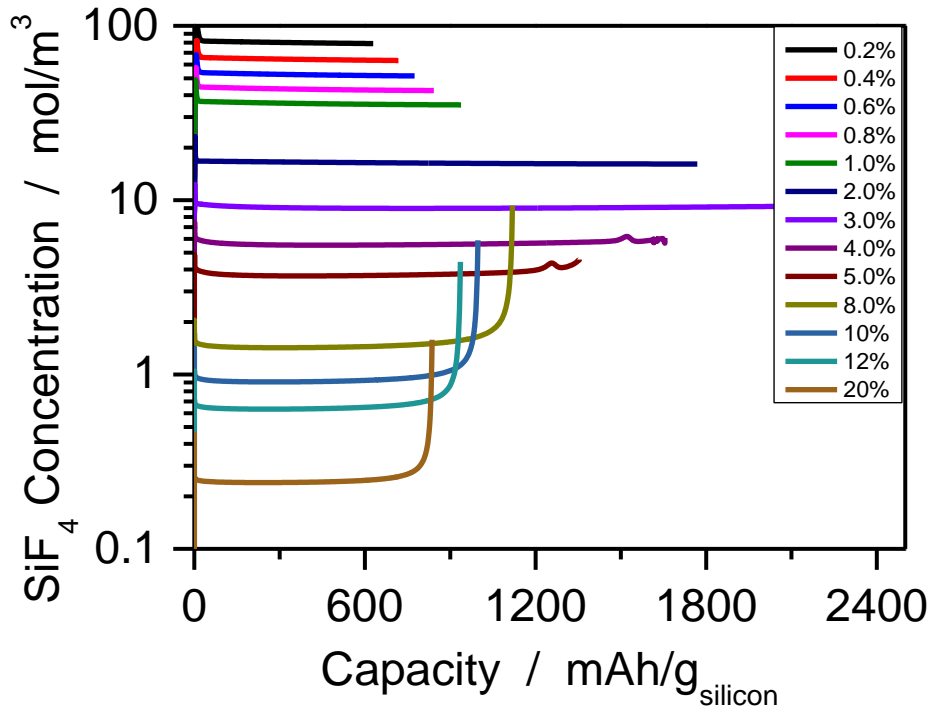


Figure 6-3 SiF₄ concentrations at anode versus capacity for various water contents. The influence of water addition on the concentration is shown at 0.3 mA cm⁻².

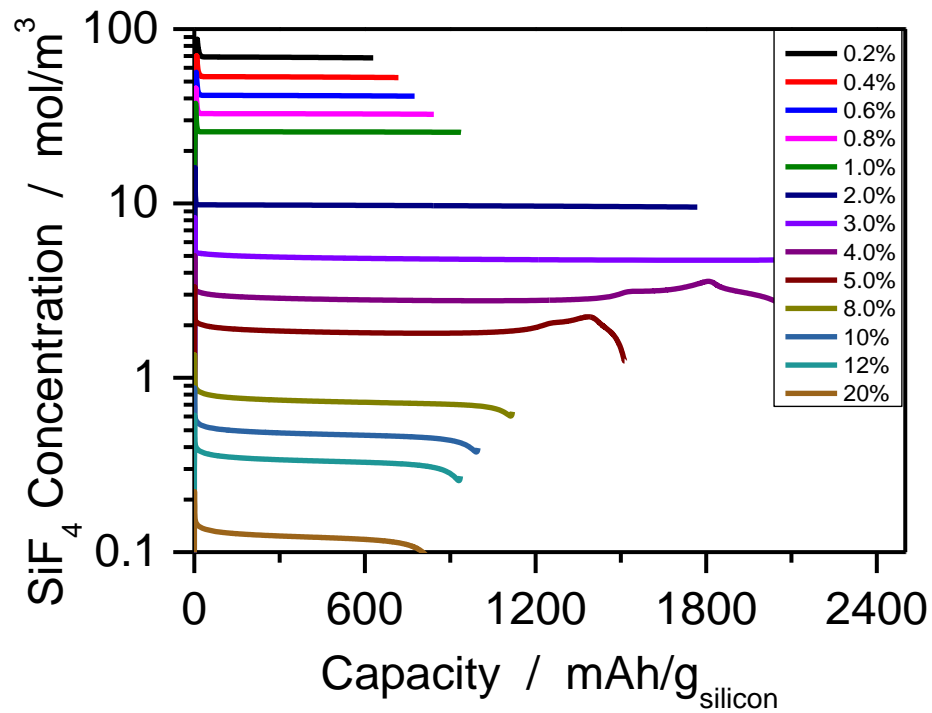


Figure 6-4 SiF₄ concentrations at cathode versus capacity for various water contents. The influence of water addition on the concentration is shown at 0.3 mA cm⁻².

6.2 Half-cell Potentials

If a battery is discharged, the electrode potential deviates from the thermodynamically determined OCV. This deviation is called overpotential. Since this overpotential significantly affects the discharge performance of the battery, implementation of the overpotential is crucial for the Si-air battery simulation.

In the literature⁵², the initial drop at the air cathode is attributed to dissolved oxygen in the electrolyte (see Chapter 3). Since external oxygen molecules are difficult to access, the cathode potential is decreased resulting in overpotential of the electrode. Figure 3-10 is shown again to present the cathode overpotential is constant at 0.4 V after the initial drop of electrode potential.

Figure 6-6 shows our simulation result for 0.1 % H₂O content in the electrolyte and at 0.3 mA cm⁻² discharge current density. We present the anode and cathode overpotentials in our simulation. In order to compare with the experimental results which are shown in Figure 6-5, very low water content is employed in the simulation.

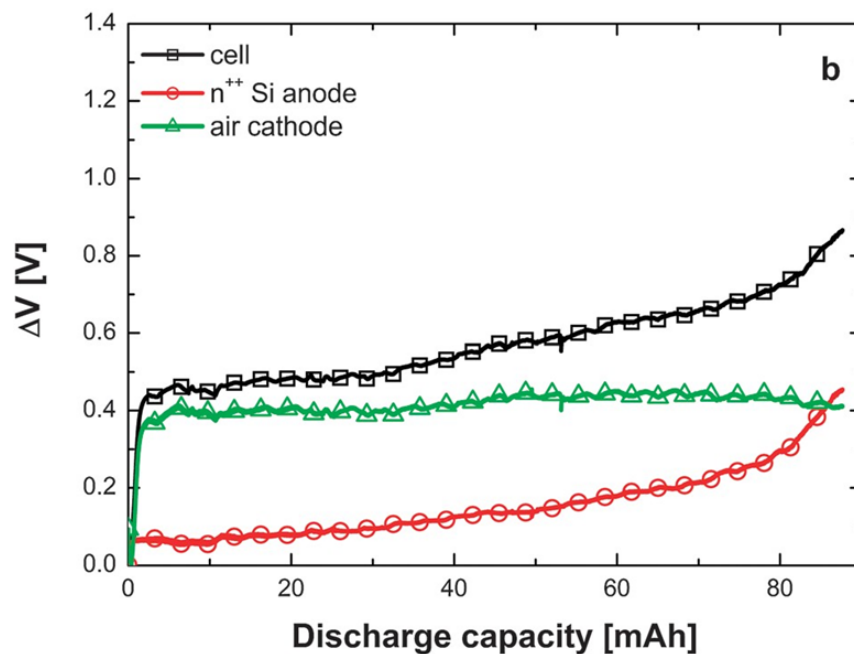


Figure 6-5 Experimental overpotential⁵² of the Si-air cell, anode and cathode at 0.3 mA cm⁻²

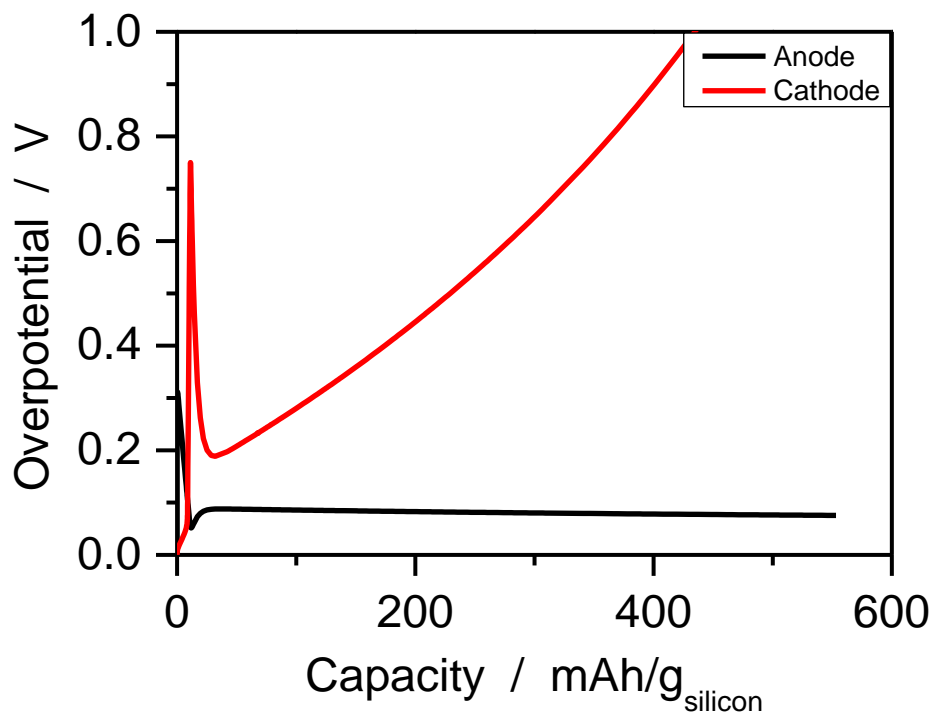


Figure 6-6 Simulated overpotentials of anode and cathode with 0.1 % H₂O at 0.3 mA cm⁻²

In our simulation result shown in Figure 6-6, the cathode overpotential deviates from the experimentally observed one. There is a peak which increases up to 0.7 V and then decreases again until 0.2 V in the beginning of the operation. Then, it surges immediately and leads to termination of discharge. The reason for the initial peak and the decrease are discussed in the previous section (see section 6.1) and the reason for the surge will be explained below. There is no plateau in our simulation results for the cathode overpotential. Because, there is pore clogging which results in reduction on the oxygen diffusion pathway due to the crystallization process in the cathode. Therefore, the concentration of oxygen is decreased leading to overpotential.

Moreover, the dissolved O₂ molecules consumption corresponds to the same initial peak point (Figure 6-6), thus it may also influence the overpotential of the cathode. O₂ concentration at the cathode is shown in Figure 6-7 (the capacity scale is reduced to see the drop clearly). Initially, there is a drop in the O₂ concentration down to 0.3 mol m⁻³ due to the consumption of the

dissolved oxygen molecules in the electrolyte. The dip point corresponds to peak point in Figure 6-6. The slow decrease on O_2 concentration after this point is due to the reduced diffusion pathway. Here, the cathode reaction is in the Tafel regime. Therefore, slight deviations in the O_2 concentration affect the overpotential substantially. This is the reason why the cathode overpotential surges immediately in Figure 6-6.

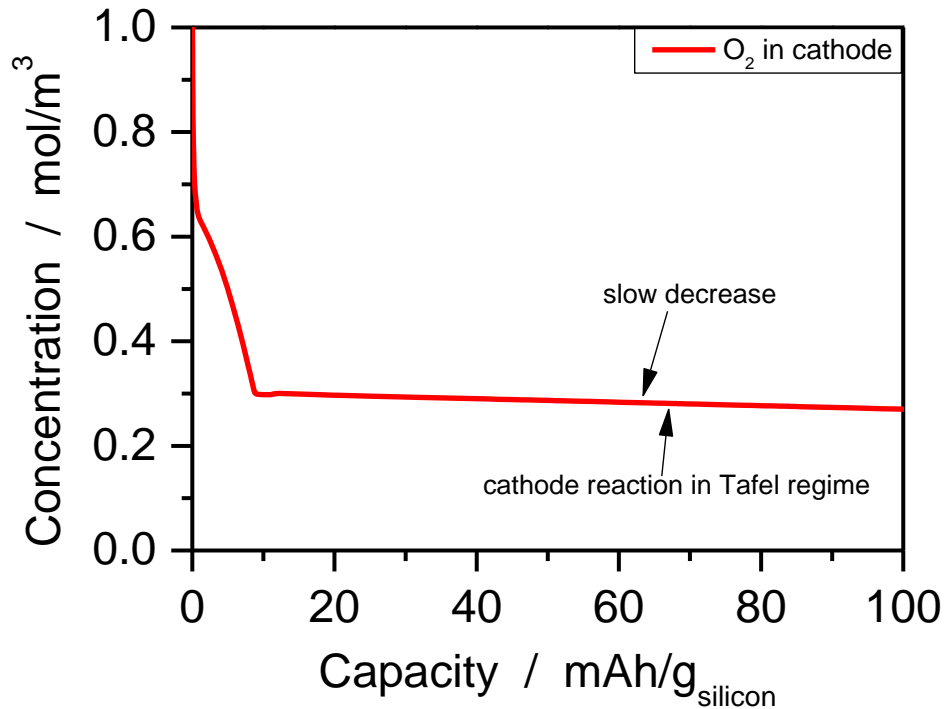


Figure 6-7 O_2 concentration at cathode with 0.1 % H_2O at 0.3 mA cm^{-2}

In the simulation results shown in Figure 6-6, the anode overpotential, however, is similar to the experiment (Figure 6-5). There is a peak which increases up to 0.3 V, then decreases until 0.05 V and remains almost constant at 0.08 V during the discharge process. This peak occurs due to the concentrations of $(HF)_2F^-$ and $(HF)_3F^-$ across the electrodes. The reason will be discussed below. The dip of the overpotential corresponds to the nucleation.

The concentrations of $(HF)_2F^-$ and $(HF)_3F^-$ at anode and cathode are shown in Figure 6-8 and Figure 6-9. In order to see the dynamics, the capacity axis is enlarged in the figures. In the beginning of the discharge, the concentrations of $(HF)_2F^-$ and $(HF)_3F^-$ sharply decrease or

increase depending on the electrode and the species. Then, $(\text{HF})_2\text{F}^-$ concentrations increase reaching a peak point and decrease again until the equilibrium, while $(\text{HF})_3\text{F}^-$ concentrations decrease reaching a dip point and increase again up to the equilibrium.

In the beginning of the discharge, the nucleation process cannot begin as the saturation level for SiF_4 is not reached. Therefore, only the cathodic and anodic electrochemical reactions take place in the battery. Consequently, the production and consumption of $(\text{HF})_2\text{F}^-$ and $(\text{HF})_3\text{F}^-$ are not balanced, and thus, there are alterations on the concentration profiles in Figure 6-8 and Figure 6-9.

On the anode electrode, as a result of the electrochemical reaction, 8 moles $(\text{HF})_3\text{F}^-$ are produced while 12 moles $(\text{HF})_2\text{F}^-$ are consumed. Hence, there is a sharp increase on the concentration of $(\text{HF})_3\text{F}^-$ and a sharp decrease on the concentration of $(\text{HF})_2\text{F}^-$. Because of this, there is a peak on the anode overpotential. On the cathode side, the electrochemical reaction results in production of 16 moles $(\text{HF})_2\text{F}^-$ and consumption of 12 moles $(\text{HF})_3\text{F}^-$. That is why there is a sharp increase and a decrease on the concentrations at early stages. However, once the transport between the electrodes can balance the concentrations in the whole cell, 4 moles of $(\text{HF})_3\text{F}^-$ are consumed and 4 moles of $(\text{HF})_2\text{F}^-$ are produced overall the battery until the nucleation and growth starts. Since $(\text{HF})_2\text{F}^-$ is the reactant and $(\text{HF})_3\text{F}^-$ is the product of the anodic electrochemical reaction, the production of $(\text{HF})_2\text{F}^-$ and the consumption of $(\text{HF})_3\text{F}^-$ overall the battery turns out the anodic electrochemical reaction advantage. That is why the anode overpotential decreases after the initial peak. However, once the nucleation and growth begins, the consumption and production amounts are balanced and the concentration profiles reach a plateau. As a result, the anode overpotential reaches a plateau as well.

The effect of water addition into the RTIL electrolyte is also discussed in the literature review (see Chapter 3). Figure 6-10 shows the effect of water addition on the anode and cathode overpotential. The simulations are performed with 1 % and 10 % H_2O and discharging at 0.3 mA cm^{-2} . There is a sharp increase in the anode overpotential due to the nucleation. In contrary to the case of very low water content (Figure 6-6), the cathode overpotential is quite

low until the discharge termination (termination due to pore clogging) at 1 % H₂O or remains quite low if the pore clogging is prevented at 10 % H₂O.

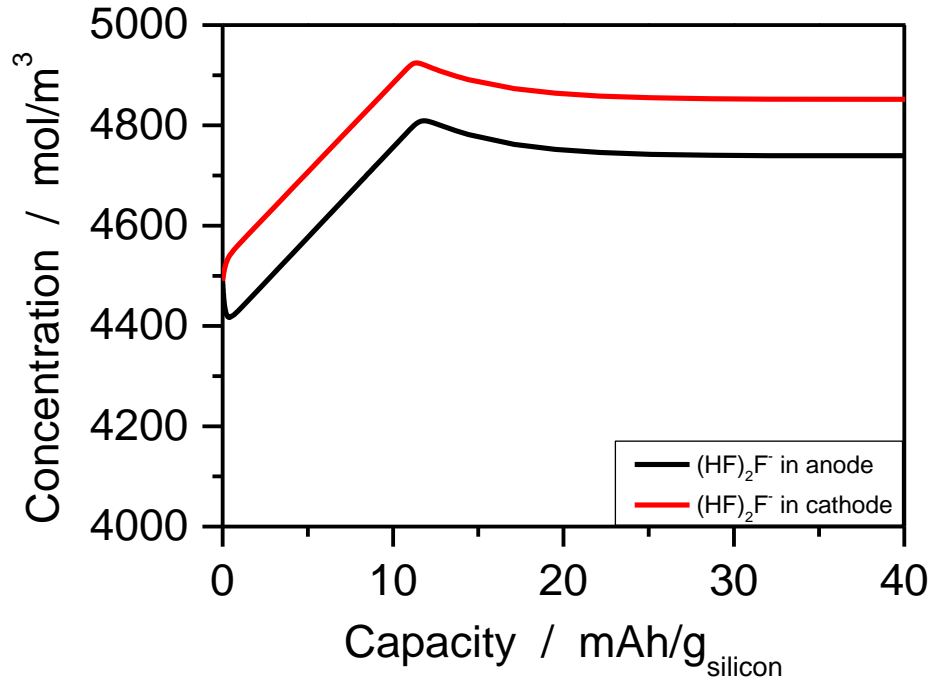


Figure 6-8 $(\text{HF})_2\text{F}^-$ concentrations at anode and cathode during the discharge with 0.1 % H₂O at 0.3 mA cm⁻²

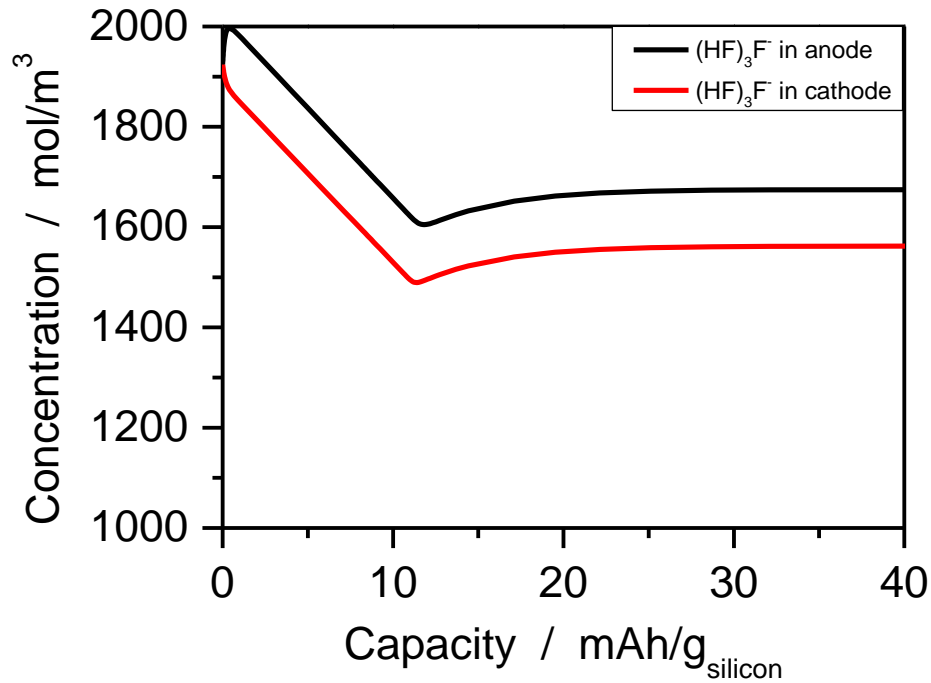


Figure 6-9 $(\text{HF})_3\text{F}^-$ concentrations at anode and cathode during the discharge with 0.1 % H₂O at 0.3 mA cm⁻²

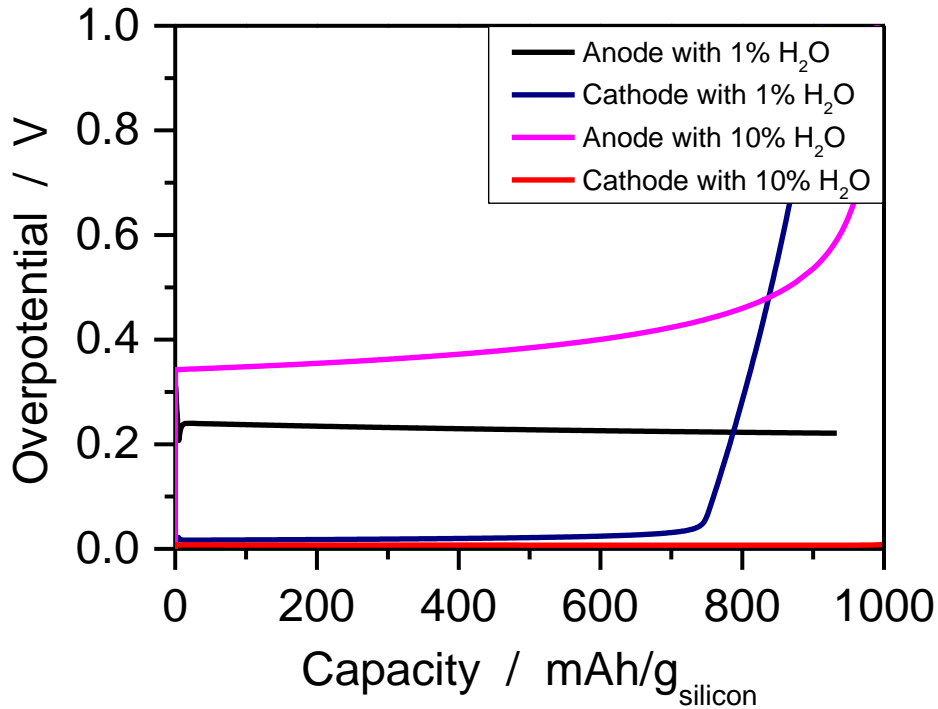


Figure 6-10 Overpotentials of anode and cathode during the discharge with 1 % H₂O and 10 % H₂O at 0.3 mA cm⁻²

At low water contents (0.1 % H₂O and 1 % H₂O), the discharge process terminates due to the cathode electrode. Clearly, this effect can be seen in Figure 6-6 and Figure 6-10 as the cathode overpotential increases significantly. Since the pore clogging is delayed by increasing the water content up to 1 % H₂O, the cathode overpotential does not surge at early stages. However, once high water content (10 % H₂O) is employed, the discharge process is now limited by the anode electrode due to the shift of the crystallization reaction into the anode. The shift of the crystallization reaction into the anode is also the reason for the delayed pore clogging for 1 % H₂O content. The cathode overpotential is quite small as most of the nucleation and growth occur in anode, and thus, the oxygen diffusion path is not blocked (pore clogging) in cathode side.

6.3 Spatial Distribution of Crystallization

In this section, volume fractions of the electrolyte, SiO_2 , and the electrode materials will be presented.

The volume fractions in the electrodes change due to the crystallization and dissolution processes. Since both electrodes have porous structures; producing solid crystal particles and depositing them into these pores causes a decrease in the electrolyte volume fraction and possibly in the electrode material volume fraction. In the cathode, electrode material is carbon and it has always a fixed volume fraction as it does not contribute in any reactions. Therefore, only the electrolyte volume fraction decreases once solid particles start to form. However, in the anode, electrode material is silicon metal and it participates in the anode reaction. Therefore, both silicon metal and electrolyte change in case of crystal formation at the anode. As discussed in section 5.1, the separator is reaction-free zone, and thus, the electrolyte always has a volume fraction of 1.

Firstly, we represent the discharge profiles with 0.5 % H_2O , 3 % H_2O , and 10 % H_2O in Figure 6-11. On each profile, we mark four time points with red circles that will be used later for comparing the crystal and electrolyte volume fractions. The discharge curves will be explained in section 6.4. Secondly, the volume fractions of electrolyte, graphite, silicon, and crystal are shown in Figure 6-12, Figure 6-14, and Figure 6-16. The data points for these figures are taken from the 4th points on the discharge curves. Also, we present the electrolyte volume fractions for each discharge curves; in this case, data points are taken from the four points on the discharge curves.

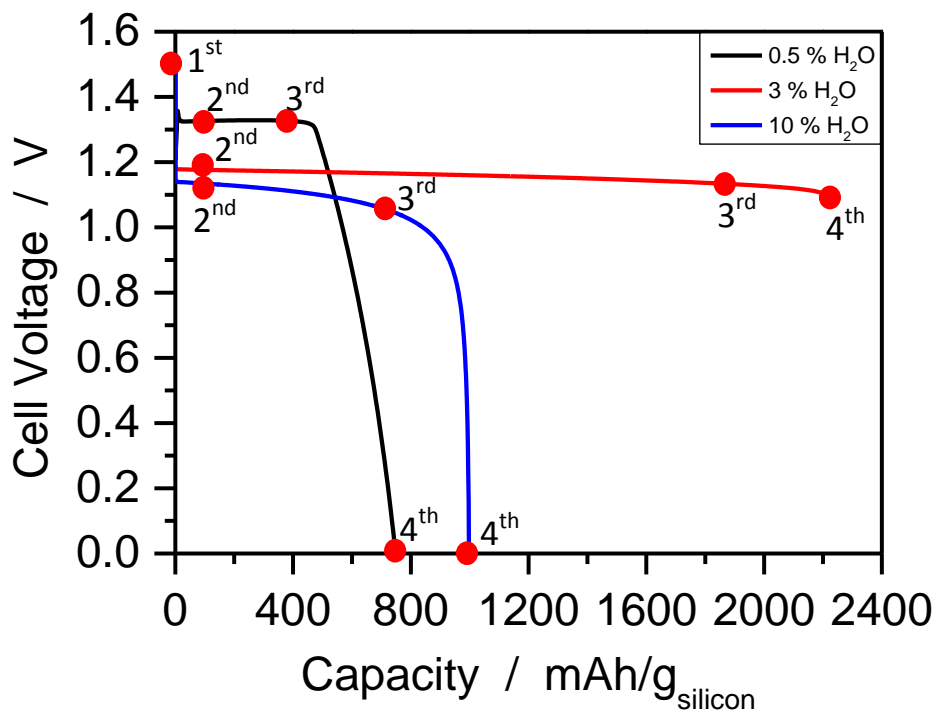


Figure 6-11 Discharge curves (with 4 time points marked) with various water contents at 0.3 mA cm^{-2} .

In Figure 6-12, the volume fractions in anode and cathode are shown for $0.5 \% \text{ H}_2\text{O}$ at 0.3 mA cm^{-2} . The data points are taken at the end of discharge (4th point for $0.5 \% \text{ H}_2\text{O}$ in Figure 6-11). One can see that the crystal volume fraction is maximum near the oxygen channel and decreases until 0.1 in the cathode, while there is almost no crystal in the anode. On the contrary to crystal volume fraction, the electrolyte volume fraction is minimum near the oxygen channel and increases through the cathode, while it is increased to 0.4 in the anode. The graphite has a fixed volume, but the silicon metal is dissolved and its volume fraction is lowered to 0.7 at the end of discharge.

At low water content ($0.5 \% \text{ H}_2\text{O}$), the crystallization mostly take place in the cathode. The reason why crystallization is higher in the cathode is the production of H_2O and $(\text{HF})_2\text{F}^-$ at the cathode. These two species are the reactants for the crystallization reaction. Hence, the crystallization in the cathode is favored. The fast crystallization in the cathode results in pore

clogging that leads to inhomogeneous oxygen concentration due to the blocked diffusion pathway. This is also why the crystal volume fraction is inhomogeneous in the cathode.

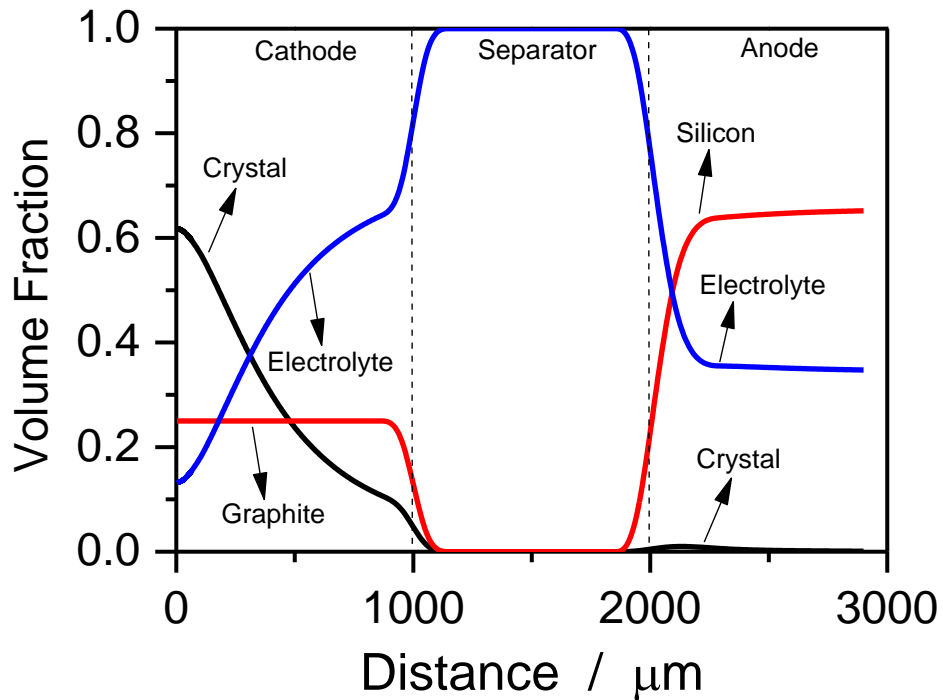


Figure 6-12 Volume fractions in cathode and anode with 0.5 % H₂O at the end of discharge

The electrolyte volume fractions during the discharge process (Figure 6-11) are depicted in Figure 6-13. The data points are taken from the discharge curve. The electrolyte volume fraction decreases during the discharge process in the cathode. However, it increases in the anode. The crystallization rate determines whether electrolyte volume fraction increases or decreases. In the cathode, there is fast crystallization while the crystallization is slow in the anode. Therefore, the electrolyte volume fraction is increased due to the slow crystallization in the anode. As discussed above, the crystal volume fractions are high near the oxygen channel at the end of discharge. Hence, in the cathode, the electrolyte volume fraction decreases due to the crystal growth.

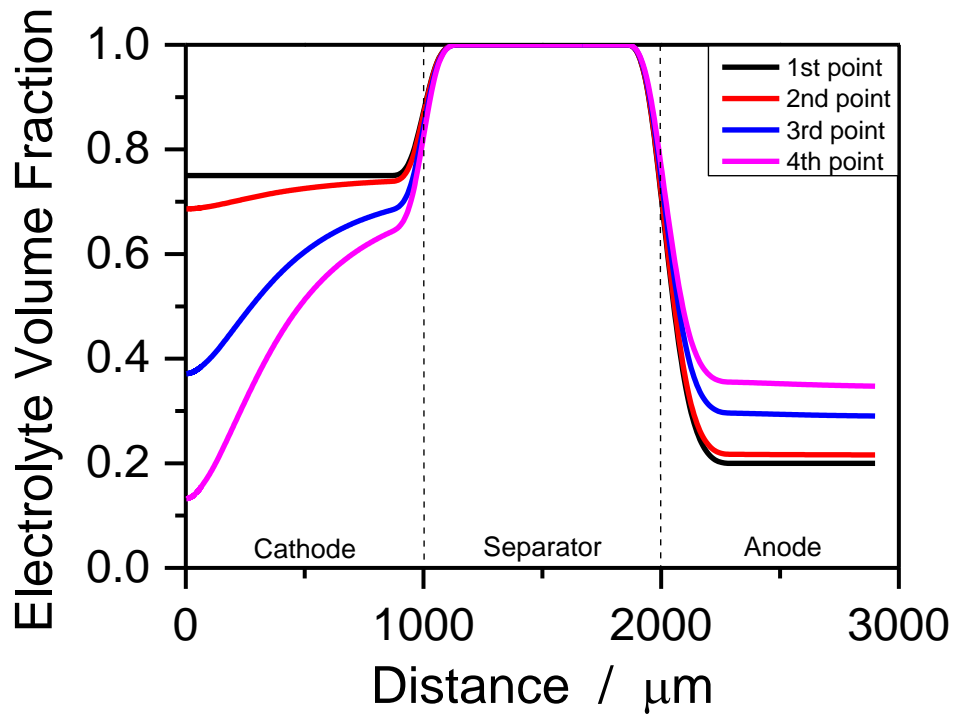


Figure 6-13 Electrolyte volume fractions during the discharge of the battery with 0.5 % H₂O

Figure 6-14 shows the volume fractions at the end of discharge (4th point for 3 % H₂O in Figure 6-11) with 3 % H₂O at 0.3 mA cm⁻². The crystal volume fractions in the cathode show a gradient from 0.5 to 0.25, while they remain constant around 0.6 in the anode. As a result of this, the electrolyte volume fractions increase from 0.25 to 0.5 in the cathode and decrease down to 0 in the anode. Also, the silicon metal dissolution is high, and thus, its volume fraction is reduced to 0.35.

The maximum discharge capacity is obtained with 3 % H₂O content during the simulations. Therefore, one can expect the highest average crystallization volume fractions through the battery when 3 % H₂O is simulated. This will be discussed in the next section.

At 3 % H₂O content, low concentration of SiF₄ determines the crystallization. Since it is produced by the anode reaction, the crystallization in anode dominates the system. Figure 6-14 shows that the highest crystal volume fractions are obtained at the anode side. Thus, the crystallization reaction is shifted into the anode by adding more water into the electrolyte.

Therefore, there is more crystallization in the anode than the cathode. This prevents pore clogging at early stages leading to more homogenous (than 0.5 % H₂O) crystal volume fractions in the cathode. The crystal volume fractions are homogeneous in the anode side as SiF₄ concentration, which determines the crystallization, is also homogeneous. Moreover, the electrolyte volume fraction reaches zero in the last compartment of the anode. This low volume fraction results in the battery termination.

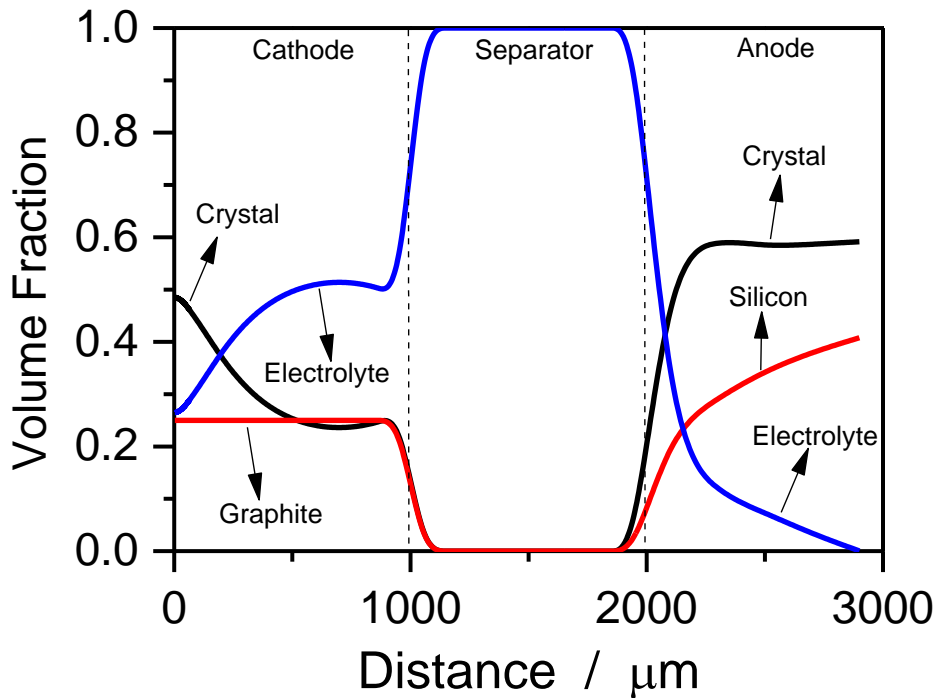


Figure 6-14 Volume fractions in cathode and anode with 3 % H₂O at the end of discharge

The electrolyte volume fractions during the discharge process (Figure 6-11) are shown in Figure 6-15. The data points are taken from the discharge curve. Between the 2nd and 3rd data points, the electrolyte volume fractions are reduced significantly in both electrodes. In the cathode, the electrolyte volume fractions are reduced from 0.8 to 0.25 in the first compartments. Then, the volume fractions show an increase through the cathode up to 0.5. In the anode electrode, the decrease on the electrolyte volume fractions is continuous and reaches 0 at the end of discharge.

The reason for the decrease of the electrolyte volume fractions is crystal growth. Due to the low crystallization in the cathode, the electrolyte has higher volume fractions during the discharge process. However, as more crystals form in the anode due to the fast crystallization; the electrolyte volume fractions decrease continuously.

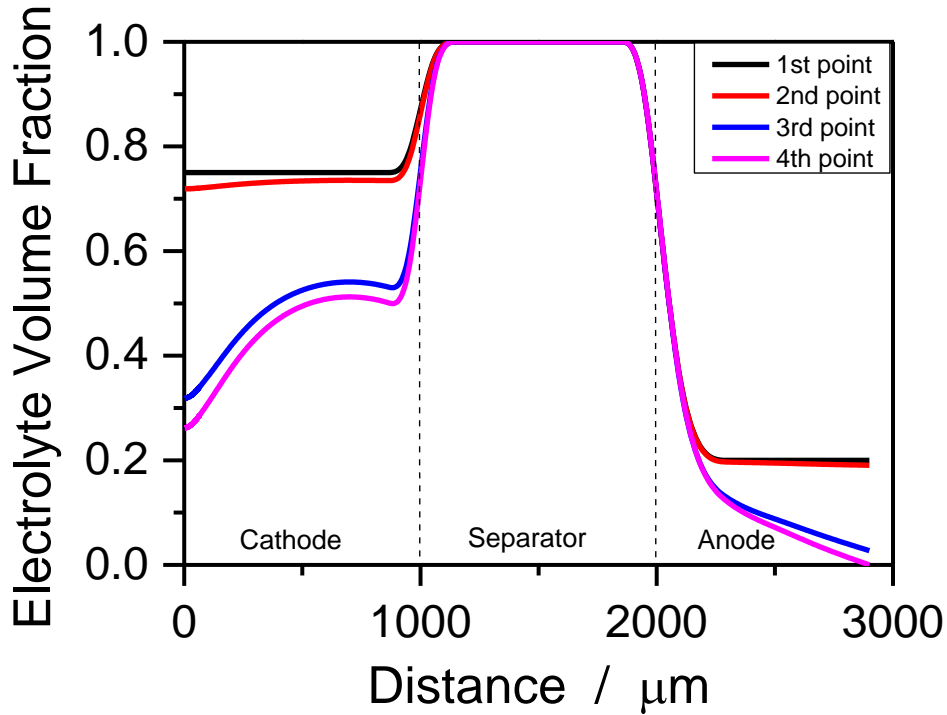


Figure 6-15 Electrolyte volume fractions during the discharge of the battery with 3 % H₂O

Figure 6-16 shows the volume fractions at the end of discharge (4th point for 10 % H₂O in Figure 6-11) with 10 % H₂O at 0.3 mA cm⁻². The electrolyte volume fractions show a constant profile in both electrodes. In the cathode, the electrolyte volume fractions are similar to initial values. However, they are reduced to 0.05 in the anode. The crystal volume fractions are quite low, around 0.03, in the cathode. On the other side, the crystal volume fractions are around 0.35. Dissolution of the silicon metal on the anode is not as high as in the 3 % H₂O case.

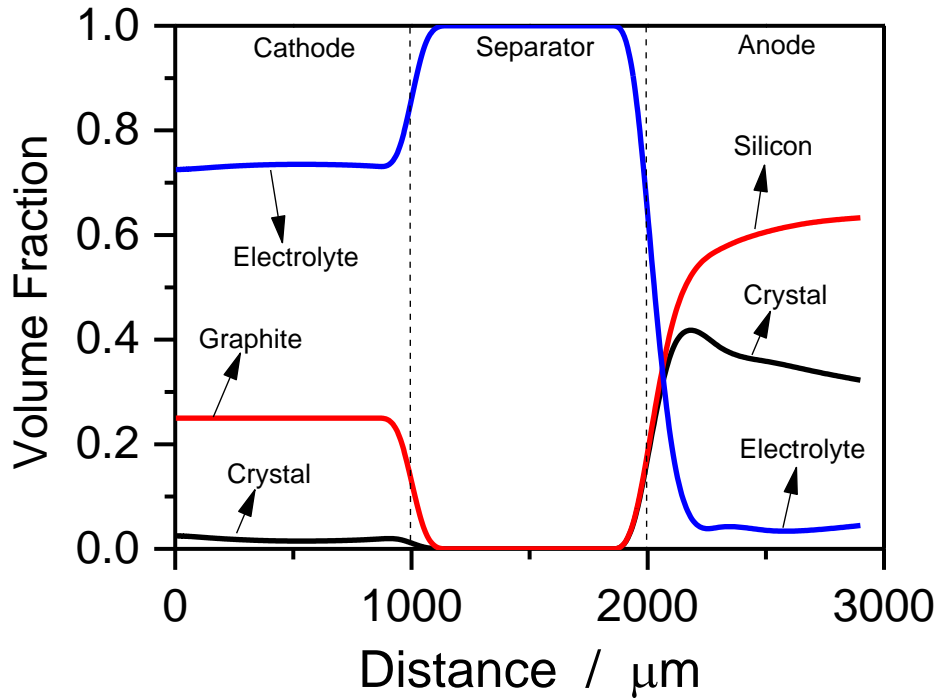


Figure 6-16 Volume fractions in cathode and anode with 10 % H₂O at the end of discharge

Addition of more than 3 % H₂O into the electrolyte results in decreased discharge capacity. The reason of capacity fading will be discussed later. However, lower capacity means less crystal volume fractions in the battery. This argument is corroborated by Figure 6-16. The crystal volume fractions, especially in the cathode, are smaller than for the 3 % H₂O case. The reason why the anode electrode has more crystallization than the cathode is; that at the high water contents, SiF₄ concentration still determines the crystallization. Hence, the anode has larger crystallization resulting in the small volume fractions of the electrolyte in the anode that trigger the battery termination.

The electrolyte volume fractions are shown in Figure 6-17. In this case, electrolyte has homogenous volume fractions over the anode which is contrary to 3 % H₂O case. In the cathode, the electrolyte volume fractions do not change as the crystallization is quite low. However, the crystallization in the anode is quite fast due to the high water content. When the

silicon metal dissolves and produces SiF_4 , it crystallizes immediately. Therefore, the electrolyte has homogenous volume fractions through the anode.

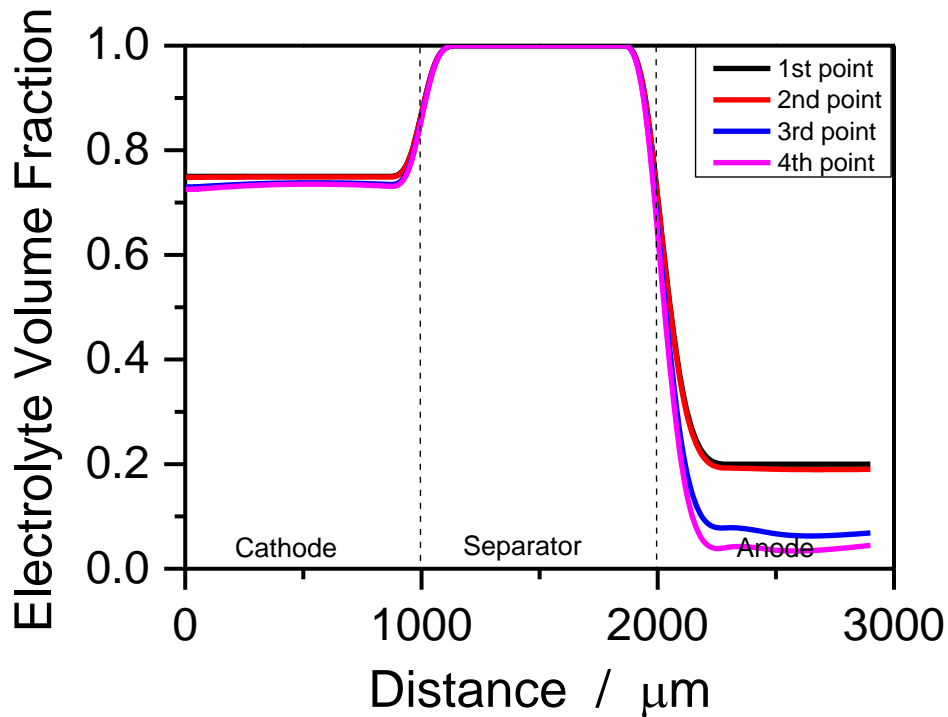


Figure 6-17 Electrolyte volume fractions during the discharge of the battery with 10 % H_2O

In conclusion, the average crystal volume fractions in the electrodes are shown depending on the water content in Figure 6-18. This figure summarizes the remarkable effect of water addition into the electrolyte. The crystal volume fractions in the cathode increase up to 0.45 initially by adding more water into the electrolyte, and then decrease to 0.05 at 20 % H_2O content. The anode has very low crystal volume fractions at low water contents; however, they increase up to 0.65 by adding water and then decrease to 0.35 by further addition of water.

Clearly, the highest total crystal volume fraction is obtained for 3 % H_2O . At low water contents (< 3 % H_2O), crystallization in the cathode is higher. Contrary to low water contents, the anode has more crystallization for high water contents (> 3 % H_2O). Furthermore, the highest capacity was reached for 15 % H_2O content in the experimental studies.⁴⁹ Due to the parameter fitting and assumptions in the simulation, the highest capacity ($2250 \text{ mAh g}_{\text{silicon}}^{-1}$) is

achieved with 3 % H₂O. This result qualitatively agrees with experiments; the crystallization in the cathode dominates at low water contents, while the crystallization in the anode dominates at high water contents.

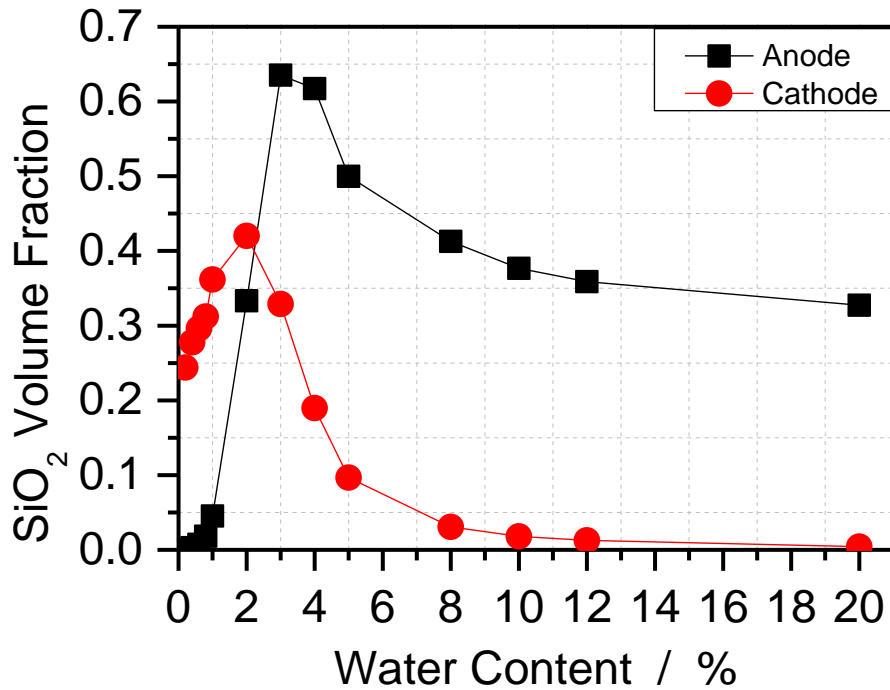


Figure 6-18 Average SiO₂ volume fractions at anode and cathode with various water contents

6.4 Discharge at Various Water Contents

Capacities are often used characterized to batteries. The capacity of a battery is defined as the amount of charge it can deliver. In this section, we discuss the capacity of the Si-air battery.

The effect of water addition on the discharge capacity of Si-air batteries is the main focus of this work. Here, we discuss the effect of water addition to the electrolyte on the discharge capacity.

In Si-air batteries, silicon metal is the active material and participates in the anode reaction. Therefore, we relate capacities to the mass of silicon (rather than to the mass of graphite) in the simulation results.

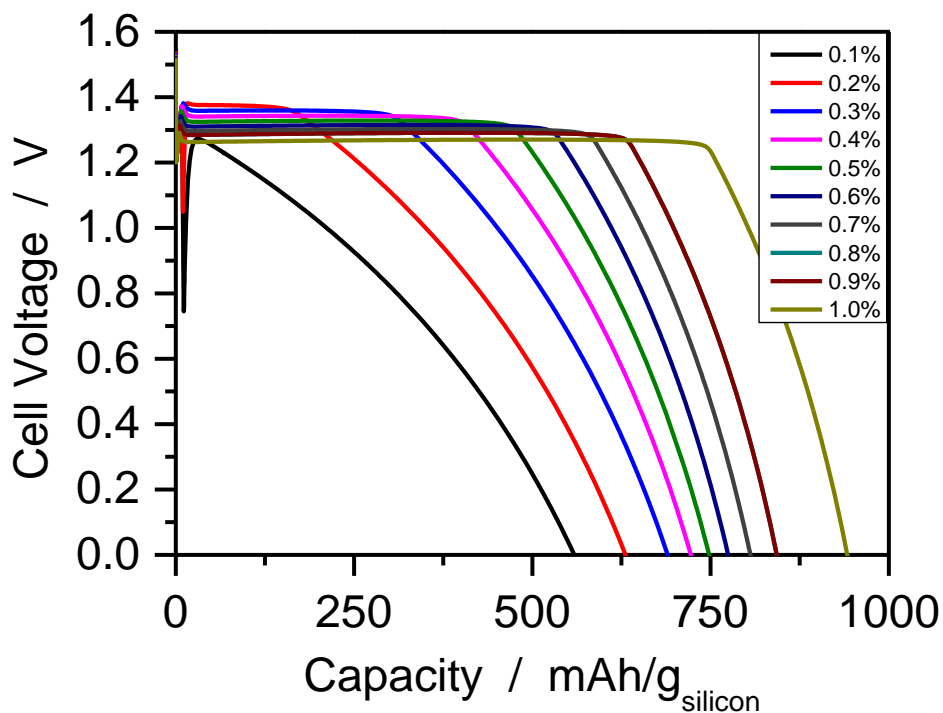


Figure 6-19 Discharge capacity of the Si-air battery at low water contents with 0.3 mA cm^{-2}

Figure 6-19 shows the discharge curves at low water contents up to 1 % H_2O . The curves show the voltage plateaus starting from 1.4 V at 0.2 % H_2O . The plateaus are extended by further addition water, as well as the discharge capacities are increased. We discuss the discharge capacities now, the decrease of the voltage plateaus will be discussed later.

Figure 6-20 summarizes the effect of water addition on the discharge capacity. The capacity values are taken at the end of discharge curves, i.e., at 0 V, in Figure 6-19. The effect of discharge capacity increase by adding water into the electrolyte can be seen in this figure. The discharge capacity at 0.1 % H_2O is almost doubled at 1 % H_2O . The reason why the capacity increases by adding water into the electrolyte was discussed briefly in the previous section. At very low water contents, the crystallization occurs mostly in the cathode side, especially near the oxygen inlet. When the pores are filled with the solid crystal particles, the oxygen cannot diffuse into cathode, separator, and anode anymore. Due to this reason, battery terminates at early stages which results in less discharge capacity.

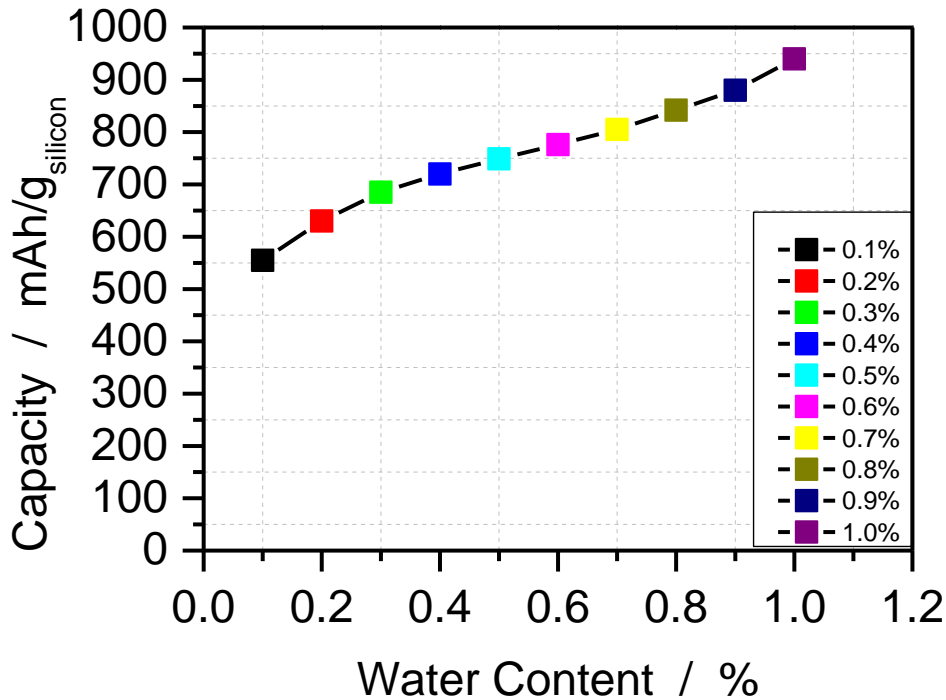


Figure 6-20 The effect of low water contents on the discharge capacity. Data points are taken at the end of discharge.

However, adding more water into the electrolyte leads to a shift of the crystallization reaction into the anode. Therefore, the solid crystal particles are formed more and more in the anode pores by adding more water. This prevents the early stage pore clogging at the cathode and leads to higher discharge capacities. On the other hand, this process also causes a more constant O_2 concentration and longer and flatter voltage plateaus which can be seen on the discharge curves.

Figure 6-21 shows the discharge curves at high water contents up to 20 % H_2O . The resulting discharge capacities are higher compared to low water contents. However, the voltage plateaus are decreased at high water contents. The maximum capacity, which is around $2250 \text{ mAh g}_{\text{silicon}}^{-1}$, is achieved with 3 % H_2O in the electrolyte. Further addition of water causes a decrease of the discharge capacities and the voltage plateaus become less flat. At 20 % H_2O , the discharge capacity is $820 \text{ mAh g}_{\text{silicon}}^{-1}$, which is around one third of the 3 % H_2O capacity. Due to numerical problems in the simulation; 3 % H_2O , 4 % H_2O , and

5 % H₂O terminate around 1.1 V, 1.05 V, and 0.8 V, respectively. We discuss the discharge capacities now, the decrease on the voltage plateaus will be discussed later.

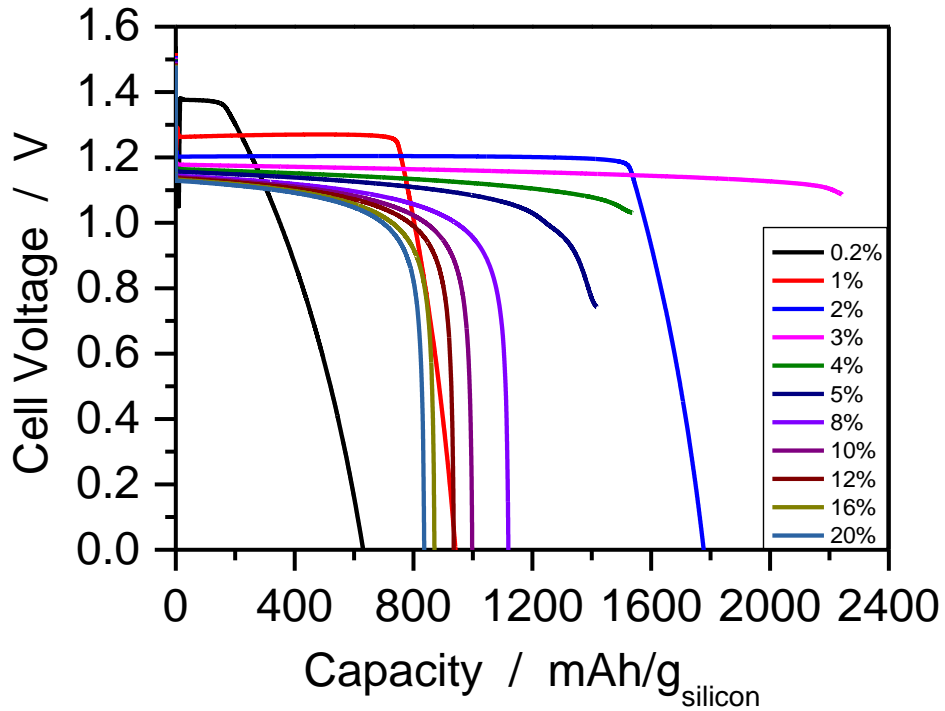


Figure 6-21 Discharge capacity of the Si-air battery at high water contents with 0.3 mA cm⁻²

The effect of water addition on the discharge capacity at high and low water contents are summarized in Figure 6-22. The capacity values are taken at the end of discharge, i.e., 0 V, in Figure 6-19 and Figure 6-21. Clearly, the capacity values increase from 600 mAh g_{silicon}⁻¹ to 2250 mAh g_{silicon}⁻¹ by increasing the water content from 0.1 % H₂O to 3 % H₂O. Further addition of water decreases the capacity values back to 800 mAh g_{silicon}⁻¹.

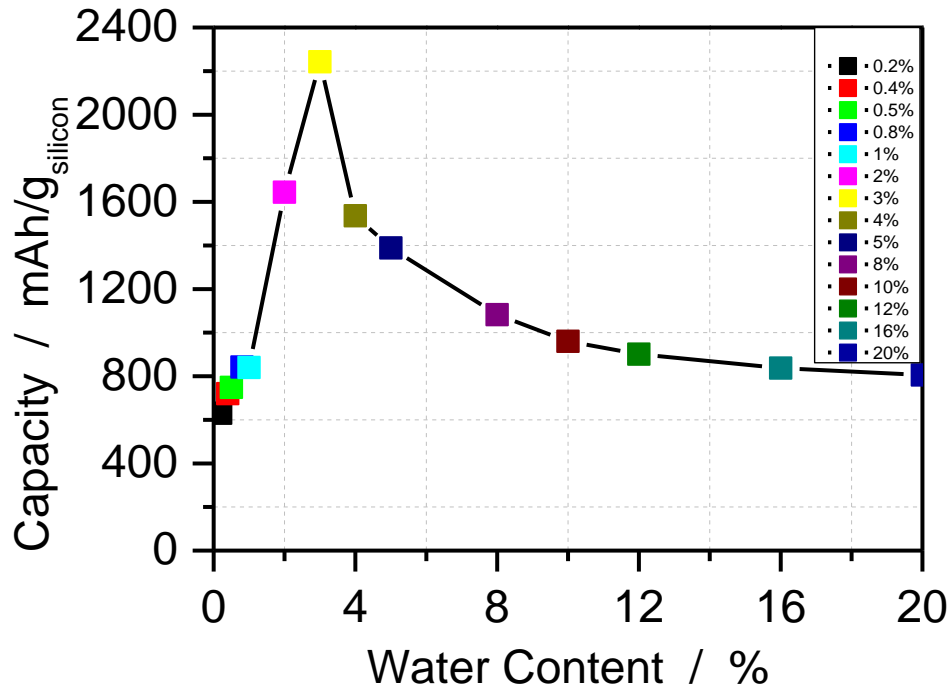


Figure 6-22 The effect of high water contents on the discharge capacity

The discharge capacities shown in Figure 6-21 and Figure 6-22 are higher than for low water contents (see Figure 6-19). The discharge capacities are maximal at 3 % H₂O, for which both the anode and the cathode are used for storing the discharge product. As described above, the capacities increase below 3 % H₂O, because pore clogging in the cathode and slow oxygen transport become less and less of an issue. Above 3 % H₂O, the storage space in the cathode becomes less used and the discharge is limited by pore clogging in the anode. At low water contents, the cell exhibits the same discharge capacities at very high water contents as at low water contents.

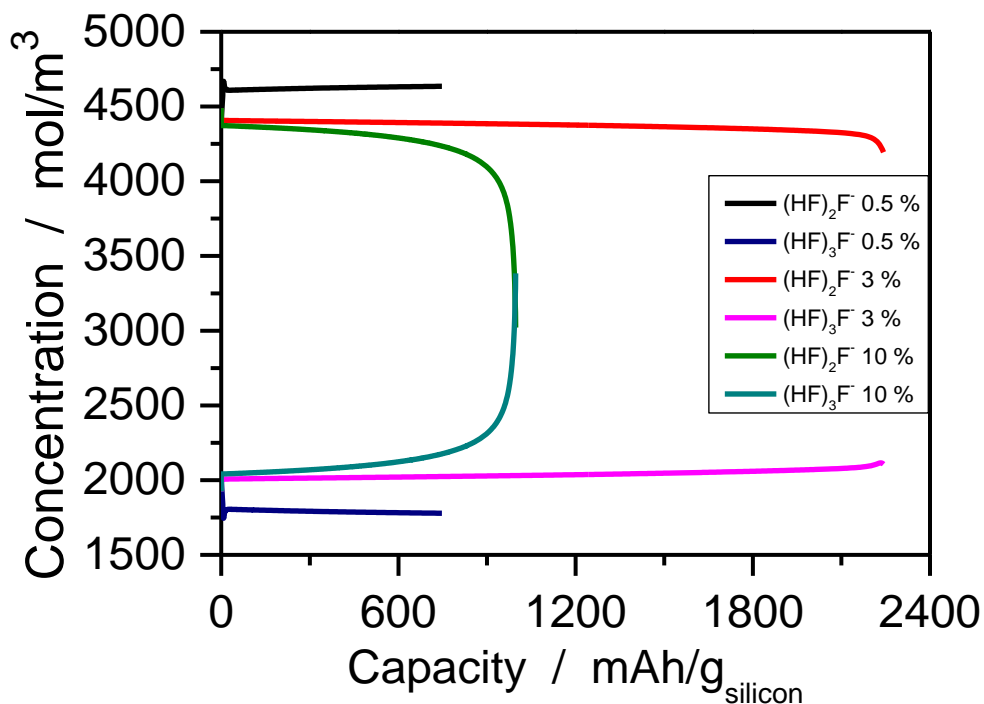


Figure 6-23 Average concentrations of the electrolyte species at the anode during discharge with various water contents

Figure 6-23 shows the average concentrations of the electrolyte species during discharge at the anode for various water contents. Below $1 \text{ mAh g}_{\text{silicon}}^{-1}$, the concentration of $(\text{HF})_2\text{F}^-$ decreases for all water contents. Only for very low water contents, e.g., 0.5 % H_2O , the concentration of $(\text{HF})_2\text{F}^-$ is increased subsequently and goes through a peak around $10 \text{ mAh g}_{\text{silicon}}^{-1}$. In total, in this early stage of discharge, the concentration of $(\text{HF})_2\text{F}^-$ increases for low water contents and it decreases for high water contents. The concentration of $(\text{HF})_3\text{F}^-$ shows opposed behavior. During discharge, we observe further, comparably small, concentration changes. With increasing the water content, the concentration of $(\text{HF})_2\text{F}^-$ remains constant, drops slowly, or drops fast during the discharge. In contrary to $(\text{HF})_2\text{F}^-$, the concentration of $(\text{HF})_3\text{F}^-$ remains constant, increases slowly, or increases fast during discharge.

Note that $(\text{HF})_2\text{F}^-$ is consumed while $(\text{HF})_3\text{F}^-$ is produced by the electrochemical anode reaction, and $(\text{HF})_2\text{F}^-$ is produced while $(\text{HF})_3\text{F}^-$ is consumed by the electrochemical cathode

reaction. We discussed in sections 6.1 and 6.2 that the concentration of $(\text{HF})_2\text{F}^-$ in the anode is decreasing before transport between the electrodes becomes relevant. It subsequently increases until nucleation and growth starts because there is a net production of $(\text{HF})_2\text{F}^-$ in the cell in the absence of crystallization. We found this full behavior at low water concentrations in sections 6.1 and 6.2. At larger water contents, however, we find some deviations from this full picture. In this case, the solubility of SiF_4 is lower and nucleation starts earlier. Therefore, the increase in $(\text{HF})_2\text{F}^-$ concentration is absent. In summary, at the early stage of discharge, the $(\text{HF})_2\text{F}^-$ concentration in the anode drops at high water contents, whereas it rises at low water contents.

After the nucleation phase, the cell reaction is balanced by the crystallization reaction and there is no net production of electrolyte species. Therefore, the concentrations remain relatively constant. At low water contents, transport of electrolyte into the anode is not limited. Therefore, the electrolyte concentration stays constant as the total cell reaction is balanced. The net reaction in the anode, i.e., the electrochemical anode reaction and the crystallization reaction together, consumes $(\text{HF})_2\text{F}^-$ and produces $(\text{HF})_3\text{F}^-$. At high water contents, crystallization occurs in the anode and limits the transport of electrolyte into the anode. As a result, the concentration of $(\text{HF})_2\text{F}^-$ in the anode decreases while the concentration of $(\text{HF})_3\text{F}^-$ increases during discharge.

Now, we discuss the discharge voltage plateaus since they are affected by the electrolyte concentrations. The voltage plateaus in Figure 6-19 are lowered by increasing the water content in the electrolyte. At 0.2 % H_2O , the cell exhibits a voltage plateau at 1.4 V. If the water content is increased to 1.0 % H_2O , the voltage plateau is decreased to 1.25 V. However, the voltage plateaus are longer at higher water contents as the discharge does not terminate at early stages. Clearly, the longest plateau is obtained by employing 1.0 % H_2O content in the electrolyte.

At high water contents (above 1.0 % H_2O), the voltage plateaus also decrease by adding more water into the electrolyte. As can be seen in Figure 6-21, the voltage plateaus are decreased from 1.25 V to 1.15 V. The battery exhibits the longest plateau at the maximum discharge

capacity ($2250 \text{ mAh g}_{\text{silicon}}^{-1}$ with 3 % H_2O). Further addition of water leads to shorter and less flat plateaus in the battery.

The reason why the voltage plateaus are lowered by further addition of water is related to nucleation and growth. As discussed in Figure 6-23, the beginning of the nucleation and growth determines the equilibrium concentrations of the electrolyte species. For instance, the equilibrium of the $(\text{HF})_2\text{F}^-$ is around 4600 mol m^{-3} at 0.5 % H_2O , 4450 mol m^{-3} at 3 % H_2O , and 4400 mol m^{-3} at 10 % H_2O . Parallel to these decreases on the $(\text{HF})_2\text{F}^-$ concentration, the anode overpotential increases as well. Therefore, the anode overpotential increases slowly starting from the low water contents to the high water contents. As a result, the increase on the anode overpotential decreases the discharge voltage plateaus.

However, the length of the discharge voltage plateaus is related to pore clogging in the electrodes. At low water contents, the diffusion of the oxygen determines the discharge capacity. This is because the crystallization in the cathode leads to pore clogging and eventually, the oxygen cannot diffuse fast enough resulting in the concentration gradients. Therefore, the plateau in the oxygen concentration is directly parallel to the voltage plateaus at low water contents. On the other hand, pore clogging in the anode determines the discharge capacity at high water contents. The crystallization in the anode leads to pore clogging and as a result, the electrolyte species cannot diffuse fast enough. Especially, the diffusion of $(\text{HF})_2\text{F}^-$ cannot sustain fast enough resulting in the consumption of this species in the anode. In this case, the voltage plateaus are parallel to $(\text{HF})_2\text{F}^-$ concentrations. Therefore the starvation of $(\text{HF})_2\text{F}^-$ in the anode results in discharge termination.

6.5 Discharge at Various Discharge Currents

As a last step, we show the effect of discharging the battery at various current densities in this section. Also, we compare our simulation results with the experimentally⁴⁸ observed ones.

In order to compare with the experiment, we discharge the battery with 0.3, 0.1, 0.05, and 0.01 mA cm^{-2} . These current densities are chosen because the same values were used in the

experiments. Figure 3-5 is shown again to present the experimental discharge results. However, the data points on this figure are extracted and plotted again to use the capacity with respect to the mass of silicon to be able to compare with the simulation results. The resulting plot is shown in Figure 6-25.

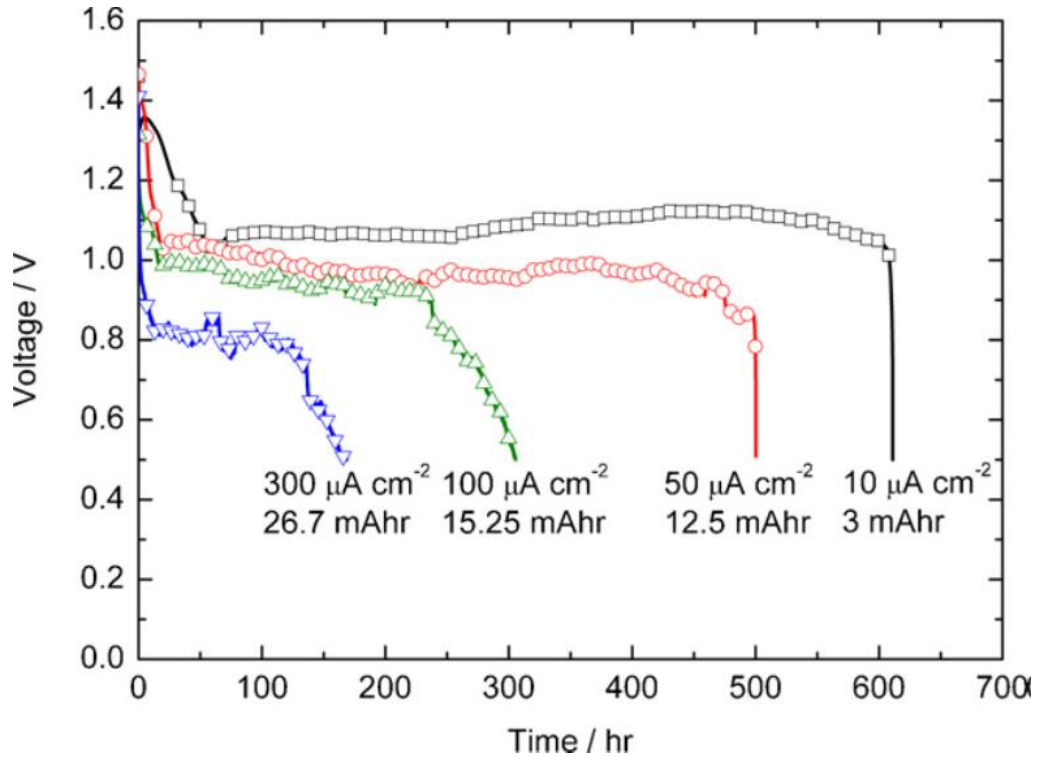


Figure 6-24 Discharge curves at various current densities (literature)⁴⁸

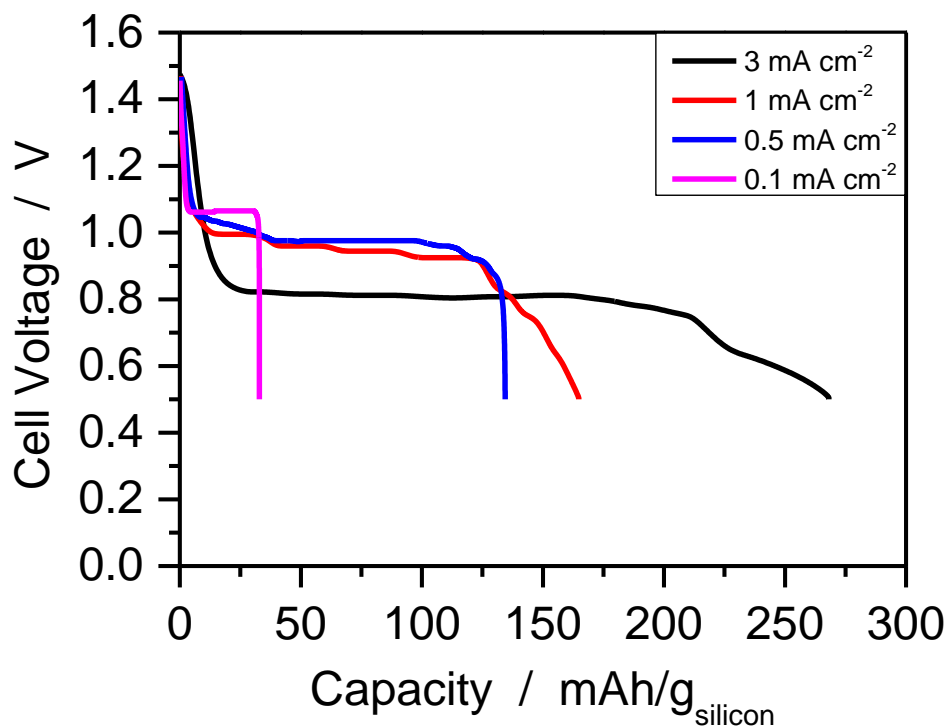


Figure 6-25 The data points from the discharge curves (Figure 6.24) are extracted and plotted again with respect to the mass of silicon at various current densities (literature)⁴⁸

The discharge curves of the Si-air battery that are obtained in the experiment are shown in Figure 6-25. The discharge processes were terminated at 0.5 V. Four different discharge currents are depicted in the figure. The capacities increase with increasing discharge current density. The discharge potentials decrease with increasing discharge current density. The highest discharge capacity is obtained at 0.3 mA cm^{-2} , while the highest discharge potential is obtained at 0.01 mA cm^{-2} .

The cell voltage decreases with increasing current density in Figure 6-25, due to polarization losses. The voltage plateaus are between 0.8 – 1.1 V depending on the current density. The capacity values obtained in the experiment are 275 , 170 , 140, and 35 $\text{mAh g}_{\text{silicon}}^{-1}$ for 0.3, 0.1, 0.05, and 0.01 mA cm^{-2} , respectively. The reason of obtaining higher discharge capacity with higher current density was explained by a model for SiO_2 deposition on porous carbon air electrode in Chapter 3. At low current densities, SiO_2 deposits have fine shape and they are

deposited at micro-pores. On the other hand, SiO_2 deposits have coarse and bulky shape at high current densities and they are deposited at meso- and macro-pore sites. Deposition at the meso- and macro-pore sites enables the further oxygen reduction and diffusion. Hence, higher capacities are obtained at higher discharge current densities. However, this explanation is contradictory to later finding. It was found that the battery is not cathode limited but rather it is anode limited. Therefore, the deposition of the crystal particles does not affect the discharge capacity significantly. The impedance of the anode determines the discharge capacity in Si-air batteries.

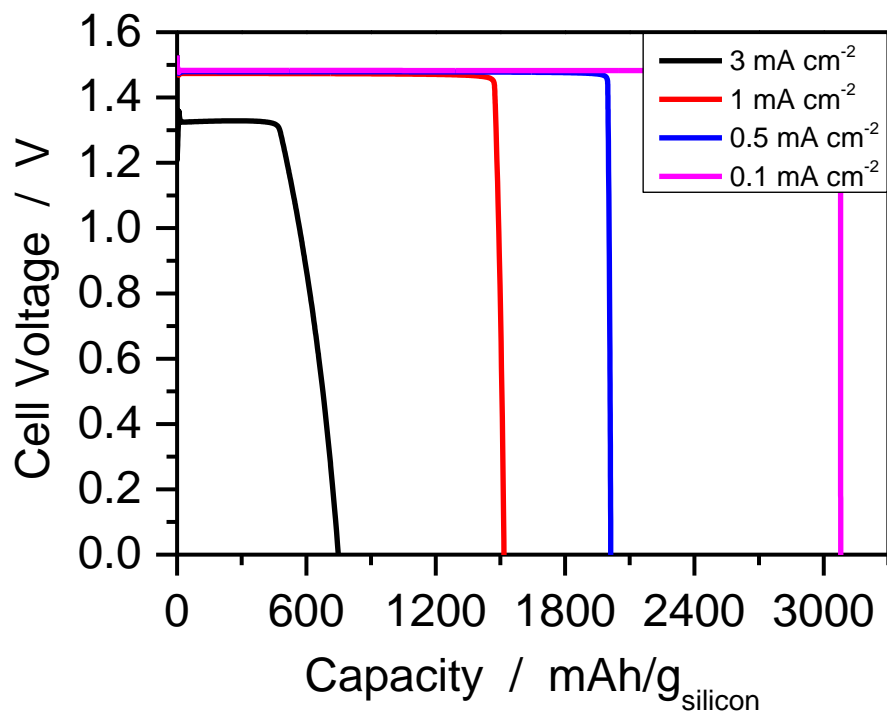


Figure 6-26 Discharge curves of our model at various current densities with 0.5 % H_2O

Figure 6-26 shows the simulation results of the Si-air battery model at low water content (0.5 % H_2O). Low water content is chosen since the water content in the RTIL electrolyte is not provided in the experiment.⁴⁸ We discharge the battery with 0.3, 0.1, 0.05, and 0.01 mA cm^{-2} and obtain 800, 1550, 2050, and 3100 $\text{mAh g}_{\text{silicon}}^{-1}$ discharge capacities, respectively.

The discharge capacity and the voltage plateau are both increased once the battery is being discharged at lower current densities. The increase of the voltage plateaus is expected as the polarization losses are decreased by drawing low current densities. However, the increase of the discharge capacity is related to crystallization. The crystallization is inhomogeneous at high discharge current densities resulting in larger crystal volume fractions near the oxygen inlet, and eventually, it leads to pore clogging. On the other hand, the crystallization at low current densities is more homogenous than at high current densities, and thus, the pores are still available for further oxygen reduction and diffusion. Therefore, in our simulations, the battery exhibits higher discharge capacities once it is discharged at low current densities.

In the experiment, the voltage plateaus were also increased at low current densities. The voltage plateaus are obtained between 0.8 – 1.1 V in the experiment, while we obtain the voltage plateaus between 1.3 – 1.5 V in our simulation. This is because we do not have the 0.4 V drop at the cathode attributed to the dissolved oxygen molecules (see Figure 6-6). Hence, our results partly agree with the experiment. Furthermore, the discharge capacities in our simulation are increased by drawing lower current densities; which is contradictory to experimental findings. The main reason of having higher discharge capacities in our simulation is because our model is cathode limited at low water contents. However, the battery is anode limited in the experiments. In order to capture this behavior, we will have to develop a more accurate model of silicon metal dissolution.

Chapter 7 : CONCLUSION AND OUTLOOK

The aim of this study is to understand the primary Si-air battery concept and model the battery mathematically in the computer environment. In order to understand the battery concept, the previous studies are reviewed first.^{9,16,48-52} Afterwards, the mathematical model of the reactions, transport mechanisms, oxygen dissolution, volume conditions, and nucleation and growth process are based on a Li-air battery model^{63,64} since the mechanisms of these two batteries show some similarities. Finally, the mathematical model is simulated and the results of the simulations are implemented and discussed.

The first experimental studies suggest that the battery is cathode limited due to pore clogging.⁴⁸ In contrast, later study shows that the battery is anode limited.⁵² The silicon metal in the experiments has a flat structure in the beginning of the discharge, and forms a porous structure during the anodic reaction. In this thesis, however, the anode electrode has initially a porous structure and the impedances of the electrodes are not modeled. Nevertheless, our model is designed to be anode limited at high water contents due to the high crystallization process at the anode. This prediction is reasonable when the experimental results of the remarkable impact of water on the discharge performance of a Si-air battery is taken into account.⁴⁹ To sum up, the developed Si-air battery model is based on the combination of the previous studies.

The simulation results of the Si-air battery match up with the assumptions explained above. The results show that the battery is cathode limited at very low water contents due to the high nucleation at the cathode electrode. However, the battery becomes anode limited once high water contents are employed in the electrolyte. Hence, good agreement is obtained between the simulation results of the battery model and the experimental results. Since the model developed in this thesis is the first mathematical model of primary Si-air batteries, there are differences in the simulation results due to the several assumptions and parameters which are assigned during the model development. Even though higher capacities as well as higher voltage plateaus are obtained with the simulation of the model comparing to literature, the simulation results still confirm the validity and the accuracy of the developed model. Nonetheless, due to

the limited time and lack of some parameters in the literature, some mechanisms could not be included or modeled properly in this Si-air battery model.

Additionally, the simulation results of the developed Si-air battery model express the discharge performance of the silicon-air battery under several conditions, such as addition of water into the electrolyte, discharging various constant current densities, the effect of changing the parameters etc. In this sense, the model and the results may help to investigate and understand the battery behavior without carrying out experiments. Once the battery is modeled with all mechanisms, the performance of the battery under several conditions can be predicted with more accuracy in a shorter time than performing experiments.

In order to improve the simulation and the experimental results, more studies should be done. For example, the morphology of the SiO_2 crystal should be investigated first. This is because the standard Gibbs free energy of alpha-quartz SiO_2 results in a higher open circuit voltage (around 2.2 V) than 1.49 V. This argument shows that the crystal produced by the crystallization process is different than the pure crystal. Furthermore, the deposition mechanisms in the electrode pores and in the separator together with the anode surface morphologies during cycling can be investigated as well. Also, all the species in the electrolyte and phases of these species need to be examined in order to fully understand the discharge process. After that, these experimental inputs can be inserted into the mathematical model. The accuracy of the parameters that are taken from the literature is crucial for the simulation performance. Besides these experimental inputs, the dissolution of the anode electrode can be modeled again in a way that it has a flat structure and becomes porous by the anodic reaction. Last but not least, depending on the future experimental investigations and results, new mechanisms can be inserted into this developed model. In that respect, this model can be considered as the base for the further models in the future.

ACKNOWLEDGEMENT

First and foremost, I would like to thank Prof. Dr. Arnulf Latz for providing me with the opportunity to work on this Master's Thesis in a very sophisticated environment such as Deutsches Zentrum für Luft- und Raumfahrt and guiding me through all the research activities.

I am also grateful for having the input and supportive comments of my second advisor Prof. Dr. Werner Tillmetz. His scientific knowledge has always guided me throughout.

I owe my deepest gratitude to Dr. Birger Horstmann for the continuous support of my Master's Thesis, for his patience, motivation, enthusiasm, and immense knowledge. This thesis would not have been possible without his mentoring and helpful advice.

Furthermore, I want to thank my all colleagues in the Theorie group at DLR. They never hesitated to share their valuable ideas with me. Special thanks are given to David Fronczek for always being helpful and never hesitating to answer my questions.

Last but not least, I owe more than thanks to my friends and my family members including my parents and my uncle, for their support and encouragement throughout my life. Without their support, it would be impossible for me to finish my education.

LIST OF FIGURES

Figure 2-1 Advances in development of primary batteries in 20 th century. Continuous discharge at 20°C; 40-60 h rate; AA or similar size battery ¹	4
Figure 2-2 Development of some battery chemistries ³	6
Figure 2-3 The gravimetric energy densities for various types of rechargeable batteries and the gasoline. Theoretical energy densities are based on thermodynamics. ⁶	8
Figure 2-4 Schematic representation of a zinc-air battery.....	12
Figure 2-5 The polarization curves of the anodic and cathodic reactions ¹⁹	13
Figure 2-6 Schematic representation of a Li-air battery ⁶	17
Figure 2-7 A single measured discharge-charge cycle for an aprotic Li-air cell (based on SP carbon) operated at $\sim 0.1 \text{ mA cm}^{-2}$ current density ⁶	18
Figure 2-8 Major challenges for rechargeable Li-air batteries ²⁹	19
Figure 3-1 Discharges profiles of silicon-air battery with an alkaline solution: a) Galvanostatic discharge curve of a modified silicon-air battery with a discharge current density of 0.05 mA cm^{-2} . b) Galvanostatic discharge curve of an unmodified silicon-air battery with a discharge current density of 0.05 mA cm^{-2} . ⁵⁰	24
Figure 3-2 Discharge profiles of a silicon-air battery with a GPE as electrolyte ⁵¹	26
Figure 3-3 A schematic diagram of the silicon-air battery ⁴⁸	27
Figure 3-4 Polarization voltammograms recorded at 5 mV s^{-1} for various electrodes ⁴⁸	28
Figure 3-5 Discharge profiles of silicon-air cells at different constant current densities ⁴⁸	30
Figure 3-6 A model for SiO ₂ deposition on porous carbon electrode. a) Low discharge currents and b) high discharge currents ⁴⁸	30

Figure 3-7 Variation of the discharge profiles with increasing water content in the electrolyte:⁴⁹
EMI · HF2.3F (■), EMI · HF2.3F + 10 vol % H2O (●), and HF2.3F + 15 vol % H2O (▲) at
discharge rate 0.3 mA cm⁻² 32

Figure 3-8 Electrolyte conductivity and discharge capacity as a function of water content⁴⁹ 32

Figure 3-9 Nyquist plots for silicon anode and air cathode half-cells⁵² 34

Figure 3-10 Overpotentials on Si-air cell, silicon anode and air cathode at a discharge current of
0.3 mA cm⁻².⁵² 35

Figure 3-11 Discharge profiles of silicon-air battery at 0.3 mA cm⁻², while exchanging the silicon
anode⁵² 37

Figure 3-12 Discharge profiles of silicon-air battery at 0.3 mA cm⁻², while exchanging the air cathode⁵²
..... 37

Figure 4-1 Representative modeling domains for the battery 39

Figure 4-2 A schematic of the silicon-air battery 40

Figure 4-3 Formation energy of a crystal nucleus⁶³ 51

Figure 5-1 Polarization voltammograms and the Butler Volmer equation fitting. Dots are the
experimental results, lines are the calculation results 57

Figure 6-1 Crystallization criterion (dash) and driving force (line) at various low water contents. The effect
of water addition on the driving force, crystallization, and nucleation are implemented. 62

Figure 6-2 Crystallization criterion (dash) and driving force (line) at various high water contents. The
effect of water addition on the driving force, crystallization, and nucleation are implemented. 62

Figure 6-3 SiF4 concentrations at anode versus capacity for various water contents. The influence of
water addition on the concentration is shown at 0.3 mA cm⁻² 64

Figure 6-4 SiF4 concentrations at cathode versus capacity for various water contents. The influence of
water addition on the concentration is shown at 0.3 mA cm⁻² 64

Figure 6-5 Experimental overpotential⁵² of the Si-air cell, anode and cathode at 0.3 mA cm⁻² 65

Figure 6-6 Simulated overpotentials of anode and cathode with 0.1 % H₂O at 0.3 mA cm⁻² 66

Figure 6-7 O₂ concentration at cathode with 0.1 % H₂O at 0.3 mA cm⁻² 67

Figure 6-8 HF₂F⁻ – concentrations at anode and cathode during the discharge with 0.1 % H₂O at 0.3 mA cm⁻² 69

Figure 6-9 HF₃F⁻ – concentrations at anode and cathode during the discharge with 0.1 % H₂O at 0.3 mA cm⁻² 69

Figure 6-10 Overpotentials of anode and cathode during the discharge with 1 % H₂O and 10 % H₂O at 0.3 mA cm⁻² 70

Figure 6-11 Discharge curves (with 4 time points marked) with various water contents at 0.3 mA cm⁻². 72

Figure 6-12 Volume fractions in cathode and anode with 0.5 % H₂O at the end of discharge..... 73

Figure 6-13 Electrolyte volume fractions during the discharge of the battery with 0.5 % H₂O..... 74

Figure 6-14 Volume fractions in cathode and anode with 3 % H₂O at the end of discharge..... 75

Figure 6-15 Electrolyte volume fractions during the discharge of the battery with 3 % H₂O..... 76

Figure 6-16 Volume fractions in cathode and anode with 10 % H₂O at the end of discharge..... 77

Figure 6-17 Electrolyte volume fractions during the discharge of the battery with 10 % H₂O..... 78

Figure 6-18 Average SiO₂ volume fractions at anode and cathode with various water contents 79

Figure 6-19 Discharge capacity of the Si-air battery at low water contents with 0.3 mA cm⁻² 80

Figure 6-20 The effect of low water contents on the discharge capacity. Data points are taken at the end of discharge. 81

Figure 6-21 Discharge capacity of the Si-air battery at high water contents with 0.3 mA cm⁻² 82

Figure 6-22 The effect of high water contents on the discharge capacity..... 83

Figure 6-23 Average concentrations of the electrolyte species at the anode during discharge with various water contents..... 84

Figure 6-24 Discharge curves at various current densities (literature)⁴⁸ 87

Figure 6-25 The data points from the discharge curves (Figure 6.24) are extracted and plotted again with respect to the mass of silicon at various current densities (literature)⁴⁸ 88

Figure 6-26 Discharge curves of our model at various current densities with 0.5 % H2O 89

LIST OF TABLES

Table 2-1 Major advantages and disadvantages of metal-air batteries ¹	7
Table 2-2 A comparison of metal air batteries. ^{6,8,9} Only the masses of the active reactant materials are included. The specific energy values are given for the cases of inclusion and exclusion of O ₂	9
Table 3-1 Silicon electrodes corrosion rates in EMI · HF2.3F ⁴⁸	29
Table 5-1 Definition of parameters for the silicon-air battery	58

LIST OF SYMBOLS

Symbol	Unit	Meaning
α_i	—	Transfer coefficient
β	—	Bruggeman coefficient
δ, δ_0	m	Diffusion layer thickness around SiO ₂ nucleus
ε_j	m ³ m ⁻³	Volume fraction of a phase
γ	J m ⁻²	Surface energy
κ	S cm ⁻¹	Conductivity of room temperature ionic liquid
$\Delta\mu_i$	J mol ⁻¹	Chemical potential of species
ϕ_j	V	Electric potential of phase
$\Delta\phi_j$	V	Electric potential step for reaction
A	m ²	Electrode surface area
α	m	Length scale of SiO ₂ , $\alpha = (V_{\text{cryst}}^{\text{M}})^{1/3} N_{\text{A}}^{-1}$
$A_{\text{k}}^{\text{spez}}$	m ² m ⁻³	Specific surface of reaction
c_{k}	mol m ⁻³	Concentration of species
c_{k}^{S}	mol m ⁻³	Solubility of species
D_0	m ² s ⁻¹	Self-diffusion coefficient
D_{k}	m ² s ⁻¹	Diffusion coefficient of species
D_{k}^{M}	mol m ⁻¹ s ⁻¹	Migration coefficient of species
E	V	Potential
ΔG	J mol ⁻¹	Molar Gibbs reaction enthalpy
h	m	Height of battery cell
H	mol m ⁻³ Pa	Henry's constant
$i, i_{\text{f}}, i_{\text{b}}$	A	Current, forward and backward currents
j	A m ⁻²	Current density
$\vec{J}_{\text{k}}^{\text{D}}, \vec{J}_{\text{k}}^{\text{M}}$	mol m ⁻² s ⁻¹	Diffusion and migration flux
$k_{\text{f}}^{\text{i}}, k_{\text{b}}^{\text{i}}$	—	Forward and backward kinetic coefficient of reaction
n, n_{crit}	—	Number of particles in SiO ₂ nucleus
N_0	m ⁻³	Number of nucleation sites
\dot{N}	s ⁻¹ m ⁻³	Nucleation rate of SiO ₂
η	V	Overpotential
p_{k}	Pa	Partial pressure of species
r_i	mol m ⁻² s ⁻¹	Rate of reaction
r	m	Radius of SiO ₂ nucleus
V_i	m ³	Volume of phase
\bar{V}_i	m ³ mol ⁻¹	Partial molar volume of species
\vec{v}_i	m s ⁻¹	Convection velocity phase
Z	—	Zeldovich factor
z_i	—	Charge number of species

LIST OF CONSTANTS

Symbol	Value
F	96,485.256 A s mol ⁻¹
k	1.380662×10^{-23} J K ⁻¹
p_0	101,325 Pa
R	8.3145353 J k ⁻¹ mol ⁻¹
T_0	298.15 K

BIBLIOGRAPHY

1. Reddy, T. B. & Linden, D. *Linden's Handbook of Batteries*. (McGraw-Hill, 2011).
2. Bessler, W. G., Gewies, S. & Vogler, M. A new framework for physically based modeling of solid oxide fuel cells. *Electrochim. Acta* **53**, 1782–1800 (2007).
3. Armand, M. & Tarascon, J.-M. Building better batteries. *Nature* **451**, 652–7 (2008).
4. BMW i3. at <<http://www.bmw.com/com/en/newvehicles/i/i3/2013/showroom/drive.html>>
5. Volkswagen E-Up. at <http://www.vwvortex.com/artman/publish/article_2661.shtml>
6. Girishkumar, G., McCloskey, B., Luntz, a. C., Swanson, S. & Wilcke, W. Lithium–Air Battery: Promise and Challenges. *J. Phys. Chem. Lett.* **1**, 2193–2203 (2010).
7. Abraham, K. M. & Jiang, Z. A Polymer Electrolyte-Based Rechargeable Lithium/Oxygen Battery. *Electrochemical Sci. Technol.* **143**, 1–5 (1996).
8. Scrosati, B., Abraham, K. M., van Schalkwijk, W. & Hassoun, J. *Lithium Batteries*. 392 (John Wiley & Sons Inc, 2013).
9. Jakes, P. *et al.* Limitation of discharge capacity and mechanisms of air-electrode deactivation in silicon-air batteries. *ChemSusChem* **5**, 2278–85 (2012).
10. Cheng, F. & Chen, J. Metal-air batteries: from oxygen reduction electrochemistry to cathode catalysts. *Chem. Soc. Rev.* **41**, 2172–92 (2012).
11. Freunberger, S. a *et al.* Reactions in the rechargeable lithium-O₂ battery with alkyl carbonate electrolytes. *J. Am. Chem. Soc.* **133**, 8040–7 (2011).
12. Mizuno, F., Nakanishi, S., Kotani, Y., Yokoishi, S. & Iba, H. Rechargeable Li-Air Batteries with Carbonate-Based Liquid Electrolytes. *J. Electrochem. Soc. Jpn.* **78**, 403–405 (2010).
13. Mccloskey, B. D., Bethune, D. S., Shelby, R. M., Girishkumar, G. & Luntz, A. C. Solvents ' Critical Role in Nonaqueous Lithium/Oxygen Battery. *J. Phys. Chem. Lett.* **2**, 1161–1166 (2011).
14. Albertus, P. *et al.* Identifying Capacity Limitations in the Li/Oxygen Battery Using Experiments and Modeling. *J. Electrochem. Soc.* **158**, A343 (2011).
15. Viswanathan, V. *et al.* Electrical conductivity in Li₂O₂ and its role in determining capacity limitations in non-aqueous Li-O₂ batteries. *J. Chem. Phys.* **135**, 214704 (2011).
16. Cohn, G., Starosvetsky, D., Hagiwara, R., Macdonald, D. D. & Ein-Eli, Y. Silicon–air batteries. *Electrochem. commun.* **11**, 1916–1918 (2009).

17. Ein-Eli, Y. Silicon-air. at <http://gtep.technion.ac.il/energy_storage_and_conversion.php>
18. Mclarnon, F. R., Cairns, E. J. & Division, A. S. The Secondary Alkaline Zinc Electrode. **138**, 645–664 (1991).
19. Lee, J.-S. *et al.* Metal-Air Batteries with High Energy Density: Li-Air versus Zn-Air. *Adv. Energy Mater.* **1**, 34–50 (2011).
20. Harting, K., Kunz, U. & Turek, T. Zinc-air Batteries: Prospects and Challenges for Future Improvement. *Zeitschrift für Phys. Chemie* **226**, 151–166 (2012).
21. Mao, Z. & White, R. E. Mathematical Modeling of a Primary Zinc/Air Battery. **139**, (1992).
22. Chakkaravarthy, C., Waheed, A. K. A. & Udupa, H. V. K. Zinc—air alkaline batteries — A review. *J. Power Sources* **6**, 203–228 (1981).
23. Richter, B. *et al.* Energy Future: Think Efficiency. *Am. Phys. Soc.* (2008).
24. Shao, Y. *et al.* Making Li-Air Batteries Rechargeable: Material Challenges. *Adv. Funct. Mater.* **23**, 987–1004 (2013).
25. Zhang, S. S., Foster, D. & Read, J. Discharge characteristic of a non-aqueous electrolyte Li/O₂ battery. *J. Power Sources* **195**, 1235–1240 (2010).
26. Laoire, C. O., Mukerjee, S., Abraham, K. M., Plichta, E. J. & Hendrickson, M. a. Elucidating the Mechanism of Oxygen Reduction for Lithium-Air Battery Applications. *J. Phys. Chem. C* **113**, 20127–20134 (2009).
27. Ogasawara, T., Débart, A., Holzapfel, M., Novák, P. & Bruce, P. G. Rechargeable Li₂O₂ electrode for lithium batteries. *J. Am. Chem. Soc.* **128**, 1390–3 (2006).
28. Débart, A., Paterson, A. J., Bao, J. & Bruce, P. G. Alpha-MnO₂ nanowires: a catalyst for the O₂ electrode in rechargeable lithium batteries. *Angew. Chem. Int. Ed. Engl.* **47**, 4521–4 (2008).
29. Lu, Y.-C. *et al.* Lithium–oxygen batteries: bridging mechanistic understanding and battery performance. *Energy Environ. Sci.* **6**, 750 (2013).
30. Winter, B. M., Besenhard, J. O., Spahr, M. E. & Novák, P. Insertion Electrode Materials for Rechargeable Lithium Batteries **. 725–763 (1998).
31. Brandt, K. Historical development of secondary lithium batteries. **69**, 173–183 (1994).
32. Aurbach, D., Zinigrad, E., Cohen, Y. & Teller, H. A short review of failure mechanisms of lithium metal and lithiated graphite anodes in liquid electrolyte solutions. **148**, 405–416 (2002).
33. Kumar, B. *et al.* A Solid-State, Rechargeable, Long Cycle Life Lithium–Air Battery. *J. Electrochem. Soc.* **157**, A50 (2010).

34. Weesman, I. Correlation Between Surface Chemistry, Morphology, Cycling Efficiency and Interfacial Properties of Li Electrodes in Solutions Containing Different Li Salts. **39**, 51–71 (1994).
35. Freunberger, S. a *et al.* The lithium-oxygen battery with ether-based electrolytes. *Angew. Chem. Int. Ed. Engl.* **50**, 8609–13 (2011).
36. Bruce, P. G., Freunberger, S. A., Hardwick, L. J. & Tarascon, J.-M. Li–O₂ and Li–S batteries with high energy storage. **11**, 19–30 (2012).
37. Mizuno, F. *et al.* Design of Non-aqueous Electrolytes for Rechargeable Li–O₂ Batteries. *Electrochemistry* **79**, 876–881 (2011).
38. Wang, Y., Zheng, D., Yang, X.-Q. & Qu, D. High rate oxygen reduction in non-aqueous electrolytes with the addition of perfluorinated additives. *Energy Environ. Sci.* **4**, 3697 (2011).
39. Beattie, S. D., Manolescu, D. M. & Blair, S. L. High-Capacity Lithium–Air Cathodes. *J. Electrochem. Soc.* **156**, A44 (2009).
40. Kraytsberg, A. & Ein-Eli, Y. Review on Li–air batteries—Opportunities, limitations and perspective. *J. Power Sources* **196**, 886–893 (2011).
41. Xiao, J. *et al.* Hierarchically porous graphene as a lithium-air battery electrode. *Nano Lett.* **11**, 5071–8 (2011).
42. Gallant, B. M. *et al.* Chemical and Morphological Changes of Li–O₂ Battery Electrodes upon Cycling. **116**, 20800–20805 (2012).
43. Mitchell, R. R., Gallant, B. M., Shao-horn, Y. & Thompson, C. V. Mechanisms of Morphological Evolution of Li₂O₂ Particles during Electrochemical Growth. 1–5 (2013).
44. Mitchell, R. R., Gallant, B. M., Thompson, C. V. & Shao-Horn, Y. All-carbon-nanofiber electrodes for high-energy rechargeable Li–O₂ batteries. *Energy Environ. Sci.* **4**, 2952 (2011).
45. Gallant, B. M. *et al.* Influence of Li₂O₂ morphology on oxygen reduction and evolution kinetics in Li–O₂ batteries. *Energy Environ. Sci.* **6**, 2518 (2013).
46. Adams, B. D. *et al.* Current density dependence of peroxide formation in the Li–O₂ battery and its effect on charge. *Energy Environ. Sci.* **6**, 1772 (2013).
47. Horstmann, B. *et al.* Rate-dependent morphology of Li₂O₂ growth in Li–O₂ Batteries. *J. Phys. Chem. Lett.* **4**, 4217–4222 (2013).
48. Cohn, G. & Ein-Eli, Y. Study and development of non-aqueous silicon-air battery. *J. Power Sources* **195**, 4963–4970 (2010).
49. Cohn, G., Macdonald, D. D. & Ein-Eli, Y. Remarkable impact of water on the discharge performance of a silicon-air battery. *ChemSusChem* **4**, 1124–9 (2011).

50. Zhong, X. *et al.* High-capacity silicon-air battery in alkaline solution. *ChemSusChem* **5**, 177–80 (2012).
51. Cohn, G., Altberg, A., Macdonald, D. D. & Ein-Eli, Y. A silicon–air battery utilizing a composite polymer electrolyte. *Electrochim. Acta* **58**, 161–164 (2011).
52. Cohn, G., Eichel, R. a & Ein-Eli, Y. New insight into the discharge mechanism of silicon-air batteries using electrochemical impedance spectroscopy. *Phys. Chem. Chem. Phys.* **15**, 3256–63 (2013).
53. Tsuda, T. *et al.* A highly conductive composite electrolyte consisting of polymer and room temperature molten fluorohydrogenates. **149**, 295–298 (2002).
54. Hagiwara, R., Hirashige, T., Tsuda, T. & Ito, Y. A Highly Conductive Room Temperature Molten Fluoride: EMIF·2.3HF. *J. Electrochem. Soc.* **149**, D1 (2002).
55. Raz, O., Shmueli, Z., Hagiwara, R. & Ein-Eli, Y. Porous Silicon Formation in Fluorohydrogenate Ionic Liquids. *J. Electrochem. Soc.* **157**, H281 (2010).
56. Viswanathan, V., Speidel, A., Gowda, S. & Luntz, A. C. Li– O₂ Kinetic Overpotentials: Tafel Plots from Experiment and First- Principles Theory. (2013).
57. Mo, Y., Ong, S. P. & Ceder, G. First-principles study of the oxygen evolution reaction of lithium peroxide in the lithium-air battery. *Phys. Rev. B* **84**, 205446 (2011).
58. Hummelshøj, J. S., Luntz, a C. & Nørskov, J. K. Theoretical evidence for low kinetic overpotentials in Li-O₂ electrochemistry. *J. Chem. Phys.* **138**, 034703 (2013).
59. Radin, M. D., Rodriguez, J. F., Tian, F. & Siegel, D. J. Lithium peroxide surfaces are metallic, while lithium oxide surfaces are not. *J. Am. Chem. Soc.* **134**, 1093–103 (2012).
60. Radin, M. D., Tian, F. & Siegel, D. J. Electronic structure of Li₂O₂ {0001} surfaces. *J. Mater. Sci.* **47**, 7564–7570 (2012).
61. Hummelshøj, J. S. *et al.* Communications: Elementary oxygen electrode reactions in the aprotic Li-air battery. *J. Chem. Phys.* **132**, 071101 (2010).
62. Eberle, D. & Horstmann, B. Oxygen reduction on transition metal catalysts in aqueous electrolyte : Elementary kinetic modeling. *Phys. Chem. Chem. Phys. Full Artic.* 1–12 doi:10.1039/b000000x
63. Horstmann, B., Danner, T. & Bessler, W. G. Precipitation in aqueous lithium–oxygen batteries: a model-based analysis. *Energy Environ. Sci.* **6**, 1299–1314 (2013).
64. Neidhardt, J. P. *et al.* A Flexible Framework for Modeling Multiple Solid, Liquid and Gaseous Phases in Batteries and Fuel Cells. *J. Electrochem. Soc.* **159**, A1528–A1542 (2012).
65. Latz, A. & Zausch, J. Thermodynamic consistent transport theory of Li-ion batteries. *J. Power Sources* **196**, 3296–3302 (2011).

66. Andrei, P., Zheng, J. P., Hendrickson, M. & Plichta, E. J. Some Possible Approaches for Improving the Energy Density of Li-Air Batteries. *J. Electrochem. Soc.* **157**, A1287 (2010).
67. Goodwin, D. G. Cantera. at <<http://code.google.com/p/cantera/>>
68. Deuffhard, P., Hairer, E. & Zugck, J. One-step and Extrapolation Methods for Differential-Algebraic Systems. **516**, 501–516 (1987).
69. Bard, A. J. & Faulkner, L. R. *Electrochemical Methods: Fundamentals and Applications*. (2001).
70. Bazant, M. Z. Theory of Chemical Kinetics and Charge Transfer based on Nonequilibrium Thermodynamics. *Acc. Chem. Res.* **46**, (2013).
71. Kashchiev, D. & van Rosmalen, G. M. Review: Nucleation in solutions revisited. *Cryst. Res. Technol.* **38**, 555–574 (2003).
72. Erdemir, D., Lee, A. Y. & Myerson, A. S. Nucleation of crystals from solution: classical and two-step models. *Acc. Chem. Res.* **42**, 621–9 (2009).
73. Yoreo, J. J. De & Vekilov, P. G. Principles of Crystal Nucleation and Growth. (2003).
74. Atkins, P. & de Paula, J. *Atkin's Physical Chemistry*. (Oxford University Press, 2006).
75. Lyman, J. L. Thermochemical Properties of Si₂F₆ and SiF₄ in Gas and Condensed Phases. *J. Phys. Chem. Ref. Data* **30**, 165–186 (2001).
76. Tromans, D. Temperature and pressure dependent solubility of oxygen in water: a thermodynamic analysis. *Hydrometallurgy* **48**, 327 (1998).
77. Ohtsuki, J., Matsumoto, K. & Hagiwara, R. Physical and Electrochemical Properties of 1-ethyl-3-methylimidazolium Ionic Liquids of Mixed Anions, (FH)_nF⁻, BF₄⁻, and N(SO₂CF₃)₂. *Electrochem. commun.* **77**, 624–626 (2009).
78. Goumans, T. P. M., Wander, A., Brown, W. a & Catlow, C. R. a. Structure and stability of the (001) alpha-quartz surface. *Phys. Chem. Chem. Phys.* **9**, 2146–52 (2007).
79. Murashov, V. V. Reconstruction of pristine and hydrolyzed quartz surfaces. *J. Phys. Chem. B* **109**, 4144–51 (2005).
80. Murashov, V. V & Demchuk, E. A comparative study of unrelaxed surfaces on quartz and kaolinite, using the periodic density functional theory. *J. Phys. Chem. B* **109**, 10835–41 (2005).
81. Vita, A. De, Car, R., Rignanese, G. M., Charlier, J. C. & Gonze, X. First-Principles Molecular-Dynamics Study of the (0001) Alpha-Quartz Surface. *Am. Phys. Soc.* **61**, 250–255 (2000).
82. Han, P. & Bartels, D. M. Temperature Dependence of Oxygen Diffusion in H₂O and D₂O †. *J. Phys. Chem.* **100**, 5597–5602 (1996).

83. Eichel, R.-A. *et al.* Private Conversation. (2013).